University of Iceland
Faculty of Science
Department of Physics

RH-08-2008

Geometrical Effects in Transport through Quantum Wires with Side-coupled Quantum Dots

by

Ómar Valsson

A thesis submitted in partial satisfaction of the
requirements for the degree of
Master of Science in Physics at the University of Iceland

Committee in charge:
Prof. Viðar Guðmundsson, Chair
Dr. Sigurður I. Erlingsson

Reykjavík
June 2008

Geometrical Effects in Transport through Quantum Wires with Side-coupled Quantum Dots

High resolution version available at:
http://www.raunvis.hi.is/reports/2008/RH-08-2008.html

Abstract

The coherent electronic transport in quantum wires with embedded nanostructures is investigated within a theoretical framework consisting of the Landauer-Büttiker formalism and a quasi-1D Lippmann-Schwinger scattering formalism. The conductance of a clean ballistic quantum wire exhibits step like quantization. However, the embedded nanostructures are expected to introduced deviations to the quantization. The focus of this work is on quantum wire with side-coupled quantum dots. These quantum wire systems show in general a rich conductance structure caused mainly by quasi-bound states in the quantum dots. A quantum wire with two side-coupled quantum dots shows indication of a peculiar state, so called bound state in the continuum. A simple model of a closed quantum dot with a similar geometry as the side-coupled quantum dots is introduced. This model is used to characterize the quasi-bound states in the open side-coupled quantum dots.

Acknowledgments

The work presented in this M.Sc. thesis was carried out at the Science Institute, University of Iceland under the supervision of Prof. Viðar Guðmundsson. His knowledge of, insight, and interest in physics has been essential for this work and for that I acknowledge. Furthermore, I would like to thank Dr. Sigurður Ingi Erlingsson and Prof. Jón Tómas Guðmundsson for carefully reading the manuscript of this thesis.

I would like to acknowledge my family and friends for their support throughout the years.

This research was partly funded by the Icelandic Research Fund for Graduate Students, the Icelandic Research Fund, and the Icelandic Instrument Fund.

Contents

Chapter 1

Introduction

Low-dimensional nanostructures, where the full quantum mechanical wave nature of electrons has to be taken in account, are not only interesting from the viewpoint of fundamental physics but will be an important part of future electronic devices [1]. These nanostructures are characterized by that the sample dimensions are on the nanoscale and thus on the order of or smaller than the relevant length scales. These length scales are, for example, the mean free path, phase coherence length of the electrons, the Fermi wavelength, and the Bohr radius. This requirement is easily fulfilled in today's low temperature experiments.

Low-dimensional means that the electrons are confined in one or more direction so they are restricted to discrete energies or subbands in the confining directions but free to move in the other directions. The electrons can be confined in one or two directions resulting in a two-dimensional electron gas or a quantum wire, respectively. The electrons can also be confined in all three directions resulting in a quantum dot with discrete energy levels. Such structures are sometimes called artificial atoms since the electronic structure resemblances natural atoms [2].

A two-dimensional electron gas can be formed at an interface of AlGaAs and GaAs in a semiconductor heterostructure. Using modulation doping, where doping is introduced on the AlGaAs side, a potential well or a confinement potential is formed on the GaAs side. At low enough temperature and electron density all of the electrons are in the lowest subband so the electrons effectively behave as two-dimensional particles and the confining direction can be ignored. A quantum wire can be fabricated from a two-dimensional electron gas by further confining the electrons. This can be done by the use of deep or shallow etching or by placing a negative bias on a split gate [1].

These system show many interesting physical effects due to their full quantum mechanical nature and low-dimensionality. One of these effect is that the conductance of clean ballistic quantum wires exhibit step like quantization which is very far from the normal ohmic behavior. This came as a surprise when first observed in ballistic quantum point contacts in a two-dimensional electron gas [3, 4].

The subject of this thesis will be coherent electronic transport through quantum wire systems, i.e. quantum wires with embedded nanostructures. The embedded nanostructures should modify the conductance of the quantum wire system from the step like quantization. The embedded nanostructures can, for example, be simple impurities, quantum dots, or quantum rings. However, the focus here will be on side-coupled quantum dots. These side-coupled quantum dots are open quantum dots that are embedded to the sides of the wire far from the center and thus side-coupled to the quantum wire.

The transport will be investigated in a static single-particle picture by using a theoretical framework consisting of the Landauer-Büttiker formalism and a quasi-1D Lippmann-Schwinger scattering formalism. The Landauer-Büttiker formalism connects the transmission or scattering of electrons in a quantum wire with the conductance of the quantum wire. The transmission will be obtained using a quasi-1D Lippmann-Schwinger scattering formalism. One of the strong points of the quasi-1D Lippmann-Schwinger scattering formalism is that it takes into account all the finer details of the geometry of the quantum wire systems. Thus, allowing investigation of interesting geometrical effects in the quantum wire systems. It also allows the visualization of the scattering processes which helps greatly in understanding the electronic transport through the quantum wire systems.

The organization of this thesis is the following. The theoretical framework is introduced in chapters 2 and 3. A simple model of an isolated closed quantum dot with a similar geometry as the open side-coupled quantum dots is introduced in chapter 4. The results of the transport calculations for the quantum wire systems are considered in chapter 5. Finally, the thesis is summarized in chapter 6. Derivations and numerical methods are shown in full detail in the appendices.

Chapter 2

Electronic Transport in Quantum Wires

Here, the first part of the theoretical framework is introduced. First, the Landauer-Büttiker formalism is presented. Subsequently, the general properties of quantum wire systems are examined. Finally, the confinement potential is introduced.

2.1 Landauer-Büttiker Formalism

The Landauer-Büttiker formalism connects the probability that electrons that impinge on one end of a wire are transmitted through the wire and reach the other end with the conductance of a coherent quantum wire [1, 5–7]. The Landauer-Büttiker formalism is in the single-particle picture which can be justified by the Fermi liquid theory of interacting electrons [6].

The setup of the quantum wire system is the following. There are two reservoirs which provide electrons that are fed into leads which take the electrons to a localized scattering area where the embedded nanostructure is situated. There is a confinement potential in the quantum wire that confines the electrons in the transverse direction, which here is taken as the y-direction. Due to the confinement the electrons are restricted to certain subbands in the transverse direction but free to move along the quantum wire in the x-direction. This results in a multiband quasi-one-dimensional scattering problem. The name quantum waveguides is sometimes used for such systems since these systems are in many aspects analogous to conventional waveguides covered in all introductory textbooks on electromagnetism [8].

The wavefunctions of the subbands fulfill

$$\left[-\frac{\hbar}{2m}\frac{d^2}{dy^2} + V_\mathrm{c}(y)\right]\chi_m(y) = \varepsilon_m \chi_m(y), \tag{2.1}$$

where $V_\mathrm{c}(y)$ is the confinement potential, ε_m is the energy of subband m, and the wavefunctions $\chi_m(y)$ are orthonormal. The confinement potential is kept unspecified

for now since the formalism does not depend on a specific choice. It should be noted that the convention in this thesis is that the mass m is the effective electronic mass.

The wavefunctions in the leads fulfill

$$\left[-\frac{\hbar^2}{2m}\left(\frac{\partial^2}{\partial x^2}+\frac{\partial^2}{\partial y^2}\right)+V_c(y)\right]\Psi(x,y;E)=E\Psi(x,y;E), \tag{2.2}$$

with the solution for subband m

$$e^{\pm ik_m x}\chi_m(y), \tag{2.3}$$

where k_m is the wavenumber in the x-direction for subband m. It describes a propagating wave if the wavenumber is a real number. The corresponding subband is then referred to as a propagating subband. It is otherwise an decaying exponential function if the wavenumber is an imaginary number. The corresponding subband is then referred to as an evanescent subband. The total energy of an electron in subband m is partitioned between the subband energy and the kinetic energy along the wire

$$E=\varepsilon_m+\frac{\hbar^2 k_m^2}{2m}. \tag{2.4}$$

The wavenumber is then

$$k_m^2=\frac{2m(E-\varepsilon_m)}{\hbar^2}, \tag{2.5}$$

so subband m is propagating if $E \geq \varepsilon_m$.

For a fixed energy E there is only a limited number of propagating subbands but an unlimited number of evanescent subbands. The number of propagating subbands will be denoted as $N_P(E)$ and the set of propagating subbands as $P(E)$. This can also be looked at from an another perspective by keeping the subband m fixed. There is then a cutoff or a threshold energy given by ε_m. The electrons can only propagate in that subband if their energy is higher or equal to the cutoff energy. This can be understood by inspecting the dispersion relations in the leads which are shown in figure 2.1. If the fixed energy is denoted by the horizontal black line the electrons can only propagate in the subbands where there is an intersection of the dispersion relations and the black line. Here are only elastic processes considered. Thus, in the leads, far from the scattering area, only the propagating subband take part in the transmission. Nevertheless, the evenscent subbands are extremely important and can not be ignored when investigating scattering in quantum wires. They can become localized inside the scattering area and have a great effect on the transmission and thus the conductance [9].

This is analogous to what is seen in a conventional waveguides in electromagnetism, where only certain transverse modes are allowed. These transverse modes are comparable to the subbands. The transverse modes are characterized by cutoff frequencies. There is only power and signal transmission in some mode if the frequency of the wave is higher than the cutoff frequency, resulting in a propagating wave. However, waves with lower frequency can not propagate in that mode [8].

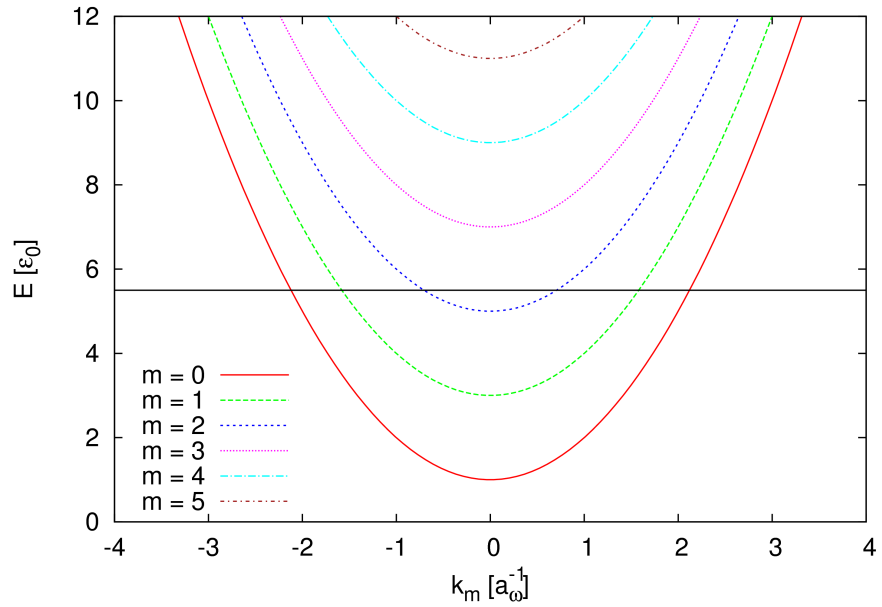

Figure 2.1: The dispersion relations in the leads for the lowest subband. If the fixed energy is denoted by the black line only subbands $m = 0, 1, 2$ allow propagation, the higher subbands are evanescent.

The analogy is of course due to the fact that the electrons are viewed as waves in quantum mechanics. However, the interpretations for these two types of waves are totally different.

Now, the total wavefunction in the leads is obtained by summing over all the subbands, propagating and evenscent

$$\Psi(x,y;E) = \begin{cases} \sum_m \left[A_m e^{ik_m x}\chi_m(y) + B_m e^{-ik_m x}\chi_m(y)\right], & (x,y) \in L, \\ \Psi(x,y;E), & (x,y) \in M, \\ \sum_m \left[C_m e^{ik_m x}\chi_m(y) + D_m e^{-ik_m x}\chi_m(y)\right], & (x,y) \in R, \end{cases} \tag{2.6}$$

where the L, M, and R denote the left lead, the scattering area, and the right lead, respectively.

A particular scattering state $\Psi_n(x,y;E)$ is now introduced. There are electrons with energy E and in propagating subband n incident from the left towards the scattering area where they get scattered. Generally can nothing be said about the scattering state inside the scattering area. However, asymptotically in the leads the electrons are either reflected into subband m with reflection amplitude $r_{m,n}(E)$ or transmitted into subband m with transmission amplitude $t_{m,n}(E)$. This setup is

shown in figure 2.2. The wavefunction of the scattering state is given by

$$\Psi_n(x,y;E) = \begin{cases} e^{ik_n x}\chi_n(y) + \sum_m r_{m,n}(E)e^{-ik_m x}\chi_m(y), & (x,y) \in L, \\ \Psi_n(x,y;E), & (x,y) \in M, \\ \sum_m t_{m,n}(E)e^{ik_m x}\chi_m(y), & (x,y) \in R. \end{cases} \tag{2.7}$$

Figure 2.3 shows the probability densities of the scattering states for the lowest two subbands where the incoming subband is only present, no reflection or band-mixing.

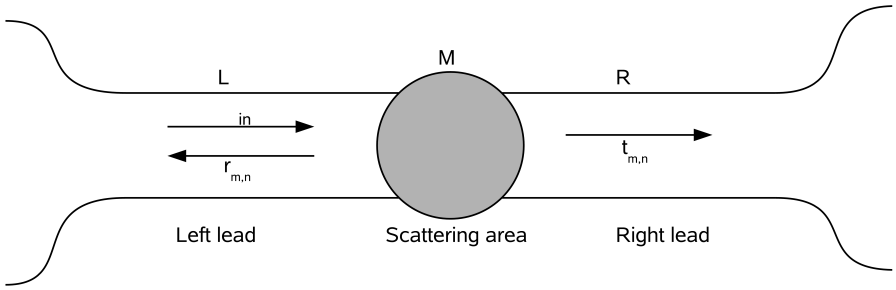

Figure 2.2: The setup of a scattering state $\Psi_n(x,y;E)$. Electrons with energy E and in subband m are incident from the left towards the scattering area where they get scattered. They are, asymptotically in the leads, either reflected into subband m with reflection amplitude $r_{m,n}(E)$ or transmitted into subband m with transmission amplitude $t_{m,n}(E)$.

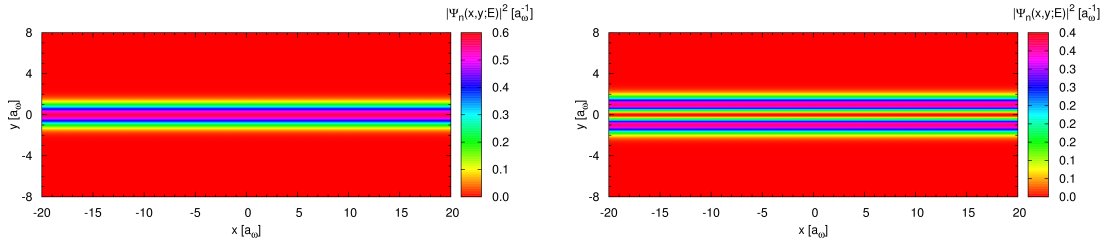

(a) $n = 0$ (b) $n = 1$

Figure 2.3: The probability densities of the scattering states for the lowest two subbands where only the incoming subband is present.

The transmission and reflection probabilities are related to the amplitudes by

$$T_{m,n}(E) = \frac{k_m}{k_n}|t_{m,n}(E)|^2, \tag{2.8}$$

and

$$R_{m,n}(E) = \frac{k_m}{k_n}|r_{m,n}(E)|^2, \tag{2.9}$$

where the prefactors are due to the normalization used for the wavefunctions.

The Landauer-Büttiker formalism states that electrons that are incident from the left in subband n and get transmitted into subband m contribute a factor of $(2e^2/h)T_{m,n}(E)$ to the conductance, here both n and m must be propagating subbands. The total conductance of the quantum wire is obtained by summing over all propagating subbands

$$G(E) = \frac{2e^2}{h}\sum_{n\in P(E)}\sum_{m\in P(E)} T_{m,n}(E) = G_0\sum_{n\in P(E)}\sum_{m\in P(E)}\frac{k_m}{k_n}|t_{m,n}(E)|^2, \tag{2.10}$$

where the energy is taken at the Fermi energy $E = \varepsilon_{\mathrm{F}}$ and the conductance unit $G_0 = 2e^2/h$ has been introduced. It should be noted that this is a zero temperature result and that the spin of the electrons is taken into account via the usual factor of 2. Note that the Landauer-Büttiker formalism does not specify how to obtain the transmission amplitudes.

In a clean quantum wire is $T_{m,n}(E) = \delta_{m,n}$. This results in $G(E) = N_P(E)$, the step like quantization of the conductance which can be seen in figure 3.1.

There is no need to assume that the wavenumbers are the same in the right and left lead but this will be useful later. The scattering state is then

$$\Psi_n(x,y;E) = \begin{cases} e^{ik_{L;n}x}\chi_n(y) + \sum_m r_{m,n}(E)e^{-ik_{L;m}x}\chi_m(y), & (x,y)\in L,\\ \Psi_n(x,y;E), & (x,y)\in M,\\ \sum_m t_{m,n}(E)e^{ik_{R;m}x}\chi_m(y), & (x,y)\in R. \end{cases} \tag{2.11}$$

There can now be different number of propagating subbands for the left and right lead so the notation $N_P(E)$ and $P(E)$ is extended to $N_{P;L}(E)$, $N_{P;R}(E)$, $P_L(E)$, and $P_R(E)$. The conductance is then

$$G(E) = G_0\sum_{n\in P_L}\sum_{m\in P_R} T_{m,n}(E) = G_0\sum_{n\in P_L}\sum_{m\in P_R}\frac{k_{R;m}}{k_{L;n}}|t_{m,n}(E)|^2. \tag{2.12}$$

Often, a current normalization, $1/\sqrt{k_m}$, is used for the wavefunctions [6]. The conductance is then quoted as

$$G(E) = G_0\sum_{n\in P}\sum_{m\in P}|t_{m,n}(E)|^2 = G_0\,\mathrm{Tr}\left[\mathbf{t}(E)^\dagger\mathbf{t}(E)\right], \tag{2.13}$$

where $\mathbf{t}$ is a $N_P \times N_P$ matrix of the transmission amplitudes $t_{m,n}$.

2.2 Quantum Wire System

Quantum wire systems are fabricated from a two-dimensional electron gas so the system is described by a two-dimensional Schrödinger equation

$$\left[-\frac{\hbar^2}{2m}\left(\frac{\partial^2}{\partial x^2}+\frac{\partial^2}{\partial y^2}\right)+V_{\mathrm{c}}(y)+V_{\mathrm{s}}(x)+V_{\mathrm{sc}}(x,y)\right]\Psi_n(x,y;E)=E\Psi_n(x,y;E), \quad (2.14)$$

where $V_{\mathrm{c}}(y)$ is the confinement potential and $V_{\mathrm{s}}(x)$ is a potential due to a step in the wire. The scattering potential $V_{\mathrm{sc}}(x,y)$ is localized and only different from zero inside the scattering area. Figure 2.4 shows the potential distribution of such a quantum wire system with an embedded quantum dot.

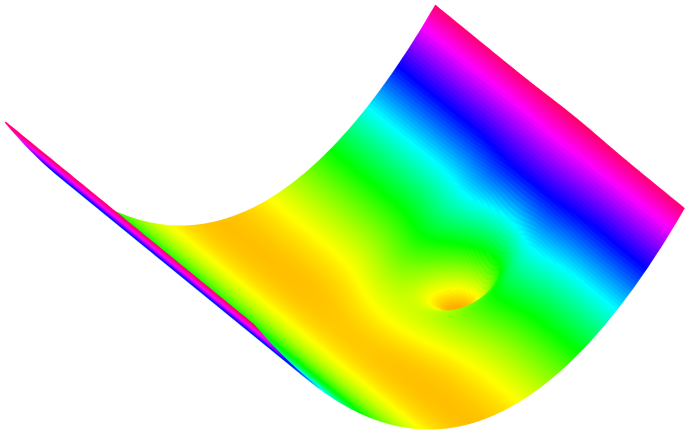

Figure 2.4: The potential distribution of a quantum wire system with an embedded quantum dot.

The scattering potential is used to describe the embedded nanostructure. It can, in principle, be any localized potential but the focus will be on potentials which are sums of Gaussian potentials

$$V_{\mathrm{sc}}(x,y)=\sum_i V_i e^{-[\beta_{x,i}(x-x_i)^2+\beta_{y,i}(y-y_i)^2]}. \quad (2.15)$$

The i-th Gaussian potential has the strength V_i, the center $(x_i,\ y_i)$ and $\beta_{\{x,y\},i}$ controls the range of the potential. Potential of this form can describe different kind of nanostructures, e.g. simple impurities, quantum dots or quantum rings.

New in the model is a step in the wire described by the potential $V_{\mathrm{s}}(x)$

$$V_{\mathrm{s}}(x) = V_{\mathrm{s}}\big[1 - \Theta(x)\big] = \begin{cases} V_{\mathrm{s}}, & x < 0, \\ 0, & x > 0, \end{cases} \tag{2.16}$$

where $V_{\mathrm{s}} > 0$ is the height or strength of the step and $\Theta(x)$ is the Heaviside function. The step can not be included in the scattering potential since it is not localized inside the scattering area. It can be thought of as a part of a model of a partial gate on top of the wire. It is of course unphysical to have such a sharp step in the wire as given by the Heaviside function. Some localized smoothing potential could be included in the scattering potential. The combination of the sharp step and the localized smoothing potential would produce a smoother, more realistic, step.

The scattering states in the leads fulfill

$$\left[-\frac{\hbar^2}{2m}\left(\frac{\partial^2}{\partial x^2} + \frac{\partial^2}{\partial y^2}\right) + V_{\mathrm{c}}(y) + V_{\mathrm{s}}(x)\right]\Psi_n(x, y; E) = E\Psi_n(x, y; E), \tag{2.17}$$

and are given by

$$\Psi_n(x, y; E) = \begin{cases} e^{ik_{L;n}x}\chi_n(y) + \sum\limits_m r_{m,n}(E)e^{-ik_{L;m}x}\chi_m(y), & (x, y) \in L, \\ \sum\limits_m t_{m,n}(E)e^{ik_{R;m}x}\chi_m(y), & (x, y) \in R. \end{cases} \tag{2.18}$$

Due to the step the wavenumbers are different in the left and right lead. The wavenumbers in the left lead are

$$k_{L;m}^2 = \frac{2m}{\hbar^2}(E - V_{\mathrm{s}} - \varepsilon_m), \tag{2.19}$$

so the requirement for propagation of subband m in the left lead is

$$E > V_{\mathrm{s}} + \varepsilon_m. \tag{2.20}$$

The wavenumbers in the right lead are, however,

$$k_{R;m}^2 = \frac{2m}{\hbar^2}(E - \varepsilon_m), \tag{2.21}$$

so the requirement for propagation of subband m in the right lead is

$$E > \varepsilon_m. \tag{2.22}$$

The thresholds where a new subband becomes propagating in the left lead are moved. Also, there are fewer propagating propagating subbands in the left lead than in the right lead where the difference depends on height of the step V_{s}.

2.3 Confinement Potential

A parabolic or harmonic oscillator potential is used to describe the confinement potential. Not only is this potential simple to implement but is also experimentally relevant for the confinement in some quantum wires fabricated from a two-dimensional electron gas.

The wavefunctions of the subbands fulfill

$$\left[-\frac{\hbar}{2m}\frac{d^2}{dy^2} + V_c(y)\right]\chi_m(y) = \varepsilon_m \chi_m(y), \tag{2.23}$$

where ε_m is the energy of subband m, the wavefunctions $\chi_m(y)$ are orthonormal, and the parabolic potential is

$$V_c(y) = \frac{1}{2}m\omega^2 y^2. \tag{2.24}$$

The solutions of equation (2.23) can be found in any introductory textbook on quantum mechanics [10]

$$\chi_m(y) = \frac{1}{(2^m m!\pi^{1/2}a_\omega)^{1/2}} H_m\left(\frac{y}{a_\omega}\right) e^{-y^2/2a_\omega^2}, \qquad m = 0, 1, 2, \dots, \tag{2.25}$$

where $a_\omega = (\hbar/m\omega)^{1/2}$ and has the dimension of length and $H_m(x)$ is the Hermite polynomial of order m [11, 12]. Figures 2.5 and 2.6 show the wavefunctions and the probability densities of the lowest subbands, respectively. The wavefunctions are symmetric for even n and antisymmetric for odd n. The energy of subband m is

$$\varepsilon_m = \left(m + \frac{1}{2}\right)\hbar\omega, \qquad m = 0, 1, 2, \dots, \tag{2.26}$$

and the difference between subbands is

$$\Delta\varepsilon = \Delta\varepsilon_m = \varepsilon_{m+1} - \varepsilon_m = \hbar\omega, \tag{2.27}$$

independent of m so there is always the same energy difference between subbands. The energy of the lowest subband is

$$\varepsilon_0 = \frac{1}{2}\hbar\omega = \frac{1}{2}\Delta\varepsilon = \frac{\hbar^2}{2m}\left(\frac{m\omega}{\hbar}\right) = \frac{\hbar^2}{2ma_\omega^2}. \tag{2.28}$$

As will be discussed in section 3.4 do ε_0 and a_ω define a convenient energy scale and length scale.

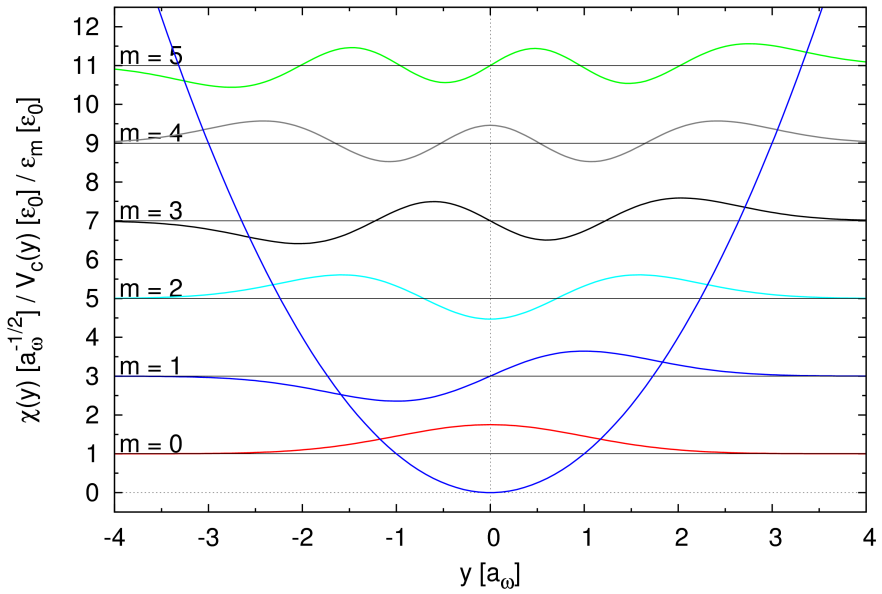

Figure 2.5: The wavefunctions of the lowest subbands for a parabolic confinement. The wavefunctions are offset in the y-direction. The parabolic potential is also shown.

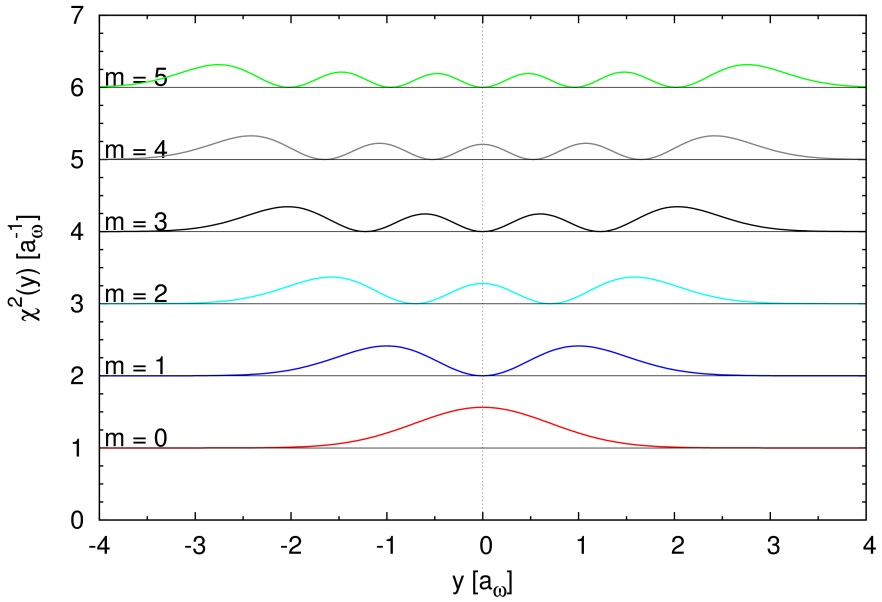

Figure 2.6: The probability densities of the lowest subbands for a parabolic confinement. The probability densities are offset in the y-direction.

Chapter 3

Scattering in Quantum Wires

Here, the second part of the theoretical framework is introduced. Classical time-independent Green's functions are first reviewed. Then, the conventional Lippmann-Schwinger scattering formalism is reviewed. Subsequently, the quasi-1D Lippmann-Schwinger scattering formalism is introduced. Finally, numerical scaling of units, which is important for numerical calculations, is discussed.

3.1 Classical Time-independent Green's Functions

Classical time-independent Green's functions are very advantageous when searching for general solutions to ordinary or partial differential equations [13]. These Green's functions have an extensive theory and a long history. The applications are numerous, e.g. in scattering theory [14], in electrodynamics [15], and many other fields where differential equations have to be solved.

The Green's function is a solution, subject to certain boundary conditions, of the operator equation

$$[z - L]G(z) = 1, \tag{3.1}$$

where $z = \lambda + is$ is a complex variable and the operator L is assumed time-independent, linear and Hermitian. If $\mathbf{r}$-represention is considered the Green's function is a solution to the differential equation

$$[z - L(\mathbf{r})]G(\mathbf{r}, \mathbf{r}'; z) = \delta(\mathbf{r} - \mathbf{r}'). \tag{3.2}$$

The operator L is assumed to posses a complete set of orthonormal eigenstates $|\phi_n\rangle$ with real eigenvalues λ_n. The eigenvalue spectra can both be discrete and/or continuous although the focus here will be on the continuous spectra.

The solution for the Green's function can be written formally as

$$G(z) = \frac{1}{z - L} = \sum_n \frac{|\phi_n\rangle \langle\phi_n|}{z - \lambda_n}, \quad z \neq \lambda_n, \tag{3.3}$$

where the completeness of the eigenstates is used in the second equality. The Green's function can be obtained by directly solving the differential equation subject to the appropriate boundary conditions or by using the spectral representation based on the formal solution above. The formal solution in the r-representation is

$$G(\mathbf{r},\mathbf{r}';z)=\sum_n \frac{\phi_n(\mathbf{r})\phi_n^*(\mathbf{r}')}{z-\lambda_n}+\int dc\,\frac{\phi_c(\mathbf{r})\phi_c^*(\mathbf{r}')}{z-\lambda_c}, \tag{3.4}$$

here is summed over the discrete spectra and integrated over the continuous spectra. The focus will now be on the case where there is only a continuous spectra with extended eigenfunctions. The Green's function $G(\mathbf{r},\mathbf{r}';\lambda)$ is not well defined if λ is a part of the continuous spectra since there is a pole in the integrand. This problem is sidestepped by using a limiting procedure

$$G^{\pm}(\mathbf{r},\mathbf{r}';\lambda)=\lim_{s\to 0^+} G(\mathbf{r},\mathbf{r}';\lambda\pm is). \tag{3.5}$$

The resulting integral can often be solved by the help of the Cauchy theorem and residue calculus [16]. The two Green's functions defined by the limiting procedure correspond to two different boundary conditions, this will be seen later.

The Green's function can be used to get information about the density of states, eigenvalues, and eigenfunctions of the operator L [13]. However, the most important application of the Green's function is to obtain a general solution to the inhomogeneous differential equation

$$[\lambda-L(\mathbf{r})]u(\mathbf{r})=f(\mathbf{r}), \tag{3.6}$$

where λ is in the continuous spectra of L and the boundary conditions are the same as for the Green's function. The general solution is given by the integral

$$u(\mathbf{r})=\phi(\mathbf{r})+\int d\mathbf{r}'\,G^{\pm}(\mathbf{r},\mathbf{r}';\lambda)f(\mathbf{r}'), \tag{3.7}$$

where $\phi(\mathbf{r})$ is a solution of the homogeneous differential equation

$$[\lambda-L(\mathbf{r})]\phi(\mathbf{r})=0, \tag{3.8}$$

subject to the same boundary conditions as the Green's function. It is easy to see that the solution to the inhomogeneous differential equation is given by equation (3.7), the original inhomogeneous differential equation is recovered by operating with $[\lambda-L(\mathbf{r})]$ on both sides of equation (3.7).

The advantages of the general solution are that the boundary conditions are directly built into it, it is usable for any function $f(\mathbf{r})$, and it is often easier to obtain a solution from it rather than directly solving the inhomogeneous differential equation.

A physical interpretation of the Green's function can be drawn by inspecting the inhomogeneous differential equation. If $u(\mathbf{r})$ describes the response of a system to a source $f(\mathbf{r})$ the Green's function $G^{\pm}(\mathbf{r},\mathbf{r}';\lambda)$ describes the response of the same system to a unit source at $\mathbf{r}'$ given by the delta function $\delta(\mathbf{r}-\mathbf{r}')$.

3.2 Conventional Lippmann-Schwinger Scattering Formalism

The conventional Lippmann-Schwinger scattering formalism in quantum mechanics is normally introduced when scattering is first discussed in textbooks on quantum mechanics [14, 17]. The ideal scattering experiment consist of a beam of particles incident along the z-direction towards a single fixed scattering volume where they are scattered. The scattered particles are detected at a distance $\mathbf{r}$ from the center at a scattering angle of $\Omega = (\theta, \phi)$. It is assumed that the interaction between the incoming particles and the scattering volume can be represented by a localized scattering potential $V(\mathbf{r})$ which is only different from zero inside a finite scattering volume. The most natural description of such a scattering experiment would be the time-dependent Schrödinger equation and wave packets. However, the simpler time-independent Schrödinger equation is adequate most of the time.

Assume, there is an incoming particle with energy E in the continuous energy spectrum which is incident along the z-direction. This particle is described with a wavefunction of a plane wave

$$\phi_{\mathbf{k}}(\mathbf{r}) = Ne^{i\mathbf{kr}} = Ne^{ikz}, \tag{3.9}$$

where N is an arbitrary normalization constant and the wavenumber k is given by

$$k = \sqrt{\frac{2mE}{\hbar^2}}. \tag{3.10}$$

This incoming wavefunction fulfills the Schrödinger equation for a free particle

$$\left[-\frac{\hbar^2}{2m}\nabla^2 \right] \phi_{\mathbf{k}}(\mathbf{r}) = E\phi_{\mathbf{k}}(\mathbf{r}). \tag{3.11}$$

The full wavefunction is a sum of the incoming wavefunction and a scattered wavefunction

$$\psi_{\mathbf{k}}(\mathbf{r}) = \phi_{\mathbf{k}}(\mathbf{r}) + \psi^{\mathrm{sc}}_{\mathbf{k}}(\mathbf{r}), \tag{3.12}$$

where the scattered wavefunction is an outgoing spherical wave. The asymptotic form of the full wavefunction for $r = |\mathbf{r}| \to \infty$ is

$$\psi_{\mathbf{k}}(\mathbf{r}) \sim N\left[e^{ikz} + f_E(\theta, \phi)\frac{e^{ikr}}{r} \right], \tag{3.13}$$

where $f_E(\theta, \phi)$ is the scattering amplitude. The scattering amplitude is generally a complex quantity so it is not directly observable in scattering experiments. The normal experimental observable is the differential cross section $d\sigma/d\Omega$ which is related to the scattering amplitude by

$$\frac{d\sigma}{d\Omega} = |f_E(\theta, \phi)|^2. \tag{3.14}$$

The differential cross section measures the strength of scattering into a detector at an angle (θ, ϕ) subtending a solid angle $d\Omega$ and has the dimensions of an area, or an area per solid angle. A comparison with one-dimensional scattering problems shows that the scattering amplitude is analogous to the transmission and reflection amplitudes. Furthermore, the differential cross section is analogous to the transmission and reflection probabilities.

The full wavefunction fulfills the Schrödinger equation for the scattering potential $V(\mathbf{r})$

$$\Big[-\frac{\hbar^2}{2m}\nabla^2 + V(\mathbf{r})\Big]\psi_{\mathbf{k}}(\mathbf{r}) = E\psi_{\mathbf{k}}(\mathbf{r}). \tag{3.15}$$

Note that this is not an eigenvalue equation, but a differential equation where the energy E is a continuous free parameter.

A free particle Green's function is defined as the solution to the differential equation

$$\big[k^2 + \nabla^2\big]G_0(\mathbf{r}, \mathbf{r}'; E) = \delta(\mathbf{r} - \mathbf{r}'). \tag{3.16}$$

Obtaining the solution from the spectral representation is an exercise in applying the Cauchy's theorem with the results [13, 14]

$$G_0^{\pm}(\mathbf{r}, \mathbf{r}'; E) = \frac{e^{\pm ik|\mathbf{r}-\mathbf{r}'|}}{4\pi|\mathbf{r} - \mathbf{r}'|}. \tag{3.17}$$

The boundary conditions of G_0^+ and G_0^- are that of a scattered wave radiating outwards from $\mathbf{r}'$ and that of a scattered wave radiating inwards to $\mathbf{r}'$, respectively. Thus, G_0^+ is the desired Green's function consistent with the boundary conditions of the scattering problem. It should be noted that the Green's function is invariant under an exchange of the coordinates and only depends on the magnitude of difference between them. This is a general property due to the fact that the free particle Hamiltonian is translation invariant and describes a isotropic space where waves propagate symmetrically [14].

The Schrödinger equation is rewritten as

$$\big[k^2 + \nabla^2\big]\psi_{\mathbf{k}}(\mathbf{r}) = V(\mathbf{r})\psi(\mathbf{r}), \tag{3.18}$$

for the full wavefunction, and

$$\big[k^2 + \nabla^2\big]\phi_{\mathbf{k}}(\mathbf{r}) = 0, \tag{3.19}$$

for the incoming wavefunction. The general solution to the scattering problem is then

$$\psi_{\mathbf{k}}(\mathbf{r}) = \phi_{\mathbf{k}}(\mathbf{r}) + \int d\mathbf{r}'\, G_0^+(\mathbf{r}, \mathbf{r}'; E)V(\mathbf{r}')\psi_{\mathbf{k}}(\mathbf{r}'), \tag{3.20}$$

which is an integral equation known as the Lippmann-Schwinger equation.

The scattering amplitude can be obtained from the asymptotic limit of the Lippmann-Schwinger equation for $r \gg r'$. Using the expansion

$$|\mathbf{r} - \mathbf{r}'| \approx r - \frac{\mathbf{r} \cdot \mathbf{r}'}{r}, \tag{3.21}$$

in the Lippmann-Schwinger equation and comparing with the asymptotic form of the full wavefunction results in

$$f_E(\theta, \phi) = -4\pi^2 \mu \int d\mathbf{r}' \, N e^{-i\mathbf{k}'\mathbf{r}'} V(\mathbf{r}') \psi(\mathbf{r}'), \tag{3.22}$$

where $\mathbf{k}' = k\hat{\mathbf{r}}$.

It should be noted that there nothing new about the Lippmann-Schwinger equation. It is just another represention of the Schrödinger equation and totally equivalent. It seems at first sight that there is not much gained by the Lippmann-Schwinger scattering formalism, the solution $\psi_{\mathbf{k}}(\mathbf{r})$ has to be known to obtain the solution $\psi_{\mathbf{k}}(\mathbf{r})$. However, there are many advantages to the Lippmann-Schwinger scattering formalism. The Lippmann-Schwinger equation is very favorable for numerical calculations and is also very open to approximations like the Born approximation and other higher order approximation. The formalism can be extended, e.g. to deal with non-local potential, relativity, many-particle effects, field theory and so on [14]. Specific example where the Lippmann-Schwinger formalism has been extended is an article by Ventra and Lang where the Lippmann-Schwinger equation is connected with density functional theory to obtain a self-consistent solution of transport in a nanoscale molecular conductors from first principles [18].

The Lippmann-Schwinger equation can also be derived in two and one dimensions [13]. The free particle Green's function for the two-dimensional case is

$$G_0^{\pm}(\mathbf{r}, \mathbf{r}'; E) = -\frac{i}{4} H_0^{(1)}(\pm k|\mathbf{r} - \mathbf{r}'|), \tag{3.23}$$

where $H_0^{(1)}$ is the Hankel function of the first kind of zero order. Furthermore, the free particle Green's function for the one-dimensional case is

$$G_0^{\pm}(x, x'; E) = \mp \frac{i}{2k} e^{\pm ik|x-x'|}. \tag{3.24}$$

These Green's functions also exhibit the general property of being invariant under an exchange of the coordinates and only depend on the magnitude of difference between the coordinates.

3.3 Quasi-1D Lippmann-Schwinger Scattering Formalism

The Landauer-Büttiker formalism introduced in chapter 2 connected the transmission of of electrons through a quantum wire with the conductance of the quantum wire. Only the transmission amplitudes $t_{m,n}(E)$ are needed to calculate the conductance. The transmission amplitudes are obtained with a quasi-1D Lippmann-Schwinger scattering formalism introduced here. A similar formalism has been introduced before [19, 20]. There was it constructed in momentum space using the T-matrix. Here, the formalism is constructed in configuration space. This is due to the step in the quantum wire introduced in section 2.2.

The scattering state $\Psi_n(x, y; E)$ introduced in section 2.1 fulfills the Schrödinger equation of the quantum wire system

$$\left[-\frac{\hbar^2}{2m}\left(\frac{\partial^2}{\partial x^2}+\frac{\partial^2}{\partial y^2}\right)+V_{\mathrm{c}}(y)+V_{\mathrm{s}}(x)+V_{\mathrm{sc}}(x,y)\right]\Psi_n(x,y;E)=E\Psi_n(x,y;E). \quad (3.25)$$

The scattering state is expanded in the subband wavefunctions

$$\Psi_n(x,y;E)=\sum_{m'}\varphi_{n;m'}(x;E)\chi_{m'}(y), \quad (3.26)$$

where $\varphi_{n;m'}(x;E)$ is the wavefunction in the x-direction for subband m. The following differential equations are obtained by inserting this expansion in the Schrödinger equation, multiplying with $\chi^*_m(x)$ and integrating over y

$$\left[\frac{d^2}{dx^2}+k^2_{R;m}-U_{\mathrm{s}}(x)\right]\varphi_{n;m}(x;E)=\sum_{m'}U_{m,m'}(x)\varphi_{n;m'}(x;E), \quad (3.27)$$

where

$$U_{\mathrm{s}}(x)=\frac{2mV_{\mathrm{s}}(x)}{\hbar^2}. \quad (3.28)$$

This is an infinite set of coupled ordinary differential equations for the wavefunctions $\varphi_{n;m}(x;E)$. The coupling between the different subbands is given by the matrix elements of the scattering potential with respect to the wavefunctions of the subbands

$$U_{m,m'}(x)=\frac{2m}{\hbar^2}V_{m,m'}(x)=\frac{2m}{\hbar^2}\int dy\,\chi^*_m(y)V_{\mathrm{sc}}(x,y)\chi_{m'}(y). \quad (3.29)$$

Some general properties can be stated about the matrix elements. The wavefunctions of the subbands are real so the matrix elements are invariant under exchange of m and m'

$$V_{m,m'}(x)=V_{m',m}(x). \quad (3.30)$$

Also, there can be selection rules for the matrix elements, e.g. if the scattering potential is symmetric in the y-direction is $V_{m,m'}(x)$ only different from zero for m and m' both even or both odd. Appendix B shows the derivation of the matrix elements for a Gaussian potential.

Solving these coupled ordinary differential equations directly in their current form is inconvenient. They are thus transformed into coupled integral equations by the use of a Green's function. The Green's function $G^{\mathrm{s}}_m(x, x'; E)$ takes the step into consideration and fulfills the differential equation

$$\left[\frac{d^2}{dx^2} + k^2_{R;m} - U_{\mathrm{s}}(x)\right] G^{\mathrm{s}}_m(x, x'; E) = \delta(x - x'), \tag{3.31}$$

with the boundary condition of an outgoing wave from x'. This Green's function is derived in Appendix A by solving the differential equation directly. It is given by

$$G^{\mathrm{s}}_m(x, x'; E) = \begin{cases} -\frac{i}{2k_{L;m}} e^{ik_{L;m}|x-x'|} \\ +\frac{i}{2k_{L;m}} \left(\frac{k_{R;m}-k_{L;m}}{k_{R;m}+k_{L;m}}\right) e^{-ik_{L;m}(x+x')}, & x < 0 \;\&\; x' < 0, \\ -\frac{i}{k_{R;m}+k_{L;m}} e^{-ik_{L;m}x + ik_{R;m}x'}, & x < 0 \;\&\; x' > 0, \\ -\frac{i}{k_{R;m}+k_{L;m}} e^{ik_{R;m}x - ik_{L;m}x'}, & x > 0 \;\&\; x' < 0, \\ -\frac{i}{2k_{R;m}} e^{ik_{R;m}|x-x'|} \\ -\frac{i}{2k_{R;m}} \left(\frac{k_{R;m}-k_{L;m}}{k_{R;m}+k_{L;m}}\right) e^{ik_{R;m}(x+x')}, & x > 0 \;\&\; x' > 0. \end{cases} \tag{3.32}$$

Due to the step the Hamiltonian is not translation invariant, thus the Green's function is not a function of the absolute value $|x - x'|$ as for the free particle Green's function. This is the reason that the formalism is constructed in configuration space and not in momentum space, the Green's function is not diagonal in momentum space as the free particle Green's function. It should be noted a similar Green's function has been derived in literature where the spectral representation was used [21, 22].

An unperturbed wavefunction $\varphi^0_{n;m}(x; E)$ satisfies the homogeneous differential equation

$$\left[\frac{d^2}{dx^2} + k^2_{R;m} - U_{\mathrm{s}}(x)\right] \varphi^0_{n;m}(x; E) = 0. \tag{3.33}$$

with the boundary condition of a electron in subband n incident from the left. In the absence of a scattering potential there is no coupling or band-mixing between different subbands. Thus, this is just a normal one-dimensional scattering problem

with the result

$$\varphi^0_{n;m}(x;E) = \begin{cases} \delta_{n,m}\left(e^{ik_{L;m}x} + \frac{k_{L;m}-k_{R;m}}{k_{L;m}+k_{R;m}}e^{-ik_{L;m}x}\right), & x' < 0, \\ \\ \delta_{n,m}\frac{2k_{L;m}}{k_{L;m}+k_{R;m}}e^{ik_{R;m}x}. & x' > 0, \end{cases} \tag{3.34}$$

Which in the absence of a step is the wavefunction of a free particle, as expected.

An infinite set of coupled one-dimensional Lippmann-Schwinger equations is then obtained

$$\varphi_{n;m}(x;E) = \varphi^0_{n;m}(x;E) + \sum_{m'}\int dx'\, G^{\mathrm{s}}_m(x,x';E)U_{m,m'}(x')\varphi_{n;m'}(x';E). \tag{3.35}$$

It should be noted that the coupled Lippmann-Schwinger equations conserve the normalization of the incident unperturbed wavefunction.

Although it is not used here can it be noted in passing that an equivalent two-dimensional Lippmann-Schwinger equation can be obtained. Multiplying with $\chi_m(y)$ and summing over m results in

$$\begin{aligned}\Psi_n(x,y;E) &= \Psi^0_n(x,y;E) \\ &\quad + \int dx' \int dy'\, G^{\mathrm{s}}(x,y,x',y';E)V_{\mathrm{sc}}(x',y')\Psi_n(x,y;E),\end{aligned} \tag{3.36}$$

where the unperturbed wavefunction is

$$\Psi^0_n(x,y;E) = \sum_m \varphi^0_{n;m}(x;E)\chi_m(y) = \varphi^0_{n;n}(x;E)\chi_n(y), \tag{3.37}$$

and the two-dimensional Green's function is

$$G^{\mathrm{s}}(x,y,x',y';E) = \frac{2m}{\hbar^2}\sum_m \chi^*_m(y)G^{\mathrm{s}}_m(x,x';E)\chi_m(y). \tag{3.38}$$

The wavefunctions $\varphi_{n;m}(x;E)$ can be related to the transmission amplitudes $t_{m,n}(E)$ by considering the asymptotic limit $x \gg 0$. The expansion $|x-x'| \approx x - x'$ for $x \gg 0$ is used for the Green's function so that

$$G^{\mathrm{s}}_m(x \gg 0, x';E) = e^{ik_{R;m}x}g^{\mathrm{s}}_m(x';E), \tag{3.39}$$

where

$$g^{\mathrm{s}}_m(x';E) = \begin{cases} -\frac{i}{k_{R;m}+k_{L;m}}e^{-ik_{L;m}x'}, & x' < 0 \\ \\ -\frac{i}{2k_m}\left[\frac{k_{R;m}-k_{L;m}}{k_{R;m}+k_{L;m}}e^{ik_{R;m}x} - e^{-ik_{R;m}x}\right], & x' > 0. \end{cases} \tag{3.40}$$

The scattering state is then

$$\begin{aligned}\Psi_n(x \gg 0, y; E) &= \sum_{m \in P_R(E)} \varphi_{n;m}(x \gg 0; E)\chi_m(y) = \sum_{m \in P_R(E)} \Bigg[\Bigg[\varphi^0_{n;m'}(x \gg 0; E) \\ &+ \sum_{m'} \int dx'\, G^{\mathrm{s}}_m(x \gg 0, x'; E) U_{m,m'}(x') \varphi_{n;m'}(x'; E) \Bigg] \chi_m(y) \Bigg] \\ &= \sum_{m \in P_R(E)} \Bigg[\Bigg[\delta_{m,n} \frac{2k_{L;m}}{k_{L;m} + k_{R;m}} + \sum_{m'} \int dx'\, g^{\mathrm{s}}_m(x'; E) U_{m,m'}(x') \varphi_{n;m'}(x'; E) \Bigg] \\ &\cdot e^{ik_{R;m}x} \chi_m(y) \Bigg]. \end{aligned} \tag{3.41}$$

The scattering state can also be written as

$$\Psi_n(x \gg 0, y; E) = \sum_{m \in P_R(E)} t_{m,n}(E) e^{ik_{R;m}x} \chi_m(y), \tag{3.42}$$

where the sum is only taken over the propagating subbands in the right lead since the evenscent subbands should all have vanished. The transmission amplitudes are obtained by comparing equations (3.41) and (3.42)

$$t_{m,n}(E) = \delta_{m,n} \frac{2k_{L;n}}{k_{L;n} + k_{R;n}} + \sum_{m'} \int dx'\, g^{\mathrm{s}}_m(x'; E) U_{m,m'}(x') \varphi_{n;m'}(x'; E), \tag{3.43}$$

where n and m are both propagating subbands.

In the absence of a scattering potential, i.e. for an unperturbed quantum wire, there is, due to the step, nevertheless scattering. The unperturbed transmission amplitude is

$$t^0_{m,n}(E) = \delta_{m,n} \frac{2k_{L;n}}{k_{L;n} + k_{R;n}}, \tag{3.44}$$

and thus the unperturbed conductance

$$G^0(E) = \sum_{n \in P_L(E)} \sum_{m \in P_R(E)} \delta_{m,n} \frac{4k_{L;n}k_{R;n}}{(k_{L;n} + k_{R;n})^2} = \sum_{n \in P_L(E)} \frac{4k_{L;n}k_{R;n}}{(k_{L;n} + k_{R;n})^2}. \tag{3.45}$$

The conductance of an unperturbed quantum wire is shown in figure 3.1 for few values of V_{s}. The thresholds where a new subband becomes propagating move higher in energy as the step height is increased and the step smears the conductance steps.

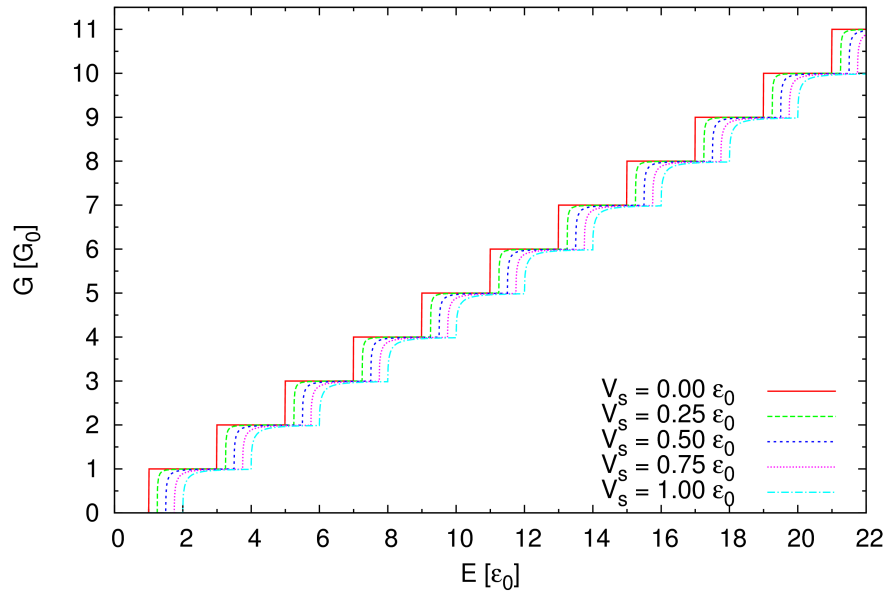

Figure 3.1: The conductance versus energy for unperturbed quantum wires for few values of the step height V_s.

In a numerical solution the total number of subbands has to be limited to a finite number N_m. This does not cause any problems if a sufficient number of evenscent subbands is always included. However, this should always be carefully checked. The numerical methods for solving these equations are introduced in appendix C. There is it shown that it is relative easy to transform the coupled Lippmann-Schwinger equations into a simple matrix equation suitable for numerical implementation. It should be noted that all numerical solutions in this thesis were implemented in Fortran 95.

3.4 Numerical Scaling

In numerical calculations is it convenient to utilize scaling so that all variables, parameters, and equations are scaled and thus dimensionless. The most obvious choice for the current case is the energy scale and length scale provided by the parabolic confinement potential. The energy scale is defined by the energy of the lowest subband $m = 0$

$$\varepsilon_0 = \frac{1}{2}\hbar\omega = \frac{1}{2}\Delta\varepsilon = \frac{\hbar^2}{2ma_\omega^2}. \tag{3.46}$$

The length scale is defined by the length a_ω

$$a_\omega = \left(\frac{\hbar^2}{2m\varepsilon_0}\right)^{1/2} = \left(\frac{\hbar}{m\omega}\right)^{1/2}. \tag{3.47}$$

There is really nothing special about this choice and in principle any related energy and length could be used. Another choice could be the Rydberg energy and Bohr radius. However, this choice makes the equations for the subbands very simple, as seen below.

The dimensionless variables are denoted as

$$\hat{E} = E/\varepsilon_0, \qquad \hat{x} = x/a_\omega, \qquad \hat{k}_{L;m} = k_{L;m}a_\omega, \qquad \hat{k}_{L;m}\hat{x} = k_{L;m}x,$$
$$\hat{V}(\hat{x},\hat{y}) = V(x,y)/\varepsilon_0, \qquad \frac{\partial}{\partial\hat{x}} = a_\omega\frac{\partial}{\partial x}, \qquad \frac{\partial^2}{\partial\hat{x}^2} = a_\omega^2\frac{\partial^2}{\partial x^2}. \tag{3.48}$$

The Schrödinger equation is transformed into a dimensionless equation, first obtaining

$$\left[-\frac{\hbar^2}{2ma_\omega^2}\left(\frac{\partial^2}{\partial\hat{x}^2}+\frac{\partial^2}{\partial\hat{y}^2}\right)+V_{\rm c}(y)+V_{\rm s}(x)+V_{\rm sc}(x,y)\right]\Psi_n(x,y;E) = E\Psi_n(x,y;E), \tag{3.49}$$

then

$$\left[-\left(\frac{\partial^2}{\partial\hat{x}^2}+\frac{\partial^2}{\partial\hat{y}^2}\right)+\hat{V}_c(\hat{y})+\hat{V}_s(\hat{x})+\hat{V}_{sc}(\hat{x},\hat{y})\right]\hat{\Psi}_n(\hat{x},\hat{y};\hat{E}) = \hat{E}\hat{\Psi}_n(\hat{x},\hat{y};\hat{E}). \tag{3.50}$$

where the equation has been divided by ε_0 and the dimensionless wavefunction $\hat{\Psi}_n(\hat{x},\hat{y};\hat{E})$ has been introduced.

The dimensionless subbands wavefunctions satisfy

$$\left[-\frac{d^2}{d\hat{y}^2}+\hat{V}_c(\hat{y})\right]\hat{\chi}_m(\hat{y}) = \hat{\varepsilon}_m\hat{\chi}_m(\hat{y}), \tag{3.51}$$

where the confinement potential is now

$$\hat{V}_c(\hat{y}) = \hat{y}^2. \tag{3.52}$$

The wavefunctions are

$$\hat{\chi}_m(\hat{y}) = \frac{1}{(2^m m!\pi^{1/2})^{1/2}}H_m(\hat{y})e^{-\hat{y}^2/2}, \qquad m = 0,1,2,\ldots \tag{3.53}$$

and the energies

$$\hat{\varepsilon}_m = \Big(2m+1\Big) = 1,3,5,\ldots, \qquad m = 0,1,2,\ldots \tag{3.54}$$

The dimensionless wavenumbers are

$$\hat{k}_{L;m}^2 = (\hat{E}-\hat{V}_s-\hat{\varepsilon}_m) = k_{L;m}^2a_\omega^2, \tag{3.55}$$

and

$$\hat{k}_{R;m}^2 = (\hat{E}-\hat{\varepsilon}_m) = k_{R;m}^2a_\omega^2. \tag{3.56}$$

One of the reasons for using dimensionless equations is that it leads to more stable numerical calculations as it minimizes the probability of over- and underflow errors. The calculations are also independent of exact material and experimental parameters. However, they should of course be kept in mind when choosing model parameters and analyzing results.

A connection to material and experimental parameters can be obtained by selecting a value for ε_0. If ε_0 is given in meV is a_ω given in nm as

$$a_\omega = \left(\frac{\hbar^2}{2m\varepsilon_0}\right)^{1/2} = \frac{6.176}{\hat{m}\varepsilon_0[\text{meV}]} \text{ nm}, \tag{3.57}$$

where $\hat{m}$ is the scaled effective mass which is $\hat{m} = 0.067$ for GaAs. The energy difference between subbands in a broad quantum wire fabricated from a GaAs two-dimensional electron gas is about $\Delta\varepsilon \approx 1$ meV. Then

$$\varepsilon_0 \approx 0.5 \text{ meV} \tag{3.58}$$

and

$$a_\omega \approx 33.7 \text{ nm}. \tag{3.59}$$

Chapter 4

Simple Model of a Closed Quantum Dot

Here, a simple model of a closed quantum dot is introduced. It is used to obtain a picture of the eigenstates of an isolated closed quantum dot which has a similar geometry or potential distribution as the open side-coupled quantum dots investigated in chapter 5. The foundation of this model is an infinite cylindrical well to which a perturbation potential is added to get the desired potential distribution. The linear variational calculus method is used to obtain a numerical solution of the model.

It should be noted that Macucci et al. investigated a similar system of interacting electrons in a two-dimensional quantum dot within density functional theory using a parabolic potential inside hard walls [23]. Their calculations are more sophisticated since the interaction between electrons is taken in account. However, they were mainly investigating the shell-filling effects and did not inspect the probability densities of the eigenstates.

The infinite cylindrical well has been used in simple models to explain some experiments. For example, the confinement of electrons to quantum corrals on a metal surface [24]. Furthermore, conductance oscillations in the electron transport through a quantum dot in a weak magnetic field [25].

This chapter will begin with a review of the linear variational calculus method. Subsequently, the model of the closed quantum dot will be introduced, Finally, the results are presented.

4.1 Linear Variational Calculus

There are very few quantum systems where an exact analytical solution to the Schrödinger equation can be obtained. Thus, most of the time must numerical calculation be utilized. In principle could some discretization method be used to solve the Schrödinger equation. However, this often leads to hefty calculations and there are many cases where other methods are much more efficient. Here, the variation

method, which is easy to implement for simple quantum system, will be introduced [26, 27].

The eigenvalue problem of the time-independent Schrödinger equation is given by

$$H\left|\Phi_\alpha\right\rangle = \varepsilon_\alpha \left|\Phi_\alpha\right\rangle, \qquad \alpha = 1, 2, 3, \ldots \tag{4.1}$$

where H is the Hamiltonian of the system, $|\Phi_\alpha\rangle$ is an eigenstate of the system with the corresponding eigenenergy ε_α. The eigenenergy spectrum of the Hamiltonian is assumed to discrete and ordered. The Hamiltonian is a Hermitian operator so the eigenenergies are real and the eigenstates are orthonormal. Furthermore, a complete set of eigenstates is assumed so that any general state can be written as a linear combinations of the eigenstates.

The foundation of the variation method is the variation principle that states the following [27]: Take a general trial state $|\tilde{\Phi}\rangle$ that satisfies the boundary conditions of the problem. Then, an upper bound of the ground state energy ε_1 is given by the expectation value of the Hamiltonian with regards to this trial state. Mathematically this is

$$\frac{\langle\tilde{\Phi}|H|\tilde{\Phi}\rangle}{\langle\tilde{\Phi}|\tilde{\Phi}\rangle} \geq \varepsilon_1, \tag{4.2}$$

where the equality sign is only valid if the trial state is the exact eigenstate of the ground state.

An estimate of the ground state energy can be found by introducing some general parametrized trial state and finding the minimum of $\langle\tilde{\Phi}|H|\tilde{\Phi}\rangle$ with regards to the parameters. But finding the minimum of $\langle\tilde{\Phi}|H|\tilde{\Phi}\rangle$ for a large number of parameters can be very difficult due to the high dimensional space to be minimized in. One way to sidestep this is to extend this method so the minimization problem is transformed to a matrix diagonalization.

This method is known as linear variational calculus [26, 27]. A set of N basis states $|\Psi_i\rangle$ is introduced and the $N \times N$ matrix H of the Hamiltonian is calculated in the basis of these basis states. An estimate of the lowest N eigenenergies and corresponding eigenstates of the quantum system is given by the eigenvalues and eigenvectors of this matrix. The eigenvalue problem is solved in the finite subspace spanned by the basis states $|\Psi_i\rangle$. In principle could an exact solution be obtained if an infinite number of basis states could be included and the resulting infinite matrix diagonalized. Thus, the accuracy of the method depends on the number and choice of basis functions.

The N basis states $|\Psi_i\rangle$ are assumed to be orthonormal

$$\langle\Psi_i|\Psi_j\rangle = \delta_{i,j}, \qquad i, j = 1, 2, \ldots, N. \tag{4.3}$$

The matrix elements of H are

$$H_{i,j} = \langle\Psi_i|H|\Psi_j\rangle. \tag{4.4}$$

The matrix H is Hermitian since the Hamiltonian is a Hermitian operator. Thus, the eigenvalues are real and the eigenvectors orthonormal. The eigenvalues fulfill

$$H\mathbf{c}^{\alpha} = E_{\alpha}\mathbf{c}^{\alpha}, \qquad \alpha = 1, 2, \ldots, N, \tag{4.5}$$

where the eigenvectors are

$$\mathbf{c}^{\alpha} = (c_1^{\alpha}, c_2^{\alpha}, \ldots, c_N^{\alpha}), \qquad \alpha = 1, 2, \ldots, N. \tag{4.6}$$

Here, the eigenvalues are ordered and can be degenerate. It can be shown that the eigenvalues of the matrix H give an upper bound for the lowest N eigenenergies of the quantum system described by the Hamiltonian H, i.e.

$$E_{\alpha} \geq \varepsilon_{\alpha}, \qquad \alpha = 1, 2, \ldots, N. \tag{4.7}$$

Also, the eigenvector $\mathbf{c}^{\alpha}$ give an approximate solution for the eigenstate $|\Phi_{\alpha}\rangle$ as a linear combination of the basis states

$$|\Phi_{\alpha}\rangle \approx |\tilde{\Phi}_{\alpha}\rangle = \sum_{i=1}^{N} = c_i^{\alpha} |\Psi_i\rangle . \tag{4.8}$$

It can be shown that these approximate states are orthonormal.

The assumption of an orthonormal basis states can be relaxed. Then the overlap matrix S is introduced

$$S_{i,j} = \langle \Psi_i | \Psi_j \rangle , \tag{4.9}$$

where $S_{i,j} = \delta_{i,j}$ for a orthonormal basis. A generalized eigenvalue problem is then obtained

$$H\mathbf{c}_{\alpha} = E_{\alpha} S \mathbf{c}_{\alpha}. \tag{4.10}$$

However, the overlap matrix can be transformed to the identity matrix with the help of a basis transformation resulting in a normal eigenvalue problem [26].

4.2 Closed Quantum Dot - Model

The model for the closed quantum dot is a two-dimensional model which can be partitioned into two parts. On one hand an infinite cylindrical well which is the unperturbed system. On the other hand a perturbation potential used to get the desired geometry consistent with the side-coupled quantum dots embedded in the quantum wire. The Hamiltonian is

$$H = H_0 + \lambda V', \tag{4.11}$$

where H_0 is the unperturbed Hamiltonian for an infinite cylindrical well, V' is the perturbation potential and λ is a perturbation parameter which ranges from 0, no perturbation, to 1, full perturbation.

Here, polar coordinates, r and θ, are the natural choice of coordinates. The unperturbed Hamiltonian is then

$$H_0 = -\frac{\hbar^2}{2m}\left(\frac{\partial^2}{\partial r^2} + \frac{1}{r}\frac{\partial}{\partial r} + \frac{1}{r^2}\frac{\partial^2}{\partial \theta^2}\right) + V_0(r,\theta) + B_{\mathrm{w}}, \tag{4.12}$$

where B_{w} is a parameter to offset the bottom of the infinite well and the hard wall potential is

$$V_0(r,\theta) = \begin{cases} 0, & r \le a_r, \\ \infty, & r > a_r, \end{cases} \tag{4.13}$$

where a_r is the radius of the well. The perturbation potential is

$$V'(r,\theta) = V_1(r,\theta) + V_2(r,\theta), \tag{4.14}$$

where

$$\begin{aligned} V_1(r,\theta) &= V_1(y-y_0)^2 = V_1(r\sin\theta - y_0)^2 \\ &= \frac{V_1}{4}\left[4y_0^2 - r^2(e^{2i\theta} + e^{-2i\theta} - 2) + 2iry_0(e^{i\theta} - e^{i\theta})\right], \end{aligned} \tag{4.15}$$

and

$$V_2(r,\theta) = V_2 r^2. \tag{4.16}$$

The potential $V_1(r,\theta)$ reproduces the slope due to the parabolic confinement potential in the quantum wire. Furthermore, the two-dimensional parabolic potential $V_1(r,\theta)$ should reproduce the Gaussian shape of the side-coupled quantum dots.

The boundary conditions of the eigenstates is that the corresponding wavefunctions must vanish at $r = a_r$ and must be finite at the origin $r = 0$. Also, the wavefunctions must be single valued with regards to the angular part so they are periodic in θ with a period of 2π.

The natural basis states are the eigenstates of an infinite cylindrical well which fullfill

$$H_0 \left|l,s\right\rangle = (\varepsilon^0_{l,s} + B_{\mathrm{w}}) \left|l,s\right\rangle, \tag{4.17}$$

and have the eigenenergies

$$\varepsilon^0_{l,s} + B_{\mathrm{w}} = \frac{\hbar^2 j^2_{l,s}}{2ma_r^2} + B_{\mathrm{w}}. \tag{4.18}$$

The corresponding eigenfunctions are

$$\psi_{l,s}(r,\theta) = \frac{1}{\sqrt{\pi}a_r J_{l+1}(j_{l,s})} J_l\Big(\frac{j_{l,s}r}{a_r}\Big)e^{il\theta}, \qquad \begin{matrix} l = 0, \pm1, \pm2, \pm3, \dots \\ s = 1, 2, 3, \dots \end{matrix}, \tag{4.19}$$

where $J_l(x)$ is the Bessel function of the first kind of order l [11,12]. The constant $j_{l,s}$ is root number s of $J_l(x)$, so that $J_l(j_{l,s}) = 0$. There is no analytical expression for the roots $j_{l,s}$ and the approximation is much too crude, tables are thus utilized [28, 29].

The unperturbed Hamiltonian is symmetric with regards to an exchange of x and y, this results in a two-fold degeneracy for all the eigenenergies where $l \neq 0$. The degeneracy is revealed in one of the properties of the Bessel functions which states that

$$J_{-l}(x) = (-1)^l J_l(x), \tag{4.20}$$

so that

$$j_{-l,s} = j_{l,s}. \tag{4.21}$$

This means that the eigenfunctions $\psi_{l,s}(r,\theta)$ and $\psi_{-l,s}(r,\theta)$ have the same eigenenergy but are linearly independent,

$$\begin{aligned}\psi_{-l,s}(r,\theta) &= \frac{(-1)^l}{\sqrt{\pi} a_r J_{l+1}(j_{l,s})} J_l\Big(\frac{j_{l,s} r}{a_r}\Big) e^{-il\theta} \\ &= (-1)^l \psi^*_{l,s}(r,\theta) = (-1)^l e^{-i2l\theta} \psi_{l,s}(r,\theta).\end{aligned} \tag{4.22}$$

However, it should be noted that these two eigenstates have the same probability density

$$|\psi_{l,s}(r,\theta)|^2 = |\psi_{-l,s}(r,\theta)|^2 = \frac{1}{\pi a_r^2 J_{l+1}^2(j_{l,s})} J_l^2\Big(\frac{j_{l,s} r}{a_r}\Big). \tag{4.23}$$

The probability densities are independent of the angle θ. This is due to the fact that the unperturbed Hamiltonian is independent of θ. Thus, there is no preferred direction in the system.

The asymptotic form of the Bessel functions for small values is

$$J_n(x) \approx \frac{1}{\Gamma(n+1)} \left(\frac{x}{2}\right)^n, \qquad x \ll 1. \tag{4.24}$$

This shows that only the eigenstates where $l = 0$ have a non-zero probability at the origin $r = 0$.

The basis states are obviously orthonormal

$$\begin{aligned}\langle l', s' | l, s \rangle &= \int_0^{2\pi} d\theta \int_0^{a_r} dr\, r \psi^*_{l',s'}(r,\theta) \psi_{l,s}(r,\theta) \\ &= \frac{1}{\pi a_r^2 J_{l'+1}(j_{l',s'}) J_{l+1}(j_{l,s})} \underbrace{\int_0^{2\pi} d\theta\, e^{i(l-l')\theta}}_{=2\pi\delta_{l',l}} \int_0^{a_r} dr\, r J_{l'}\Big(\frac{j_{l',s'} r}{a_r}\Big) J_l\Big(\frac{j_{l,s} r}{a_r}\Big) \\ &= \frac{2\delta_{l',l}}{a_r^2 J_{l+1}(j_{l,s'}) J_{l+1}(j_{l,s})} \int_0^{a_r} dr\, r J_{l'}\Big(\frac{j_{l',s'} r}{a_r}\Big) J_l\Big(\frac{j_{l,s} r}{a_r}\Big) = \delta_{l',l}\delta_{s',s},\end{aligned} \tag{4.25}$$

where the orthogonality property of the Bessel functions was used in the last step.

The matrix elements of the perturbation potential V' in this basis are given by

$$\langle l', s'|V'|l, s\rangle = \int_0^{2\pi} d\theta \int_0^{a_r} dr\, r\psi^*_{l',s'}(r,\theta)V_1(r,\theta)\psi_{l,s}(r,\theta) + \int_0^{2\pi} d\theta \int_0^{a_r} dr\, r\psi^*_{l',s'}(r,\theta)V_2(r,\theta)\psi_{l,s}(r,\theta), \tag{4.26}$$

where

$$\int_0^{2\pi} d\theta \int_0^{a_r} dr\, r\psi^*_{l',s'}(r,\theta)V_1(r,\theta)\psi_{l,s}(r,\theta) = V_1\left[\frac{a_r^2}{2}N_{l's',ls}(2\delta_{l'l} - \delta_{(l'-2)l} - \delta_{(l'+2)l}) + iy_0a_rM_{l's',ls}(\delta_{(l'-1)l} - \delta_{(l'+1)l}) + y_0^2\delta_{l'l}\delta_{s's}\right], \tag{4.27}$$

and

$$\int_0^{2\pi} d\theta \int_0^{a_r} dr\, r\psi^*_{l',s'}(r,\theta)V_2(r,\theta)\psi_{l,s}(r,\theta) = 2V_2a_r^2N_{l's',ls}\delta_{l',l}. \tag{4.28}$$

Here, the integrals

$$N_{l',s';l,s} = \frac{1}{J_{l'+1}(j_{l',s'})J_{l+1}(j_{l,s})}\int_0^1 dv\, v^2J_{l'}(j_{l',s'}v)J_l(j_{l,s}v), \tag{4.29}$$

and

$$M_{l',s';l,s} = \frac{1}{J_{l'+1}(j_{l',s'})J_{l+1}(j_{l,s})}\int_0^1 dv\, v^3J_{l'}(j_{l',s'}v)J_l(j_{l,s}v), \tag{4.30}$$

have been defined but they will be solved with numerical integration.

The matrix elements of the perturbed Hamiltonian are then given by

$$\langle l', s'|H|l, s\rangle = (\varepsilon^0_{l,s} + B_{\mathrm{w}})\delta_{l'l}\delta_{s's} + \lambda\left[V_1\left[\frac{a_r^2}{2}N_{l's',ls}(2\delta_{l'l} - \delta_{(l'-2)l} - \delta_{(l'+2)l}) + iy_0a_rM_{l's',ls}(\delta_{(l'-1)l} - \delta_{(l'+1)l}) + y_0^2\delta_{l'l}\delta_{s's}\right] + 2V_2a_r^2N_{l's',ls}\delta_{l'l}\right] \tag{4.31}$$

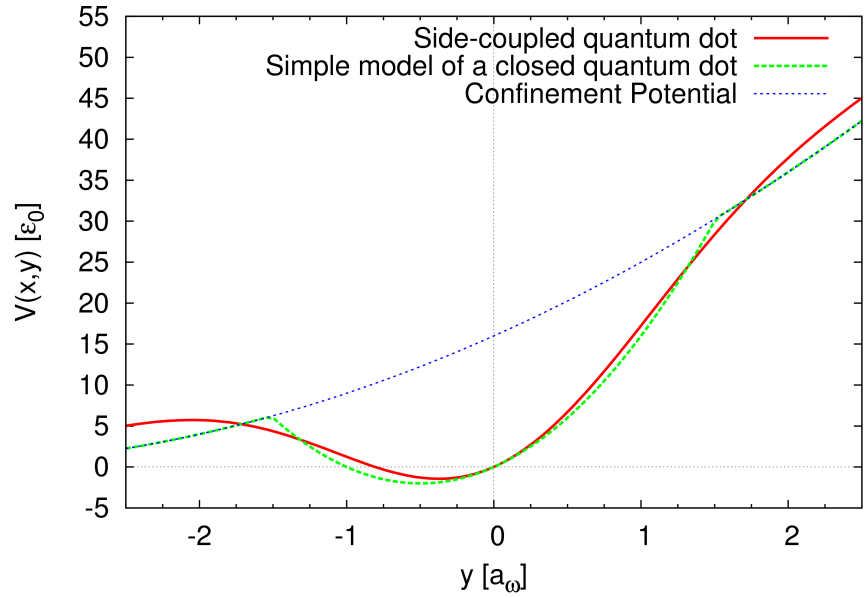

Figure 4.1: Comparison of the potential distribution of a side-coupled quantum dot and the simple model of a closed quantum dot. The cross section along the y-direction at the middle of the quantum dots

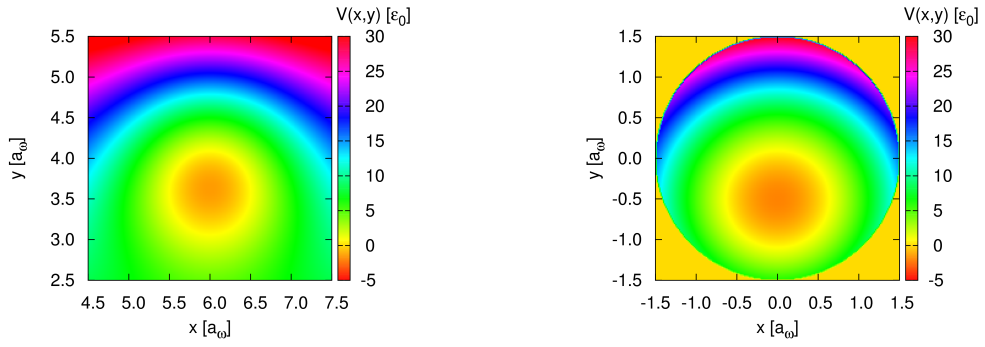

(a) Side-coupled quantum dot

(b) Simple model of a closed quantum dot

Figure 4.2: Comparison of the potential distribution of a side-coupled quantum dot and the simple model of a closed quantum dot.

Table 4.1: The eigenenergies of the unperturbed Hamiltonian, i.e. the infinite cylindrical well.

i	l	s	$j_{l,s}$	$\varepsilon^0_{l,s}$	$\varepsilon^0_{l,s} + B_{\mathrm{SCQD}}$
1	0	1	2.4048	2.5703	-13.4297
2	-1	1	3.8317	6.5253	-9.4747
3	1	1	3.8317	6.5253	-9.4747
4	-2	1	5.1356	11.7221	-4.2779
5	2	1	5.1356	11.7221	-4.2779
6	0	2	5.5201	13.5428	-2.4572
7	-3	1	6.3802	18.0918	2.0918
8	3	1	6.3802	18.0918	2.0918
9	1	2	7.0156	21.8749	5.8749
10	-1	2	7.0156	21.8749	5.8749
11	-4	1	7.5883	25.5924	9.5924
12	4	1	7.5883	25.5924	9.5924
13	2	2	8.4172	31.4889	15.4889
14	-2	2	8.4172	31.4889	15.4889
15	0	3	8.6537	33.2831	17.2831
16	-5	1	8.7715	34.1951	18.1951
17	5	1	8.7715	34.1951	18.1951
18	-3	2	9.7610	42.3456	26.3456
19	3	2	9.7610	42.3456	26.3456
20	-6	1	9.9361	43.8783	27.8783
21	6	1	9.9361	43.8783	27.8783
22	-1	3	10.1735	45.9998	29.9998
23	1	3	10.1735	45.9998	29.9998
24	-4	2	11.0647	54.4124	38.4124
25	4	2	11.0647	54.4124	38.4124
26	-7	1	11.0864	54.6256	38.6256
27	7	1	11.0864	54.6256	38.6256
28	2	3	11.6198	60.0092	44.0092
29	-2	3	11.6198	60.0092	44.0092
30	0	4	11.7915	61.7957	45.7957

The unperturbed eigenstates depend on two quantum number so it is convenient to define

$$\langle i|H|j\rangle = \langle l'(i), s'(i)|H|l(j), s(j)\rangle \,. \tag{4.32}$$

Here, the unperturbed eigenstates are ordered by the eigenenergies and the convention is that for degenerate eigenenergies the negative value of l comes first. This ordering can be seen in table 4.1.

Lengths and energies are scaled in units of the parabolic confinement of the quantum wire, ε_0 and a_ω, defined in section 3.4. The following parameters are used in the calculations

$$\begin{array}{lll} a_r = 1.5\, a_\omega, & B_{\mathrm{w}} = -16.0\, \varepsilon_0, & V_1 = 1.0\, \varepsilon_0, \\ y_0 = -4.0\, a_\omega, & V_2 = 7.0\, \varepsilon_0. & \end{array} \tag{4.33}$$

These parameters give the desired potential distribution as shown in figures 4.1 and 4.2. In table 4.1 the lowest 30 eigenenergies of the unperturbed Hamiltonian are shown for these parameters.

4.3 Closed Quantum Dot - Results

The 68 lowest eigenstates of the infinite cylindrical well were included in the calculations. This gives good accuracy for the lowest eigenstates of the perturbed system, as tested by including a smaller number of basis states.

The unperturbed system is first inspected, i.e. the infinite cylindrical well. Figure 4.3 shows the lowest eigenenergies. Figures 4.4 and 4.5 show the probability densities for the lowest six eigenstates.

Some of the properties of the eigenstates noted above can be seen. The degenerate eigenstates have the same probability density although they are linearly independent. There is only a non-zero probability at the center of the cylindrical well for eigenstates where $l = 0$. The probability densities are independent of the angle θ.

The infinite cylindrical well is a two-dimensional quantum dot where the eigenstates give the electron structure for non-interacting electrons. According to the Pauli principle only two electrons can occupy each eigenstate, one with spin up and one with spin down. Thus, the eigenenergies in figure 4.3 show an indication of closed shells for $2, 6, 12, 24$ electrons and weaker subshells for 16 and 20 electrons.

The perturbed system is now inspected. Figure 4.6 shows how the eigenenergies for the lowest six eigenstates change as a function of the perturbation parameter λ. The lowest eigenenergies are shown in figure 4.7. Furthermore, figures 4.8 and 4.9 show the lowest six eigenstates.

The perturbation lifts the degeneracy of the eigenenergies. This is expected since the perturbed Hamiltonian is not symmetric with regards to an exchange of x and y as the unperturbed Hamiltonian is. Few other things about the eigenstates can be noted. The probability densities now depend on the angle θ but this is expected

since the perturbation potential depends on θ. Also, the probability is higher for lower values of y. This is due to the slope that the perturbation potential introduces and reproduces the parabolic confinement potential in the quantum wire.

Figure 4.7 shows indications of closed shells for $2, 6, 12, 20, 24, \ldots$ electrons with a stronger shell for 20 electrons than for the infinite cylindrical well. This can be understood by the fact that the two-dimensional parabolic potential, which is part of the perturbation potential, has closed shells for $2, 6, 12, 20, 30, \ldots$ electrons. So there is a mixture of the shell structure of the infinite cylindrical well and a two-dimensional parabolic potential. This result for the shell structure is similar to the result obtained by Macucci et al [23].

This model is a single-particle one but that should not pose any problems since the quasi-1D Lippmann-Schwinger scattering formalism is also in the single-particle picture. It is thus expected that the model is adequate for characterizing the quasi-bound states seen in the open side-coupled quantum dots investigated in chapter 5.

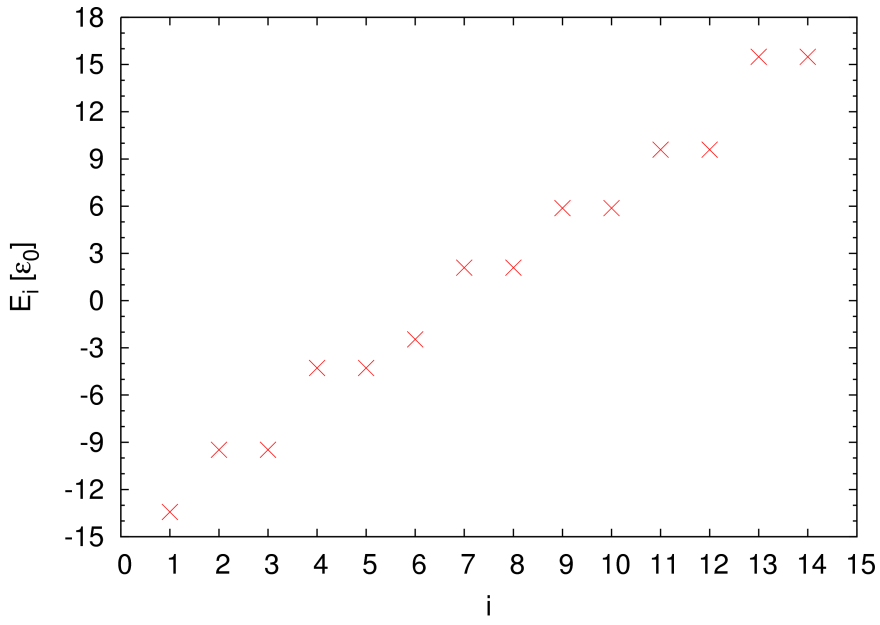

Figure 4.3: The eigenenergies for the unperturbed Hamiltonian, i.e. infinite cylindrical well.

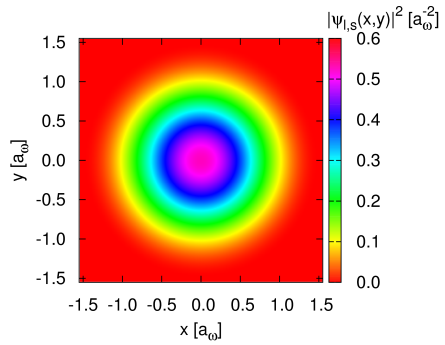

(a) Eigenstate $i = 1$, $(l = 0,\ s = 1)$

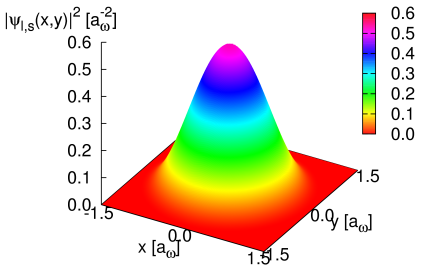

(b) $E_i = \varepsilon^0_{l,s} + B_{\mathrm{SCQD}} = -13.43\,\varepsilon_0$

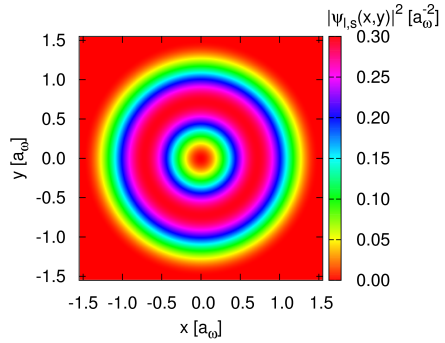

(c) Eigenstate $i = 2$, $(l = -1,\ s = 1)$

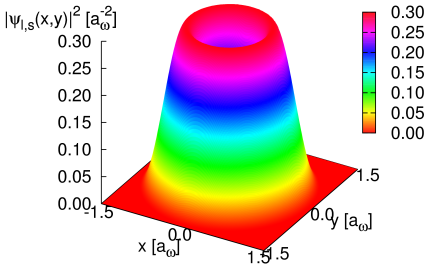

(d) $E_i = \varepsilon^0_{l,s} + B_{\mathrm{SCQD}} = -9.47\,\varepsilon_0$

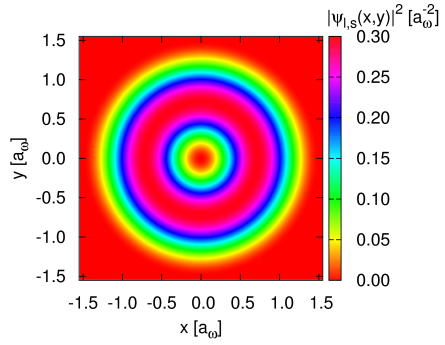

(e) Eigenstate $i = 3$, $(l = 1,\ s = 1)$

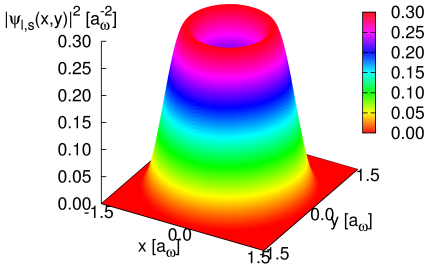

(f) $E_i = \varepsilon^0_{l,s} + B_{\mathrm{SCQD}} = -9.47\,\varepsilon_0$

Figure 4.4: The probability densities of the eigenstates for the unperturbed Hamiltonian, i.e. infinite cylindrical well.

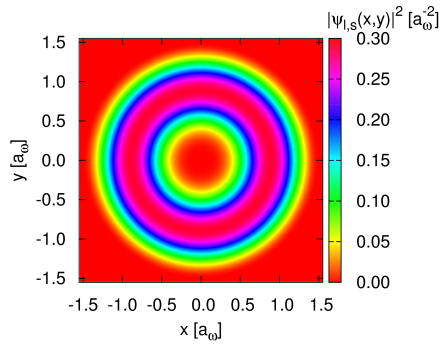

(a) Eigenstate $i = 4$, $(l = -2,\ s = 1)$

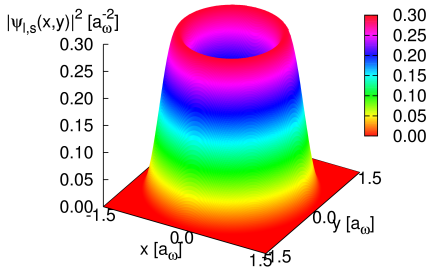

(b) $E_i = \varepsilon^0_{l,s} + B_{\mathrm{SCQD}} = -4.28\,\varepsilon_0$

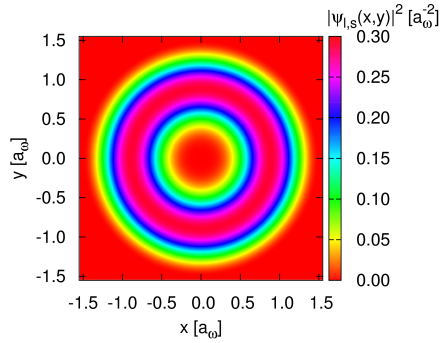

(c) Eigenstate $i = 5$, $(l = 2,\ s = 1)$

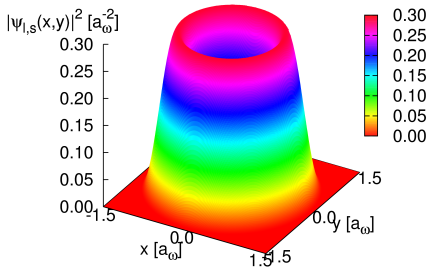

(d) $E_i = \varepsilon^0_{l,s} + B_{\mathrm{SCQD}} = -4.28\,\varepsilon_0$

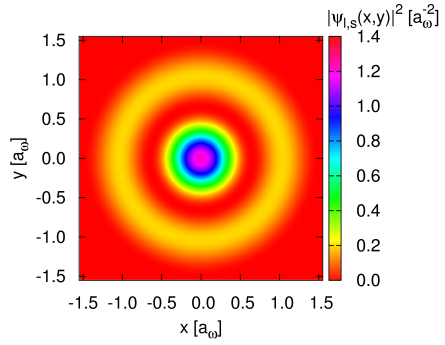

(e) Eigenstate $i = 6$, $(l = 0,\ s = 2)$

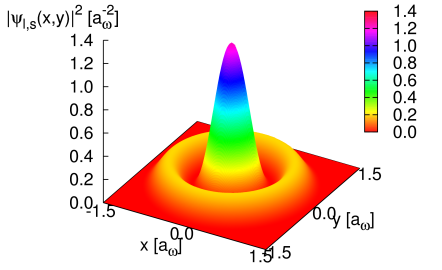

(f) $E_i = \varepsilon^0_{l,s} + B_{\mathrm{SCQD}} = -2.46\,\varepsilon_0$

Figure 4.5: The probability densities of the eigenstates for the unperturbed Hamiltonian, i.e. infinite cylindrical well.

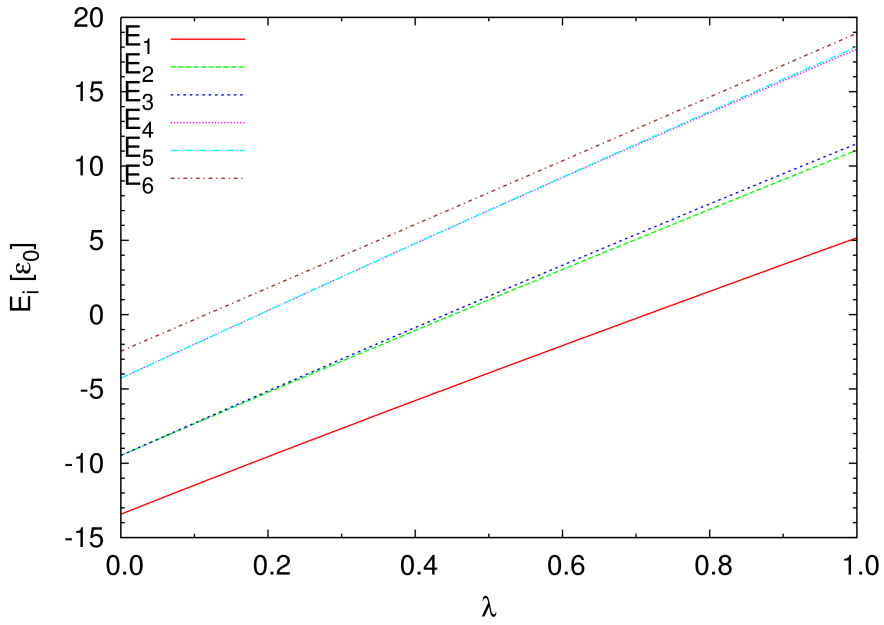

Figure 4.6: The eigenenergies of the lowest 6 eigenstates as a function of the perturbation parameter λ. The perturbation lifts the degeneracy.

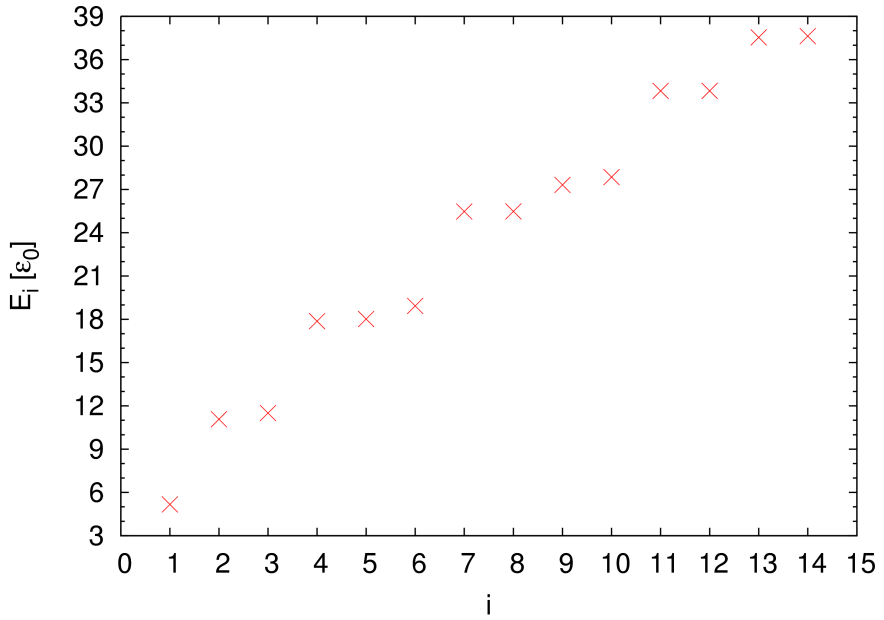

Figure 4.7: The eigenenergies for the perturbed Hamiltonian, the infinite cylindrical well with perturbation potential.

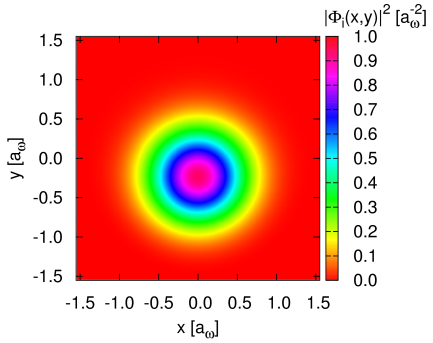

(a) Eigenstate $i = 1$

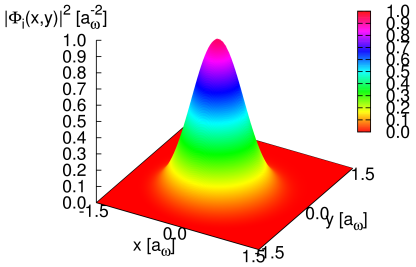

(b) $E_i = -5.17\,\varepsilon_0$

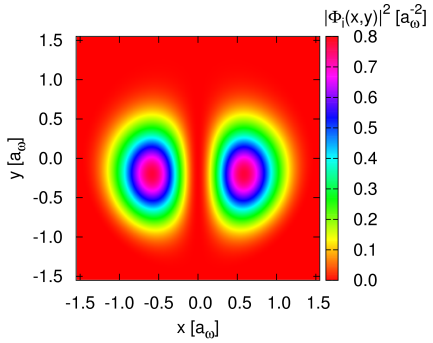

(c) Eigenstate $i = 2$

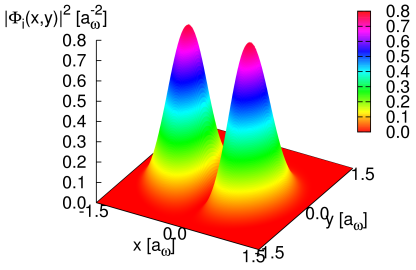

(d) $E_i = -11.07\,\varepsilon_0$

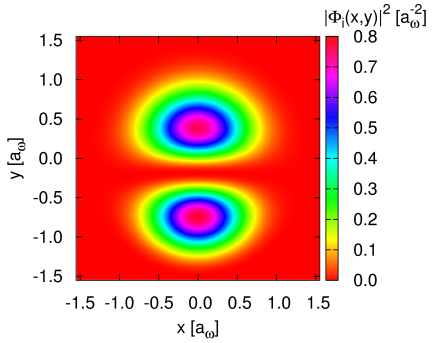

(e) Eigenstate $i = 3$

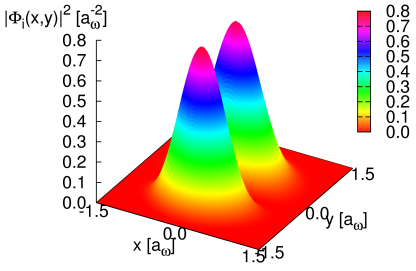

(f) $E_i = -11.51\,\varepsilon_0$

Figure 4.8: The probability densities of the eigenstates for the perturbed Hamiltonian, the infinite cylindrical well with perturbation potential.

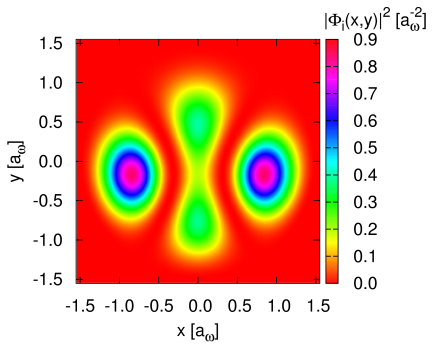

(a) Eigenstate $i = 4$

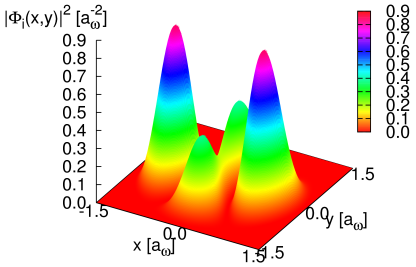

(b) $E_i = -17.87\,\varepsilon_0$

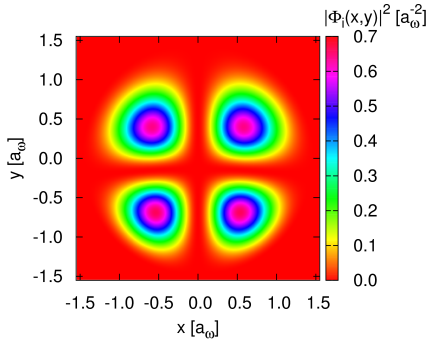

(c) Eigenstate $i = 5$

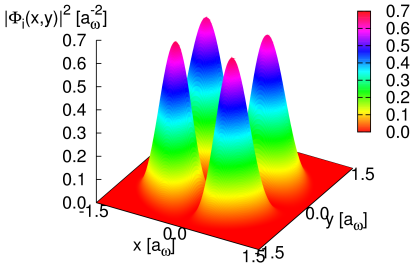

(d) $E_i = -18.02\,\varepsilon_0$

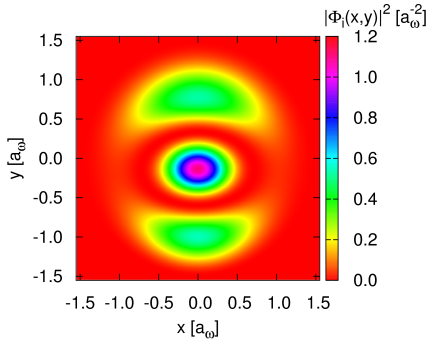

(e) Eigenstate $i = 6$

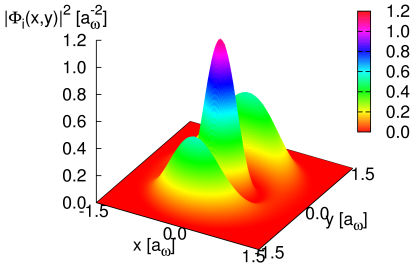

(f) $E_i = -18.93\,\varepsilon_0$

Figure 4.9: The probability densities of the eigenstates for the perturbed Hamiltonian, the infinite cylindrical well with perturbation potential.

Chapter 5

Quantum Wires with Side-coupled Quantum Dots

The theoretical framework introduced in chapters 2 and 3 will now be used to investigate transport in various quantum wire systems. All the investigated systems have a central theme. Quantum dots are embedded to the sides of the wire, far from the center. Thus, the systems can be viewed as quantum wires which are side-coupled to the open quantum dots as shown in the schematics in figure 5.1. They are referred to as quantum wires with side-coupled quantum dots. Analogous systems have recently been fabricated and experimentally investigated by the group of Kobayashi at the University of Tokyo in Japan [30, 31].

Theoretical investigations into such system have so far mainly been performed using an impurity Anderson model where the finer details of the geometry were not taken in account [32–35]. However, the quasi-1D Lippmann-Schwinger scattering formalism accounts for all the details of the geometry of the quantum wire systems. This advantage will be applied to focus on geometrical effects in transport through the quantum wire systems. Also, the ability of the quasi-1D Lippmann-Schwinger scattering formalism to visualize the scattering states will be used to obtain a greater understanding of the transport.

The geometrical effects are due to the total geometry of the systems which is a combination of the confinement, the side-coupled quantum dots, and possibly the step. The geometry can induce discrete resonance or quasi-bound states, i.e. bound states with a finite lifetime. A simple picture of a quasi-bound state is shown in figure 5.2 for a one-dimensional potential. There is the quasi-bound state a bound state in the well that can tunnel or leak out of the well. Also, the concept of a bound state in the continuum is shown but it will be discussed in detail in section 5.4.

The interplay between the extended states in the quantum wire and the quasi-bound states gives rise to resonances in the conductance. Due to the Heisenberg uncertainty principle the resonance widths are inversely proportional to the lifetime of the quasi-bound states. It is expected that quantum wires with side-coupled quantum dots show a rich structure in the conductance. This is due to the quasi-

bound states in the side-coupled quantum dots.

A simple model of an isolated closed quantum dot which has a similar geometry as the side-coupled quantum dots was introduced in chapter 4. This model can be used to characterize the quasi-bound states in the side-coupled quantum dots. It should be noted that the quantum wire systems are open systems so the side-coupled quantum dots are open quantum dots. Thus, the connection between the quasi-bound states and the eigenstates of the closed quantum dot is not always clear.

Transport in quantum wires with embedded quantum dots have been investigated with a similar formalism before [20,36]. However, the quantum dots were there much closer to the center of the wire and the step in the wire was not included.

The first system investigated is a quantum wire with a single side-coupled quantum dot, first without a step and then with a step. The step can be thought of as a part of a model of a partial gate on top of the wire. Subsequently, a quantum wire with two side-coupled quantum dots is investigated, first with identical dots and then where the dots are detuned relative to each other.

The calculations where done with scaled units as discussed in section 3.4. Thus, they are in principle independent of material and experimental parameters. However, they were of course kept in mind when choosing model parameters. The quantum wires are considered to be broad quantum wires fabricated from a two-dimensional electron gas in GaAs. Then is $\varepsilon_0 \approx 0.5$ meV and $a_\omega \approx 33.7$ nm.

All the calculation were made using $N_m = 20$ subbands, $N_x = 301$ grid points and a cutoff of $x_{\max} = 20\, a_\omega$. Numerical accuracy was carefully checked by increasing the number of subbands and grid points.

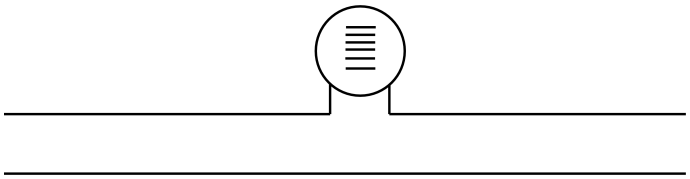

(a) Single side-coupled quantum dot

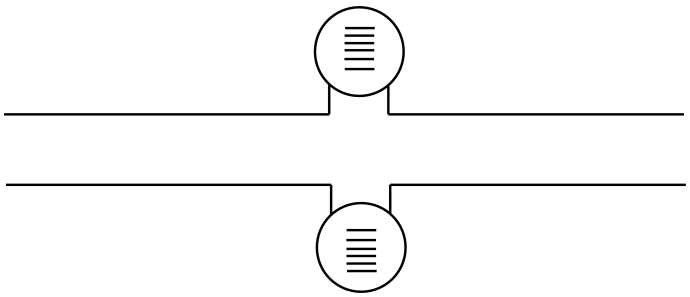

(b) Two side-coupled quantum dots

Figure 5.1: Schematics of quantum wires with side-coupled quantum dots.

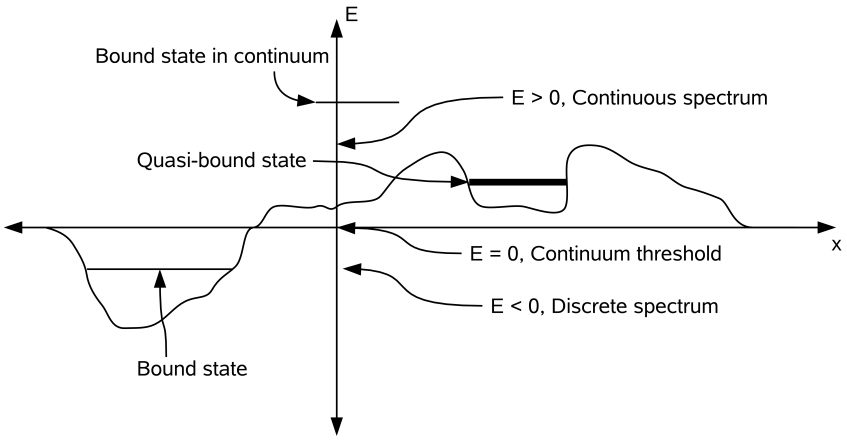

Figure 5.2: A simple picture of bound states, quasi-bound states and bound states in the continuum for a one-dimensional potential. The concept of a bound states in the continuum is discussed in detail in section 5.4

5.1 Single Quantum Dot

The transport through a quantum wire with a single side-coupled quantum dot is now investigated. The scattering potential describing the single side-coupled quantum dot is a sum of two Gaussian potentials

$$V_{\mathrm{sc}}(x,y) = V_1 e^{-[\beta_{x,1}(x-x_1)^2+\beta_{y,1}(y-y_1)^2]} + V_2 e^{-[\beta_{x,2}(x-x_2)^2+\beta_{y,2}(y-y_2)^2]}, \tag{5.1}$$

where the parameters are

$$\begin{array}{llll} V_1 = -36.0\,\varepsilon_0, & x_1 = 6.0\,a_\omega, & y_1 = 4.0\,a_\omega, & \beta_{x,1} = \beta_{y,1} = 0.4\,a_\omega^{-2}, \\ V_2 = 20.0\,\varepsilon_0, & x_2 = 6.0\,a_\omega, & y_2 = 4.0\,a_\omega, & \beta_{x,2} = \beta_{y,2} = 0.2\,a_\omega^{-2}. \end{array} \tag{5.2}$$

Figures 5.3 and 5.4 show the potential distribution of the quantum wire system. Figure 5.5 shows the cross section of the potential distribution along the transverse y-direction at the middle of the quantum dot at $x = 6\,a_\omega$. There is a tunneling barrier between the bottom of the wire and the dot. Also, the dot introduces a small constriction in the wire around $x = 6\,a_\omega$. The scattering potential is not symmetric in the y-direction so there are no selection rules for the matrix elements $V_{m,m'}(x)$ as for the case of a symmetric scattering potential. The resulting band-mixing is necessary to get the asymmetrical effects that the scattering potential introduces.

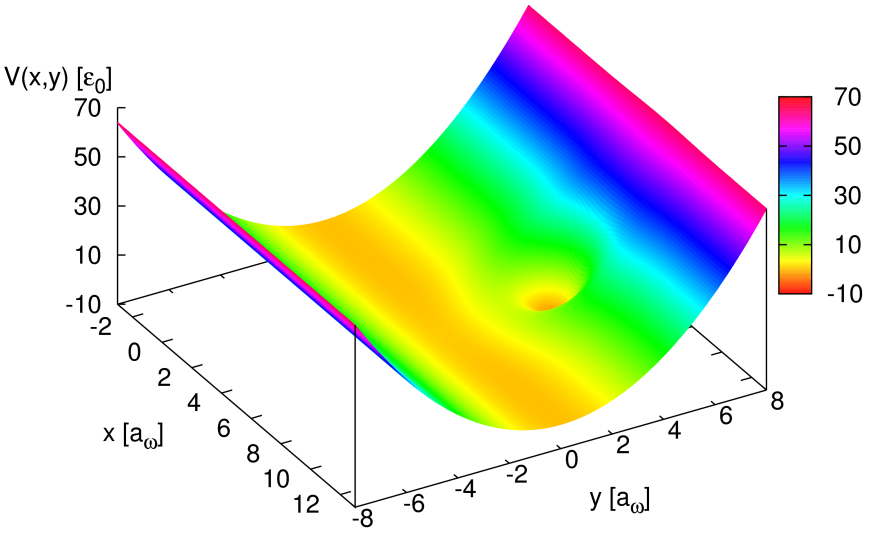

Figure 5.3: The potential distribution for a quantum wire with a single side-coupled quantum dot.

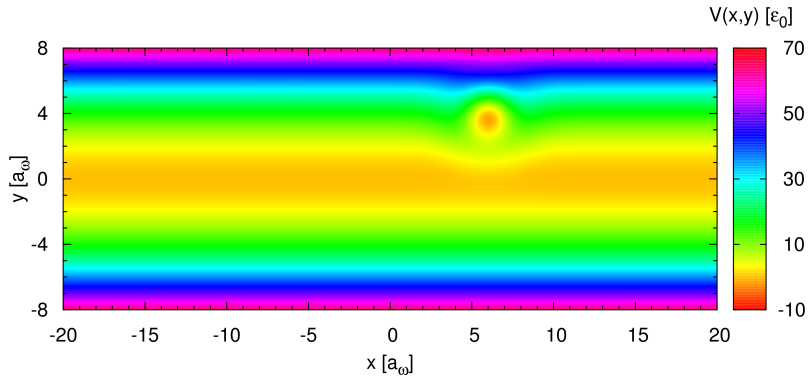

Figure 5.4: The potential distribution for a quantum wire with a single side-coupled quantum dot. This is the same view as for the probability densities.

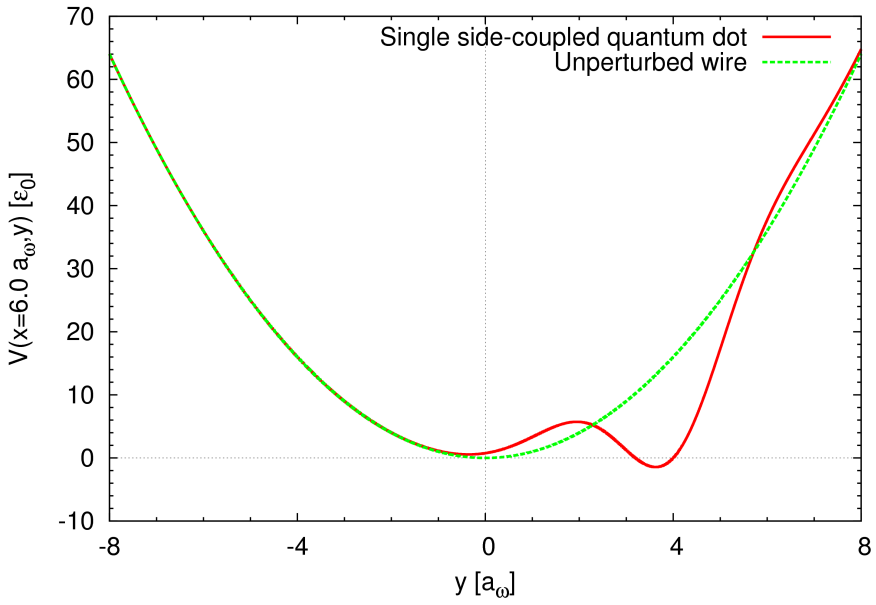

Figure 5.5: The potential distribution for a quantum wire with a single side-coupled quantum dot. The cross section of the potential distribution along the transverse y-direction at the middle of the quantum dot at $x = 6\,a_\omega$.

In figure 5.6 the conductance of the quantum wire is compared to the conductance of an unperturbed quantum wire. The conductance shows a rich structure, as expected. The conductance does not increase immediately at a threshold of a new propagating subband but this is explained by the small constriction introduced by the dot. A very sharp and narrow resonance peak-dip pair is present at $4\,\varepsilon_0$ as shown in more detail in figure 5.7. This is due to a long lived quasi-bound state in the quantum dot. A broader resonance structure is present around 8–10 ε_0. Higher in energy there is a very broad peak at about $12\,\varepsilon_0$. Above $14\,\varepsilon_0$ there are oscillations with a periodic structure and an upward trend.

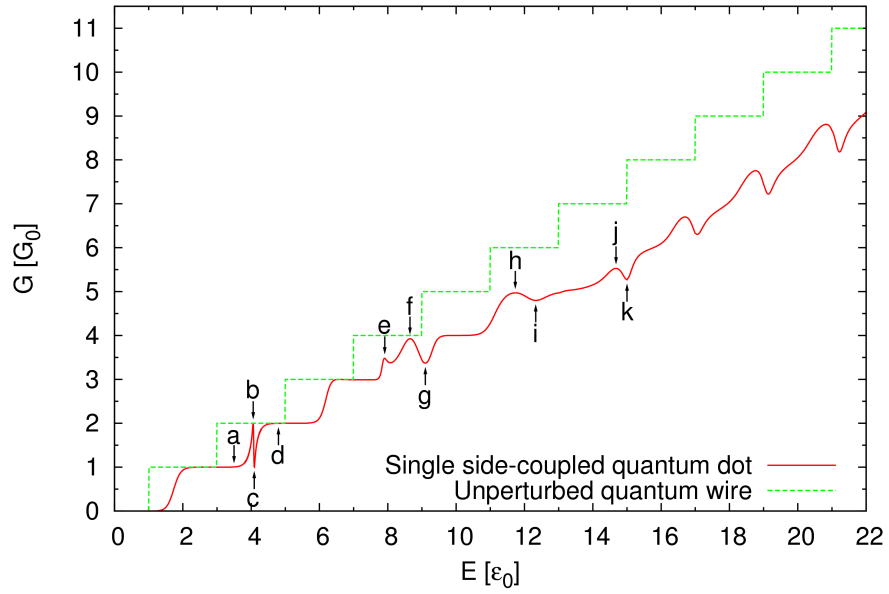

Figure 5.6: The conductance versus energy for a quantum wire with a single side-coupled quantum dot. For comparison the conductance of an unperturbed quantum wire is also shown.

The probability densities of the scattering states which are marked by the arrows in figure 5.6 will now be investigated. Before, it is a good idea to review the setup of the scattering state $\Psi_n(x, y; E)$. There are electrons with energy E and in propagating subband n incident from the left towards the scattering area where they get scattered. The electrons are either reflected into subband m with reflection amplitude $r_{m,n}(E)$ or transmitted into subband m with transmission amplitude $t_{m,n}(E)$.

Figure 5.8 shows the probability densities of scattering states at $E = 3.50\,\varepsilon_0$ which are marked by **a** in figure 5.6. The $n = 0$ scattering state is not too far from the unperturbed incoming state apart from a small wriggle or squirming structure which is due to asymmetrical scattering and band-mixing. There is almost full transmission with a faint beating pattern for $x < 6\,a_\omega$. There is no sign of a structure

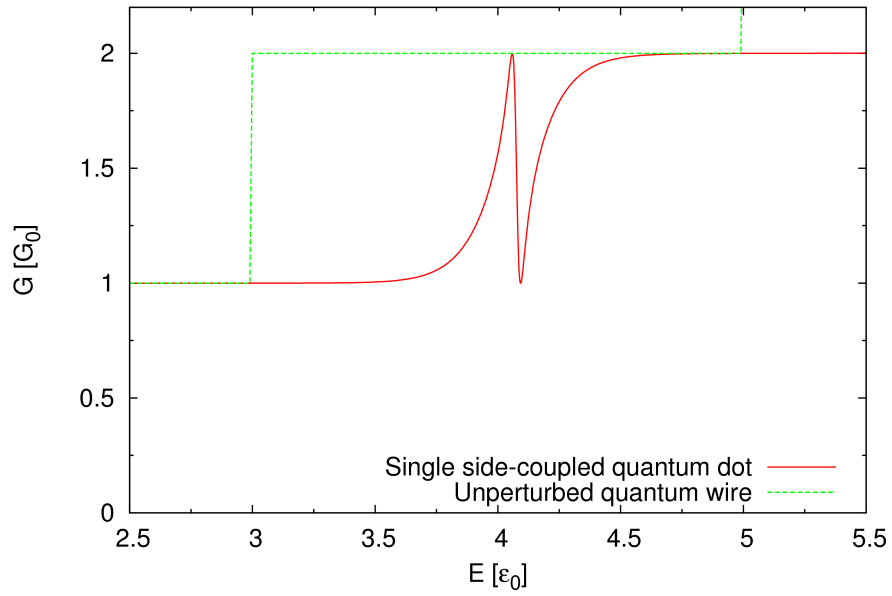

Figure 5.7: The conductance versus energy for a quantum wire with a single side-coupled quantum dot. The resonance peak-dip pair around $4\,\epsilon_0$ is shown in more detail.

around the dot and the only indication of the dot is that the peak of the probability density corresponds to the x-position of the dot at $x = 6\,a_\omega$. The $n = 1$ scattering state shows full reflection around $x = 5\,a_\omega$ which is due to the small constriction introduced by the dot.

The probability densities for the resonance peak at $E = 4.06\,\varepsilon_0$ which is marked by ***b*** in figure 5.6 are shown in figure 5.9. The $n = 0$ scattering state shows not only the extended state in the wire but also a clear quasi-bound state in the dot. The $n = 1$ scattering state shows only a quasi-bound state and no sign of the extended state in the wire. The quasi-bound state in the $n = 1$ scattering state is highly localized and probability density at the dot is high. Thus, the lifetime of the quasi-bound state is very long which is consistent with the narrow resonance peak observed. According to the conductance the $n = 1$ scattering state should have a fully transmitting extended state. Thus, to compress the color scale the square root of the probability densities is shown in figure 5.10. There is the extended state visible and also tunneling between the extended state in the wire and the quasi-bound state in the dot. This tunneling is through the tunneling barrier seen in figure 5.5.

The probability densities for the resonance dip at $E = 4.09\,\varepsilon_0$ which is marked by ***c*** in figure 5.6 are shown in figure 5.11. The scattering states are very similar to the scattering states at the peak. The square root of the probability densities shown in figure 5.12 confirm that the extended state in the $n = 1$ scattering state is fully reflected.

The quasi-bound state at the resonance peak-dip pair corresponds to the lowest eigenstate of the closed quantum dot. The resonance peak-dip pair shows a symmetric Fano line shape as can been seen in figure 5.6. The Fano effect is due to an interference between a localized discrete state and the continuum and was first investigated in atomic system by Fano [37]. Here, the localized state is the quasi-bound state in the side-coupled quantum dot and the continuum is the extended state in the quantum wire. It should be noted that the Fano effect was indeed observed by the group of Kobayashi in an experiment on a quantum wire with a single side-coupled quantum dot [30].

Here, one interesting thing can be noted. The quasi-1D Lippmann-Schwinger scattering formalism is based on plane waves which are extended over the whole wire. It is thus quite remarkable that such highly localized states as seen here can be obtained by sending in extended states.

Figure 5.13 shows the probability densities of scattering states at $E = 4.80\,\varepsilon_0$ which are marked by $\boldsymbol{d}$ in figure 5.6. The fully transmitting extended states in the wire are only visible and there is no indication of a structure around the dot.

Slightly below or above the resonance peak-dip pair there is no indication of a structure around the quantum dot. However, at the resonance peak-dip pair there is a highly localized quasi-bound state in the quantum dot. This shows that the side-coupled quantum dot is not active unless the energy of the electrons corresponds with the energy of the quasi-bound state.

The probability densities of the scattering states for the resonance structure around 8–10 ε_0 which are marked by $\boldsymbol{e}$, $\boldsymbol{f}$, and $\boldsymbol{g}$ in figure 5.6 are shown in figures 5.14, 5.15, and 5.16, respectively. For the $n = 0, 1, 2$ scattering states the extended states in the wire are mainly visible with some structure around the dot for the $n = 1, 2$ scattering states. The $n = 2$ scattering state at $E = 9.10\,\varepsilon_0$ shown in figure 5.16 is particularly interesting. There is some indication of a quasi-bound state in the quantum dot but what is really interesting is the highly pronounced wriggle structure for $x > 6\,a_\omega$. This wriggle structure is due to asymmetrical scattering and band-mixing. This is probably something that could be expected for a case of a classical particle traveling along the x-direction. The $n = 3$ scattering states for all three energies show quasi-bound states in the quantum dot. They seem to be a mixture of the second and third eigenstates of the closed quantum dot. These quasi-bound states are not as strong as for the resonance peak-dip pair. It is thus expected that they have a shorter lifetime which is consistent with that resonances are much broader than for the resonance peak-dip pair lower in energy.

The probability densities of the scattering states for the broad peak and dip around $12\,\varepsilon_0$ which are marked by $\boldsymbol{h}$ and $\boldsymbol{i}$ in figure 5.6 are shown in figures 5.17 and 5.18, respectively. The extended states in the wire are mainly visible with some structure around the quantum dot. There are no highly localized quasi-bound states in the quantum dot but this is expected since the peak and dip are very broad. The $n = 4$ scattering state at $E = 11.73\,\varepsilon_0$ shown in figure 5.17 shows a ring structure in the quantum dot with zero probability in the middle of the dot.

A similar structure can be formed by a linear combination of the fourth and fifth eigenstates of the closed quantum dot. The $n = 5$ scattering state at $E = 12.33\,\varepsilon_0$ shown in figure 5.18 shows an indication of a structure in the quantum dot with three peaks which looks something like the sixth eigenstate of the closed quantum dot. Thus, there are some indications of the eigenstates of the closed quantum dot although they are not very clear. One thing that complicates matters for the higher energies is that there is a significant overlap between the incoming extended state and the quantum dot for higher values of n.

Finally, the probability densities of the scattering states around $15\,\varepsilon_0$ which are marked by $\boldsymbol{j}$ and $\boldsymbol{k}$ in figure 5.6 are shown in figures 5.19 and 5.20, respectively. The scattering states are similar to the scattering states around $12\,\varepsilon_0$. The extended states in the wire are mainly visible with some structure around the quantum dot. This structure shows some indications of the forth, fifth and sixth eigenstates of the closed quantum dot. The scattering states higher in energy are not shown but they have a similar structure as the scattering states around $15\,\varepsilon_0$.

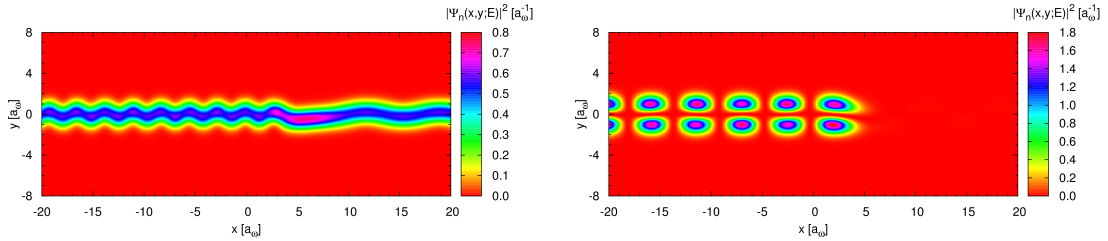

(a) $n = 0$ (b) $n = 1$

Figure 5.8: Quantum wire with a single side-coupled quantum dot. The probability densities of the scattering states at $E = 3.50\,\varepsilon_0$ marked by ***a*** in figure 5.6.

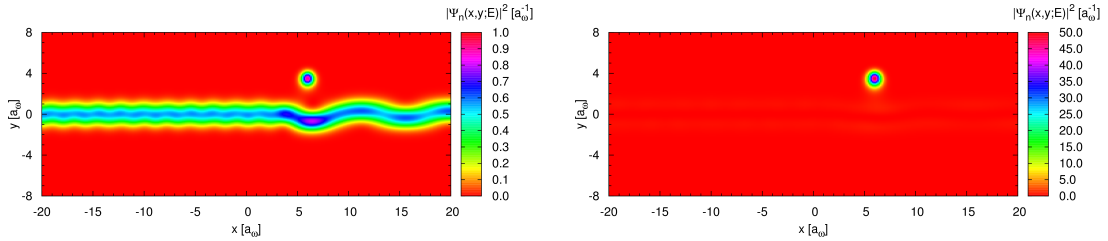

(a) $n = 0$ (b) $n = 1$

Figure 5.9: Quantum wire with a single side-coupled quantum dot. The probability densities of the scattering states at $E = 4.06\,\varepsilon_0$ marked by ***b*** in figure 5.6.

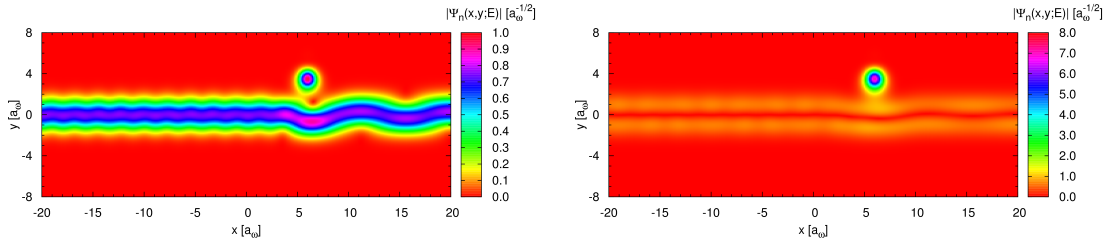

(a) $n = 0$ (b) $n = 1$

Figure 5.10: Quantum wire with a single side-coupled quantum dot. The square root of the probability densities at $E = 4.06\,\varepsilon_0$ marked by ***b*** in figure 5.6. The square root is taken to compress the color scale of the probability densities shown in figure 5.9.

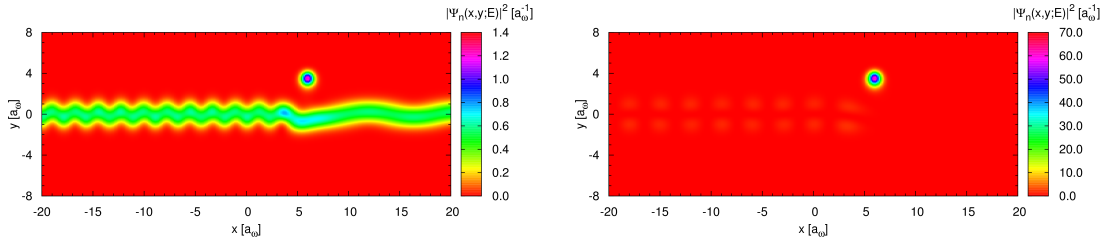

(a) $n = 0$ (b) $n = 1$

Figure 5.11: Quantum wire with a single side-coupled quantum dot. The probability densities of the scattering states at $E = 4.09\,\varepsilon_0$ marked by ***c*** in figure 5.6.

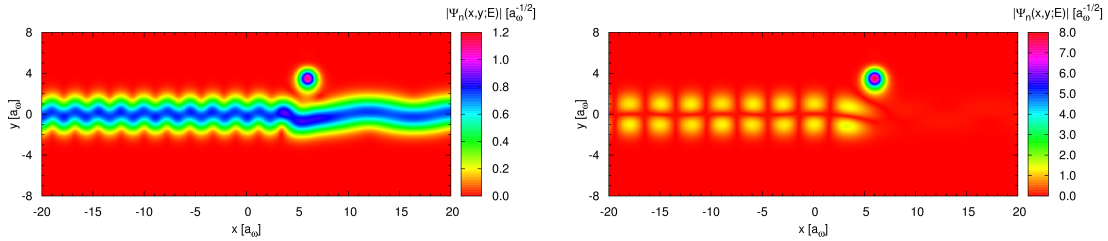

(a) $n = 0$ (b) $n = 1$

Figure 5.12: Quantum wire with a single side-coupled quantum dot. The square root of the probability densities at $E = 4.09\,\varepsilon_0$ marked by ***c*** in figure 5.6. The square root is taken to compress the color scale of the probability densities shown in figure 5.11.

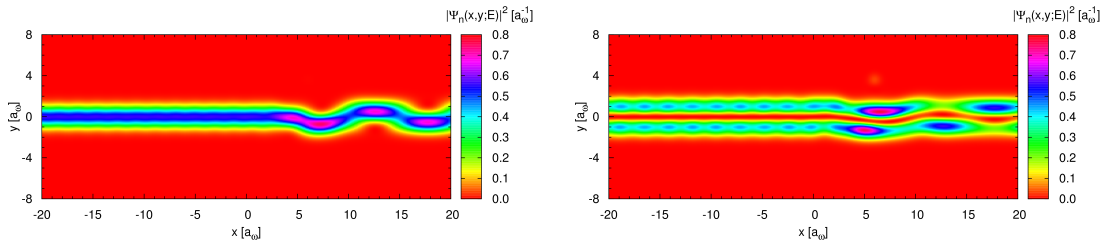

(a) $n = 0$ (b) $n = 1$

Figure 5.13: Quantum wire with a single side-coupled quantum dot. The probability densities of the scattering states at $E = 4.80\,\varepsilon_0$ marked by ***d*** in figure 5.6.

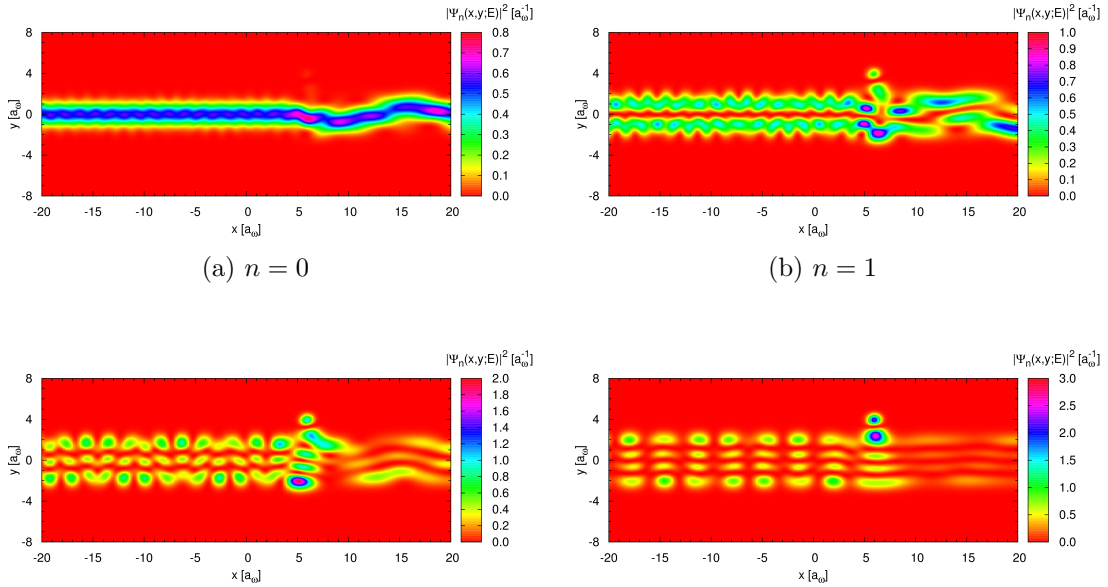

(a) $n = 0$ (b) $n = 1$

(c) $n = 2$ (d) $n = 3$

Figure 5.14: Quantum wire with a single side-coupled quantum dot. The probability densities of the scattering states at $E = 7.91\,\varepsilon_0$ marked by $\boldsymbol{e}$ in figure 5.6.

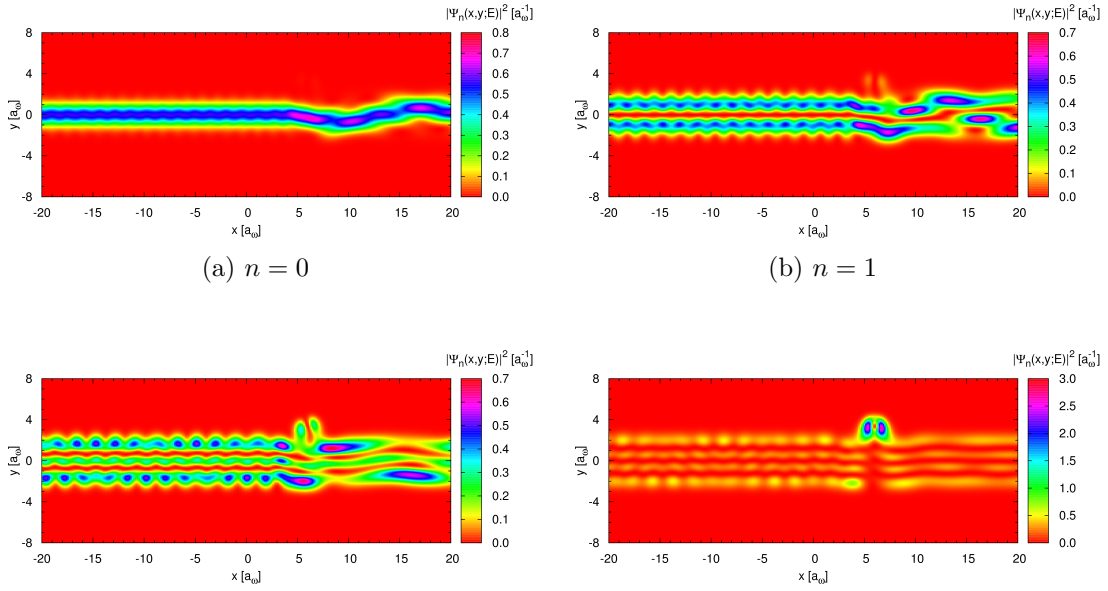

(a) $n = 0$ (b) $n = 1$

(c) $n = 2$ (d) $n = 3$

Figure 5.15: Quantum wire with a single side-coupled quantum dot. The probability densities of the scattering states at $E = 8.65\,\varepsilon_0$ marked by $\boldsymbol{f}$ in figure 5.6.

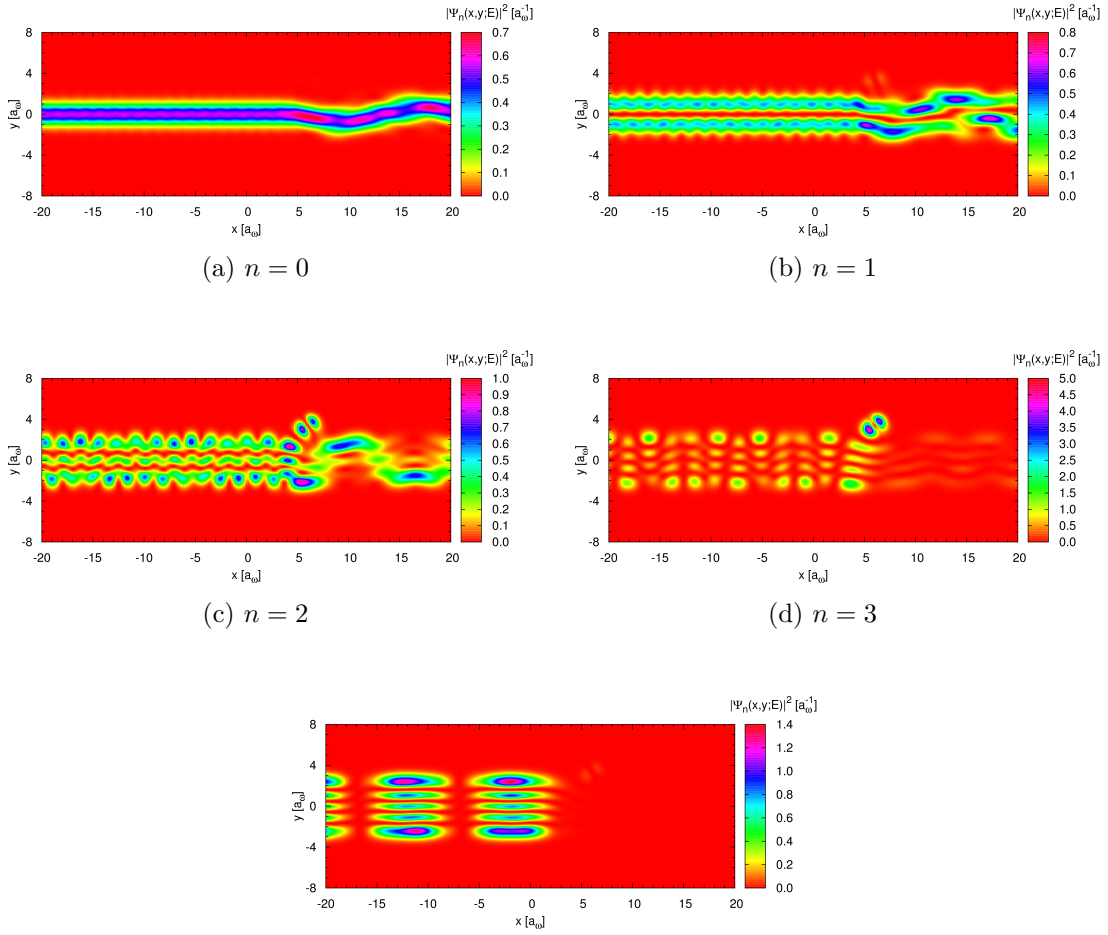

(a) $n = 0$ (b) $n = 1$

(c) $n = 2$ (d) $n = 3$

(e) $n = 4$

Figure 5.16: Quantum wire with a single side-coupled quantum dot. The probability densities of the scattering states at $E = 9.10\,\varepsilon_0$ marked by $\boldsymbol{g}$ in figure 5.6.

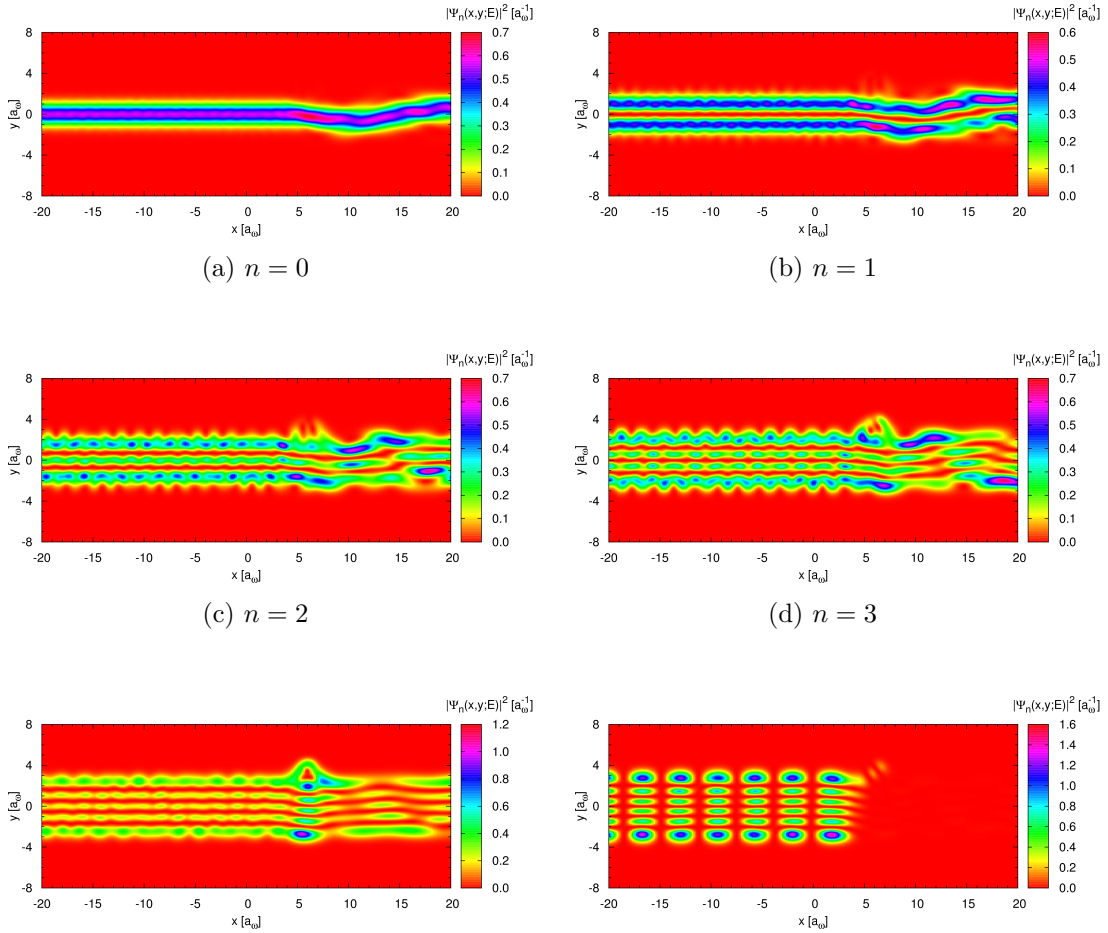

(a) $n = 0$ (b) $n = 1$

(c) $n = 2$ (d) $n = 3$

(e) $n = 4$ (f) $n = 5$

Figure 5.17: Quantum wire with a single side-coupled quantum dot. The probability densities of the scattering states at $E = 11.73\,\varepsilon_0$ marked by ***h*** in figure 5.6.

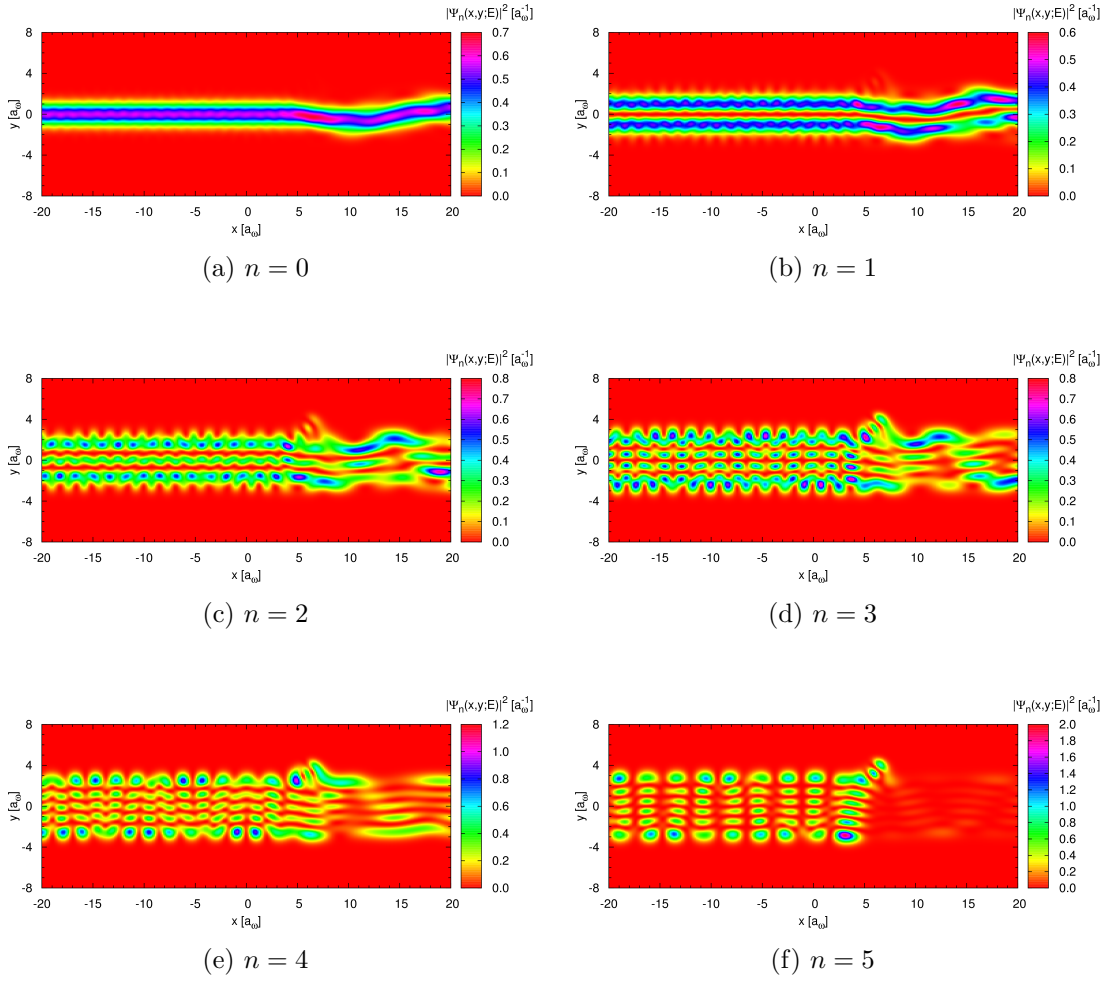

(a) $n = 0$ (b) $n = 1$

(c) $n = 2$ (d) $n = 3$

(e) $n = 4$ (f) $n = 5$

Figure 5.18: Quantum wire with a single side-coupled quantum dot. The probability densities of the scattering states at $E = 12.33\,\varepsilon_0$ marked by ***i*** in figure 5.6.

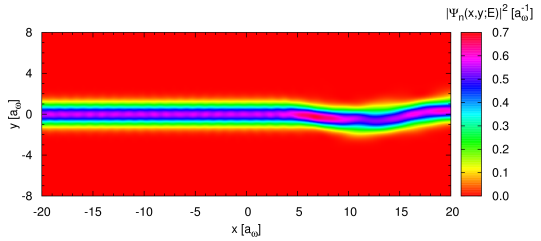

(a) $n = 0$

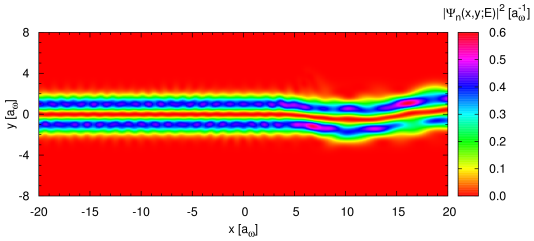

(b) $n = 1$

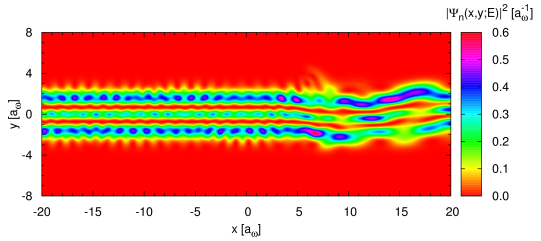

(c) $n = 2$

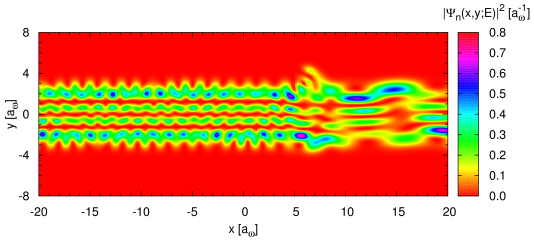

(d) $n = 3$

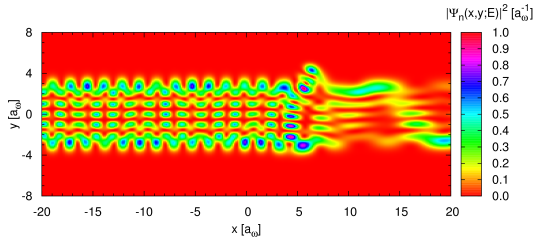

(e) $n = 4$

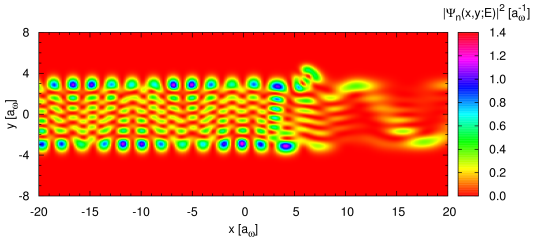

(f) $n = 5$

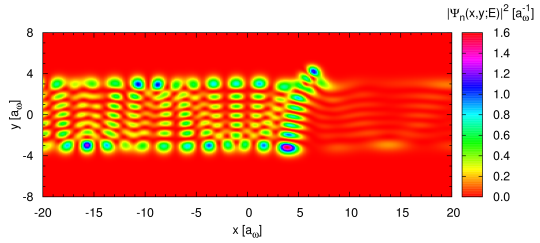

(g) $n = 6$

Figure 5.19: Quantum wire with a single side-coupled quantum dot. The probability densities of the scattering states at $E = 14.68\,\varepsilon_0$ marked by $\boldsymbol{j}$ in figure 5.6.

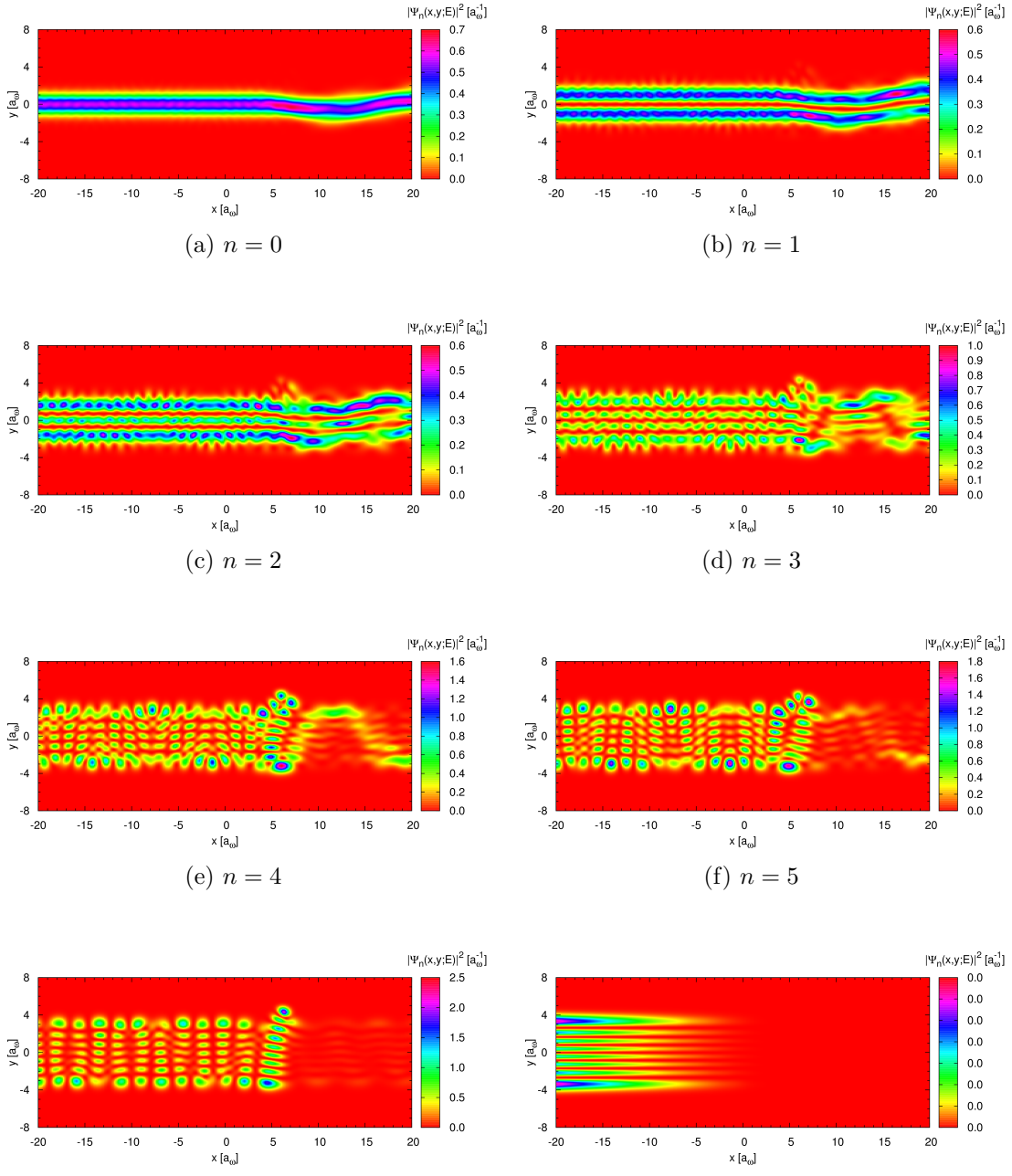

(a) $n = 0$ (b) $n = 1$

(c) $n = 2$ (d) $n = 3$

(e) $n = 4$ (f) $n = 5$

(g) $n = 6$ (h) $n = 7$

Figure 5.20: Quantum wire with a single side-coupled quantum dot. The probability densities of the scattering states at $E = 15.00\,\varepsilon_0$ marked by $\boldsymbol{k}$ in figure 5.6.

5.2 Single Quantum Dot and a Step

The transport through a quantum wire with a single side-coupled quantum dot and a step is now investigated. The step has a height of $V_s = 1.0\,\varepsilon_0$ but the scattering potential and the parameters for the quantum dot are the same as before. Figures 5.21 and 5.22 show the potential distribution of the quantum wire system. Figure 5.23 shows the cross section of the potential distribution along the x-direction for various values of y. The cross section shows that the step and the quantum dot define an effective well in the quantum wire between the step and the quantum dot. The effective x-length of the well is not well defined but can be approximated to be about 4–5 a_ω.

The step changes the conduction properties. The thresholds where a new subband becomes propagating are moved and there is not always the same number of propagating subbands for the whole wire. The thresholds are now at $2, 4, 6, 8, \ldots\ \varepsilon_0$ but were at $1, 3, 5, 7, \ldots\ \varepsilon_0$ without a step. The number of subbands propagating right of the step is $N_{P;R}(E) = N_{P;L}(E) + 1$ on the energy intervals 3–4, 5–6, 7–8, $\ldots\ \varepsilon_0$.

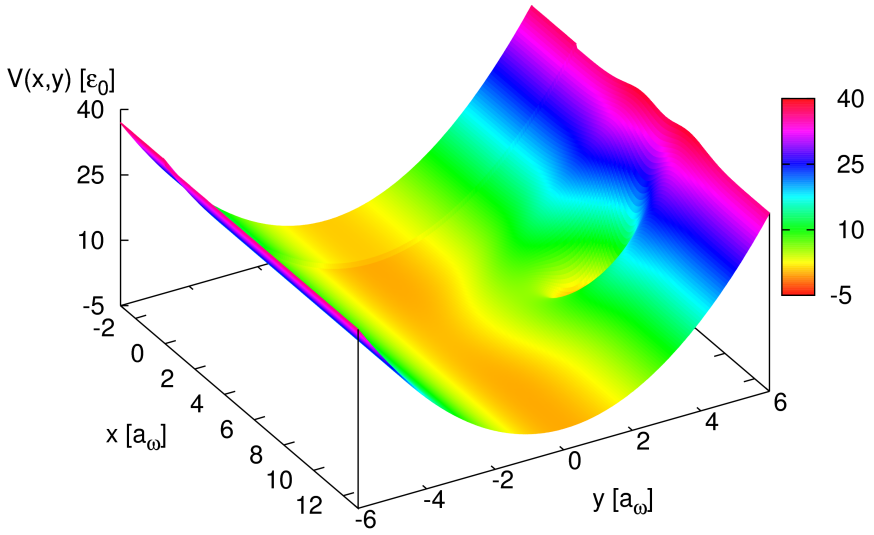

Figure 5.21: The potential distribution for a quantum wire with a single side-coupled quantum dot and a step.

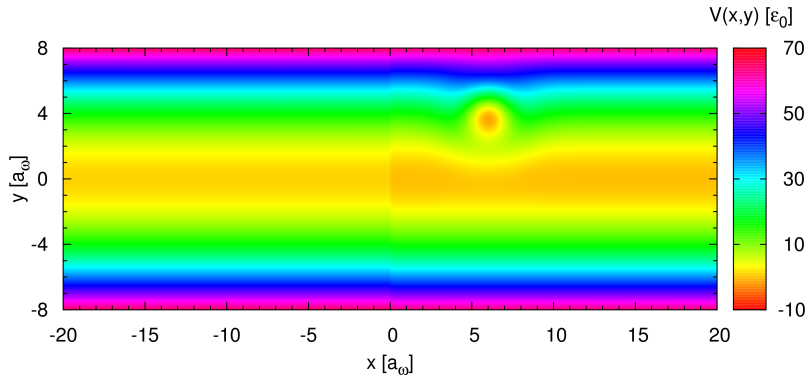

Figure 5.22: The potential distribution for a quantum wire with a single side-coupled quantum dot and a step. This is the same view as for the probability densities below.

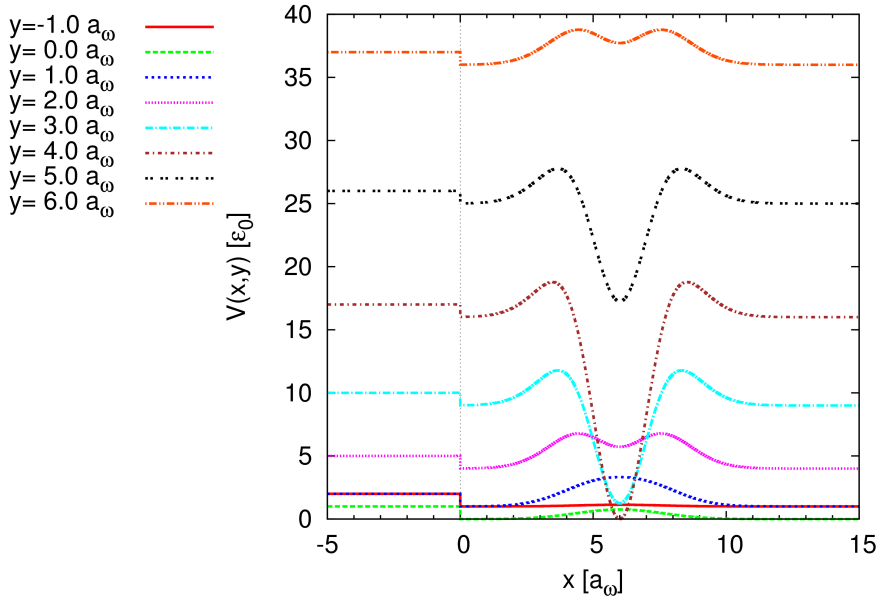

Figure 5.23: The potential distribution for a quantum wire with a single side-coupled quantum dot. The cross section of the potential distribution along the x-direction for various values of y.

Figure 5.24 shows the conductance of the quantum wire and figure 5.25 shows a comparison of the conductance with and without a step. The conductance with a step is very similar to the conductance without a step apart from some fine structure that the step introduces. This fine structure is regularly spaced and in the form of narrow dips below $12\,\varepsilon_0$ but changes above $12\,\varepsilon_0$ where it becomes less pronounced. The conductance structure is otherwise nearly the same as without a step. There is a sharp resonance peak-dip pair around $4\,\varepsilon_0$. Around 8–$10\,\varepsilon_0$ there is a broader resonance structure. Above $14\,\varepsilon_0$ there are oscillations with a periodic structure and an upward trend.

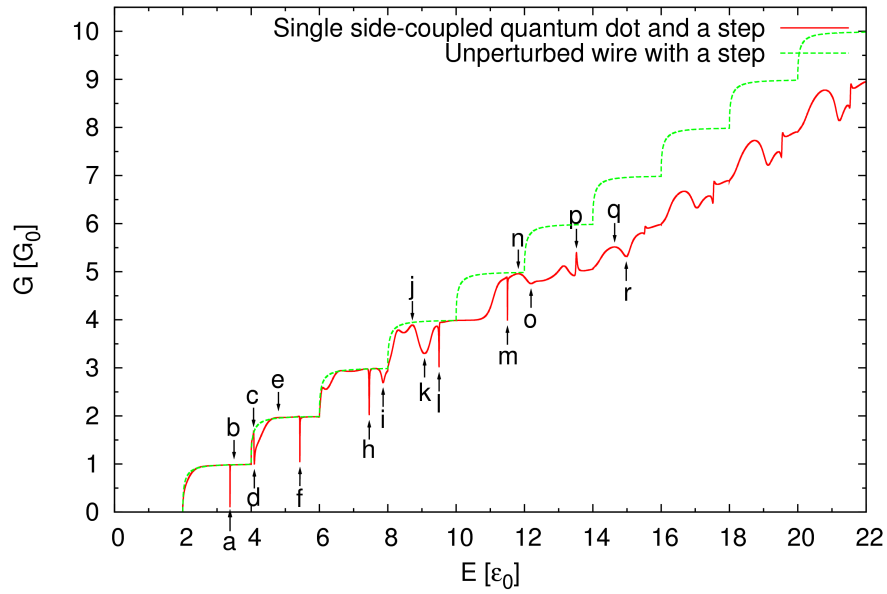

Figure 5.24: The conductance versus energy for a quantum wire with a single side-coupled quantum dot and a step. For comparison the conductance of an unperturbed quantum wire with a step is also shown.

The probability densities of the scattering states which are marked by the arrows in figure 5.24 will now be investigated.

The scattering states where there are corresponding scattering states from the case without a step will not be discussed in detail but they are shown here for comparison. These are the scattering states marked by ***b***–***e***, ***i***–***k***, ***n***–***o***, and ***q***–***r*** in figure 5.24 and shown in the figures 5.29–5.34, 5.37–5.39, 5.42–5.43, and 5.45–5.46, respectively. The scattering states for these two cases are very similar. The main difference is that due to the step the wavenumbers are different left and right of the step. This shows up as different beating patterns left and right of the step as seen when figures 5.12 and 5.33 are compared. These scattering states will not be discussed any further.

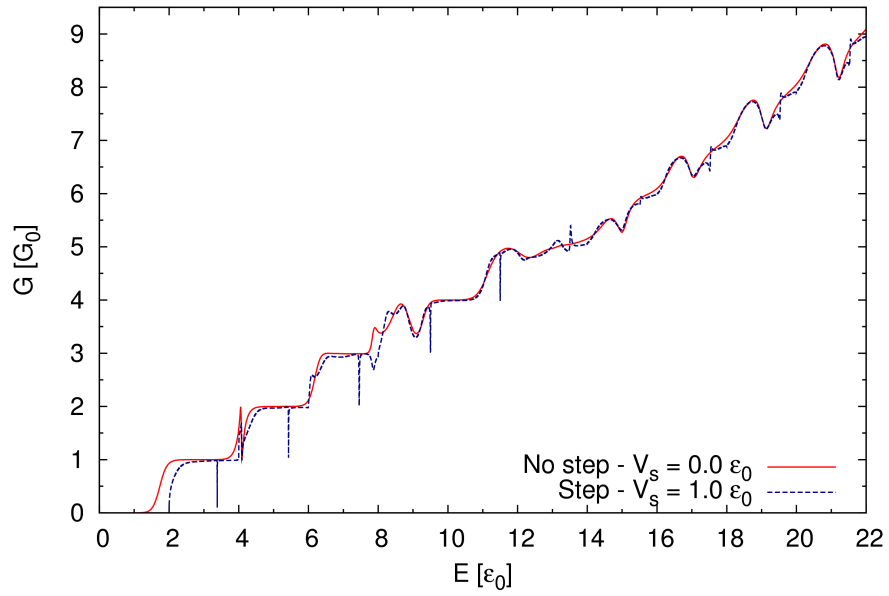

Figure 5.25: A comparison of the conductance versus energy for a quantum wire with a single side-coupled quantum dot with and without a step.

The probability density for the narrow resonance dip at $E = 3.383\,\varepsilon_0$ which is marked by ***a*** in figure 5.24 is shown in figure 5.27. There is no indication of the extended state in the wire. Only visible is a quasi-bound state which seems to be in the effective well defined by the step and the quantum dot. This quasi-bound state is in the $n = 1$ subband whereas $n = 0$ is the incoming subband. It should be noted that the $n = 1$ subband is only propagating right of the step. The wavelength of $n = 1$ subband at this energy is $\lambda_{R;2} \approx 10.2\,a_\omega$. Thus, the half-wavelength $\lambda_{R;2}/2$ approximately fits with the effective x-length of the well. The single peak in the x-direction confirms this. The conductance at this energy is about $0.1\,G_0$ so there should be a small transmitting extended state right of the quantum dot. However, it is not visible on the color scale used. Thus, to compress the color scale the fourth root of the probability density is shown in figure 5.28. The transmitting extended state is visible there but it is in the $n = 1$ subband.

The probability densities for the dips higher in energy at $5.428\,\varepsilon_0$, $7.456\,\varepsilon_0$, $9.5\,\varepsilon_0$, and $11.502\,\varepsilon_0$ which are marked by ***f***, ***h***, ***l***, and ***m*** in figure 5.24 are shown in figures 5.35, 5.36, 5.40, and 5.41, respectively. All these dips show the same effect as the first dip. There is a quasi-bound state in the effective well defined by the step and the quantum dot. The quasi-bound state is always in the subband which is one higher than the highest incoming subband. The wavelengths of the corresponding subbands are about 8.7–$10.2\,a_\omega$ so the half-wavelength seem to fit with the effective x-length of the well. This is confirmed by that there is always a single peak in the x-direction.

The probability densities for the peak at $E = 13.521\,\varepsilon_0$ which is marked by $\boldsymbol{p}$ in figure 5.24 are shown in figure 5.44. The same effect as for the dips before is visible. Also, there is a very faint remnants of a structure in the quantum dot. This structure looks like the fifth eigenstate of the closed quantum dot.

All the conductance fine structure the step introduces is due to the effective well defined by the step and the quantum dot. This well acts as a resonator resulting in resonance dips and peaks. This happens when the corresponding half-wavelengths in the x-direction fit with the effective x-length of the well. This is confirmed by moving the quantum dot in the x-direction as shown in figure 5.26. This changes the effective x-length of the well. The dip moves lower in energy if the effective x-length of the well is increased because a larger half-wavelength is needed to fulfill the resonance condition. The opposite happens when the effective x-length of the well is decreased.

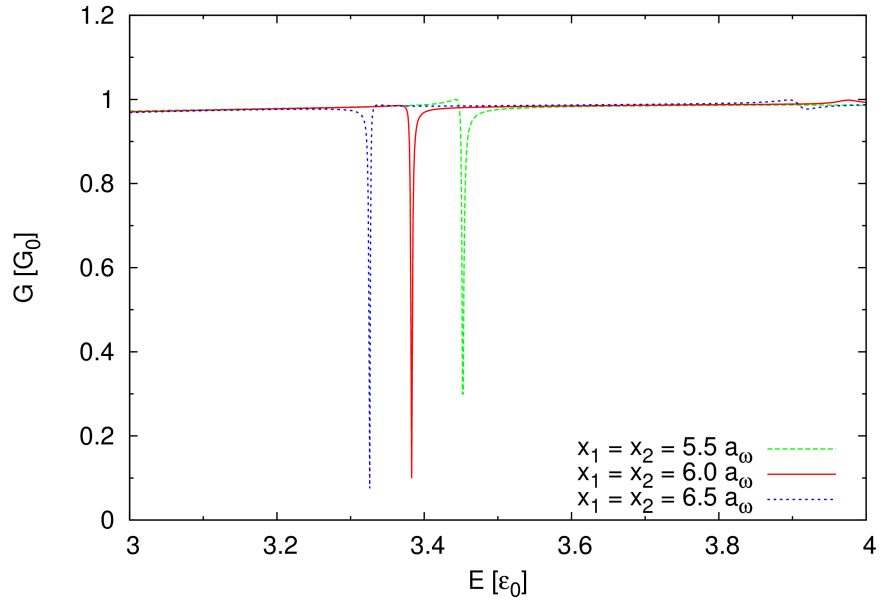

Figure 5.26: The conductance versus energy for a quantum wire with a single side-coupled quantum dot and a step. The dip around $3.4\,\varepsilon_0$ which is due to the effective well defined by the step and the quantum dot. The effective x-length of the well is changed by moving the dot. This alters the energy position of the dip since the half-wavelength required to fulfill the resonance condition is changed.

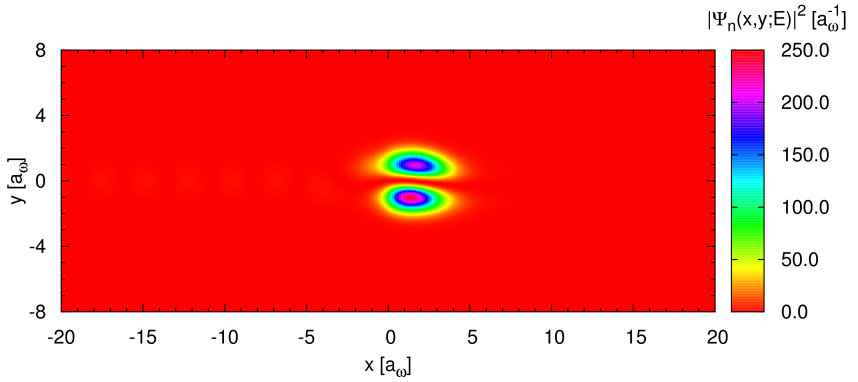

(a) $n = 0$

Figure 5.27: Quantum wire with a single side-coupled quantum dot and a step. The probability density of the scattering state at $E = 3.383\,\varepsilon_0$ marked by ***a*** in figure 5.24.

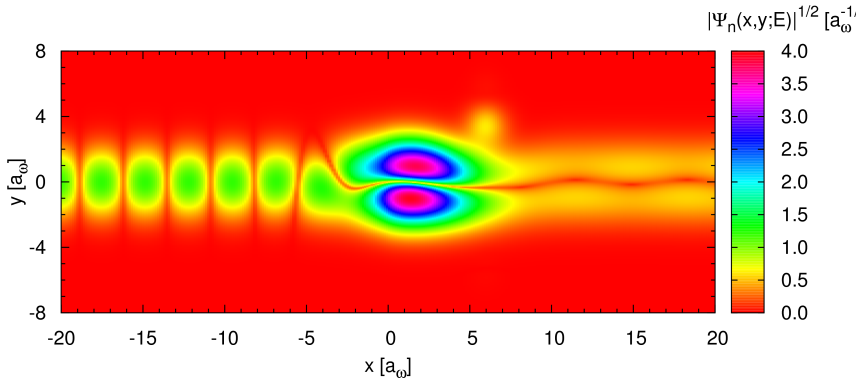

(a) $n = 0$

Figure 5.28: Quantum wire with a single side-coupled quantum dot and a step. The fourth root of the probability density at $E = 3.383\,\varepsilon_0$ marked by ***a*** in figure 5.24. The fourth root is taken to compress the color scale of the probability density shown in figure 5.27.

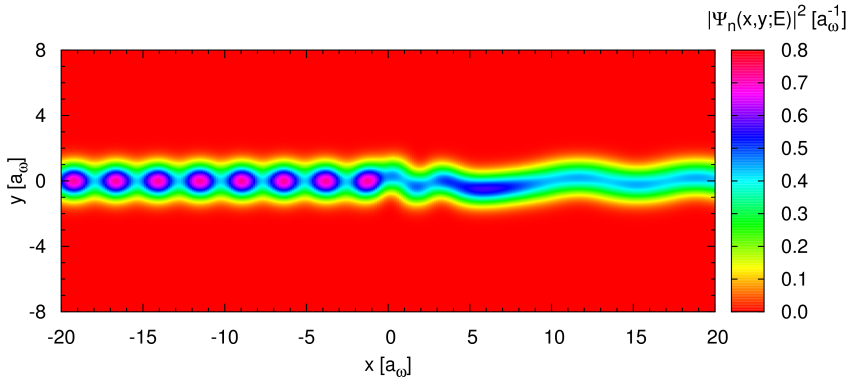

(a) $n = 0$

Figure 5.29: Quantum wire with a single side-coupled quantum dot and a step. The probability density of the scattering states at $E = 3.5\,\varepsilon_0$ marked by ***b*** in figure 5.24.

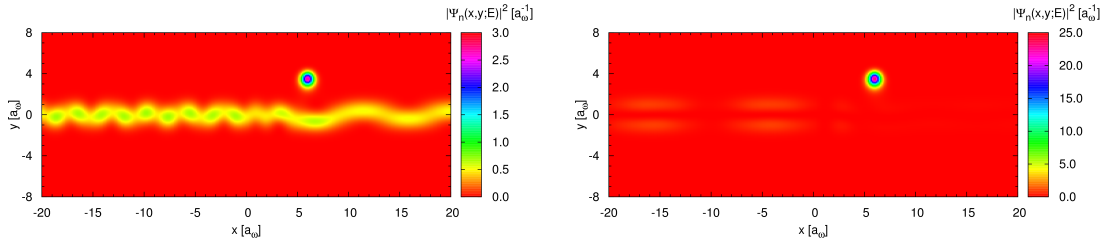

(a) $n = 0$ (b) $n = 1$

Figure 5.30: Quantum wire with a single side-coupled quantum dot and a step. The probability densities of the scattering states at $E = 4.073\,\varepsilon_0$ marked by ***c*** in figure 5.24.

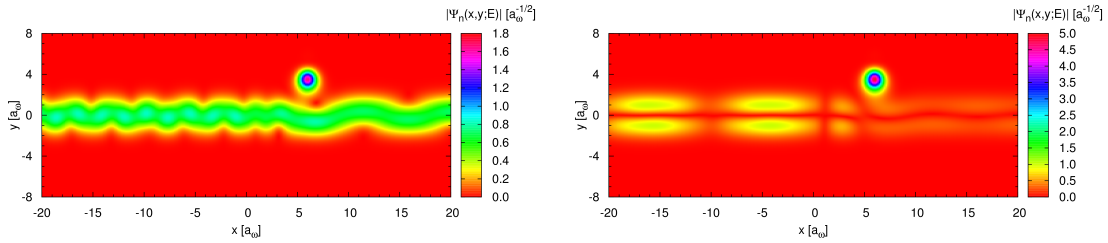

(a) $n = 0$ (b) $n = 1$

Figure 5.31: Quantum wire with a single side-coupled quantum dot and a step. The square root of the probability densities at $E = 4.073\,\varepsilon_0$ marked by ***c*** in figure 5.24. The square root is taken to compress the color scale of the probability densities shown in figure 5.30.

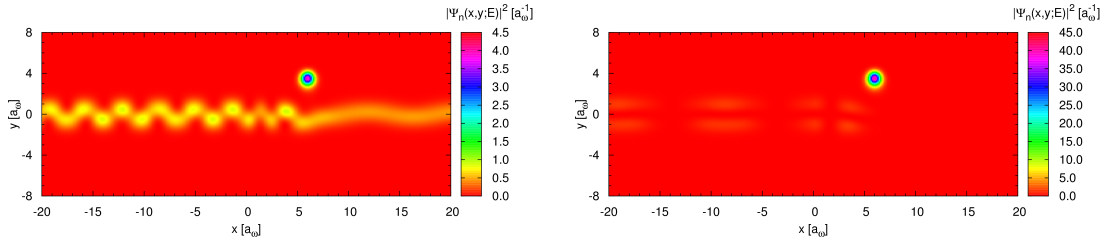

(a) $n = 0$ (b) $n = 1$

Figure 5.32: Quantum wire with a single side-coupled quantum dot and a step. The probability densities of the scattering states at $E = 4.093\,\varepsilon_0$ marked by ***d*** in figure 5.24.

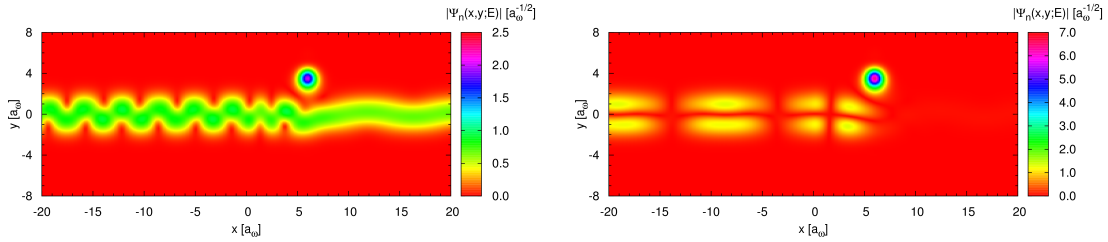

(a) $n = 0$ (b) $n = 1$

Figure 5.33: Quantum wire with a single side-coupled quantum dot and a step. The square root of the probability densities at $E = 4.093\,\varepsilon_0$ marked by ***d*** in figure 5.24. The square root is taken to compress the color scale of the probability densities shown in figure 5.32.

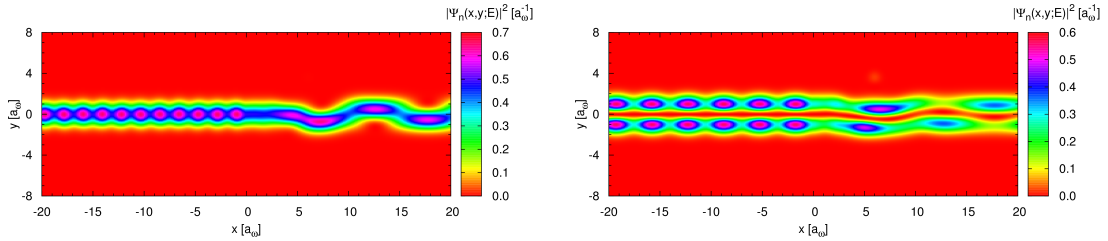

(a) $n = 0$ (b) $n = 1$

Figure 5.34: Quantum wire with a single side-coupled quantum dot and a step. The probability densities of the scattering states at $E = 4.8\,\varepsilon_0$ marked by ***e*** in figure 5.24.

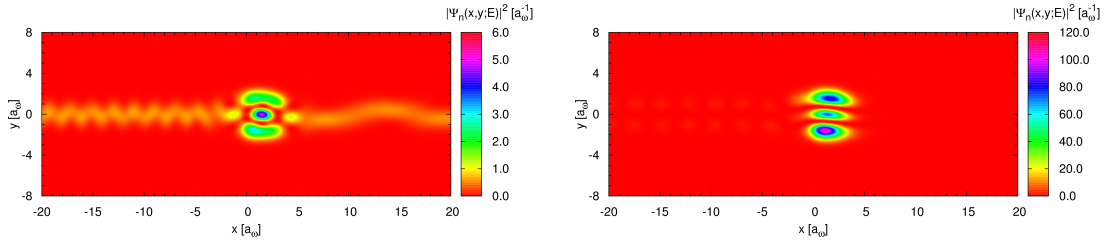

(a) $n = 0$ (b) $n = 1$

Figure 5.35: Quantum wire with a single side-coupled quantum dot and a step. The probability densities of the scattering states at $E = 5.428\,\varepsilon_0$ marked by $\boldsymbol{f}$ in figure 5.24.

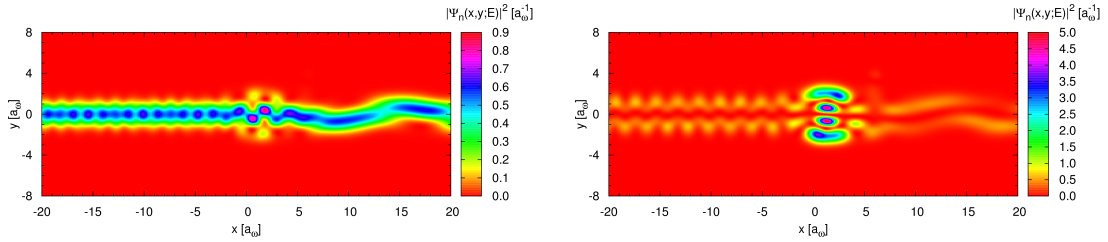

(a) $n = 0$ (b) $n = 1$

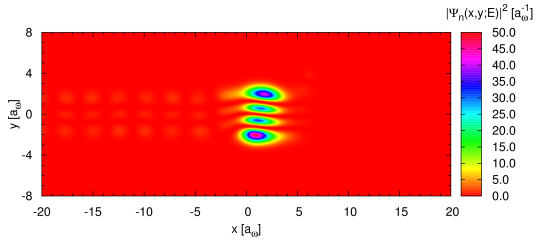

(c) $n = 2$

Figure 5.36: Quantum wire with a single side-coupled quantum dot and a step. The probability densities of the scattering states at $E = 7.456\,\varepsilon_0$ marked by $\boldsymbol{h}$ in figure 5.24.

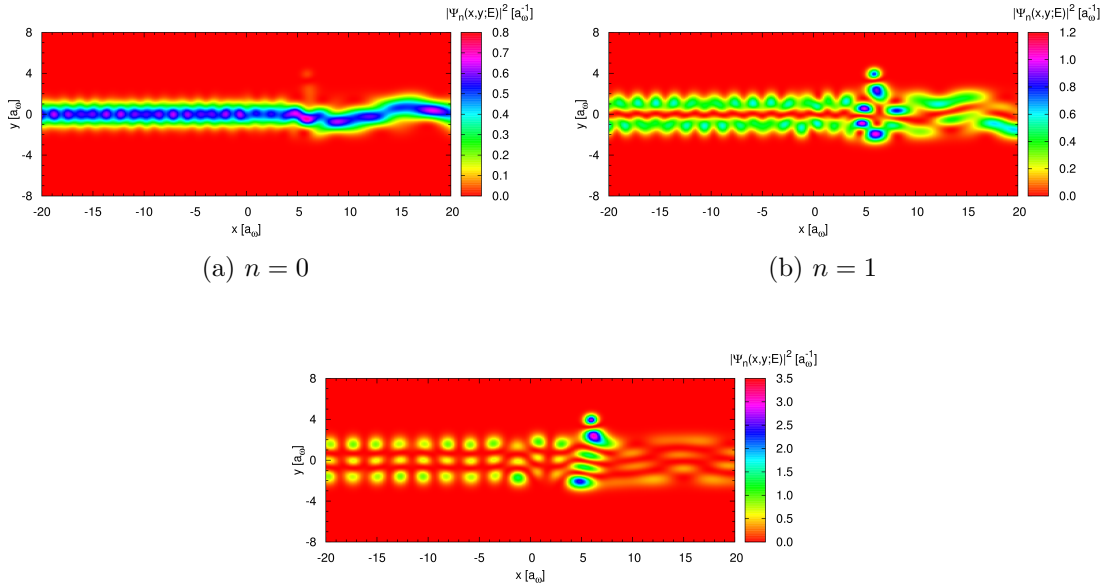

(a) $n = 0$ (b) $n = 1$

(c) $n = 2$

Figure 5.37: Quantum wire with a single side-coupled quantum dot and a step. The probability densities of the scattering states at $E = 7.863\,\varepsilon_0$ marked by ***i*** in figure 5.24.

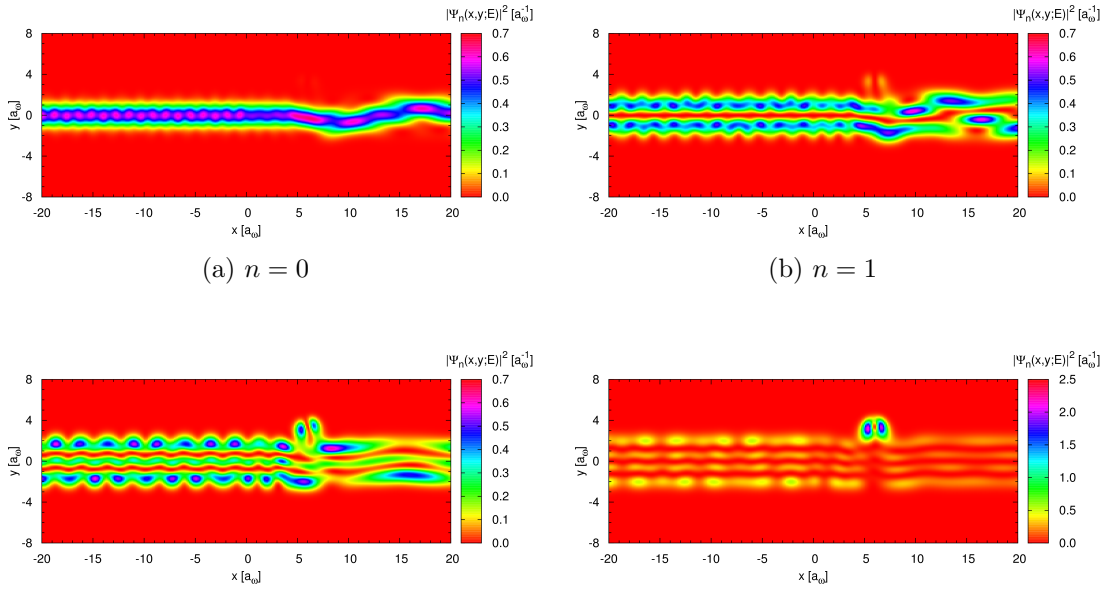

(a) $n = 0$ (b) $n = 1$

(c) $n = 2$ (d) $n = 3$

Figure 5.38: Quantum wire with a single side-coupled quantum dot and a step. The probability densities of the scattering states at $E = 8.720\,\varepsilon_0$ marked by ***j*** in figure 5.24.

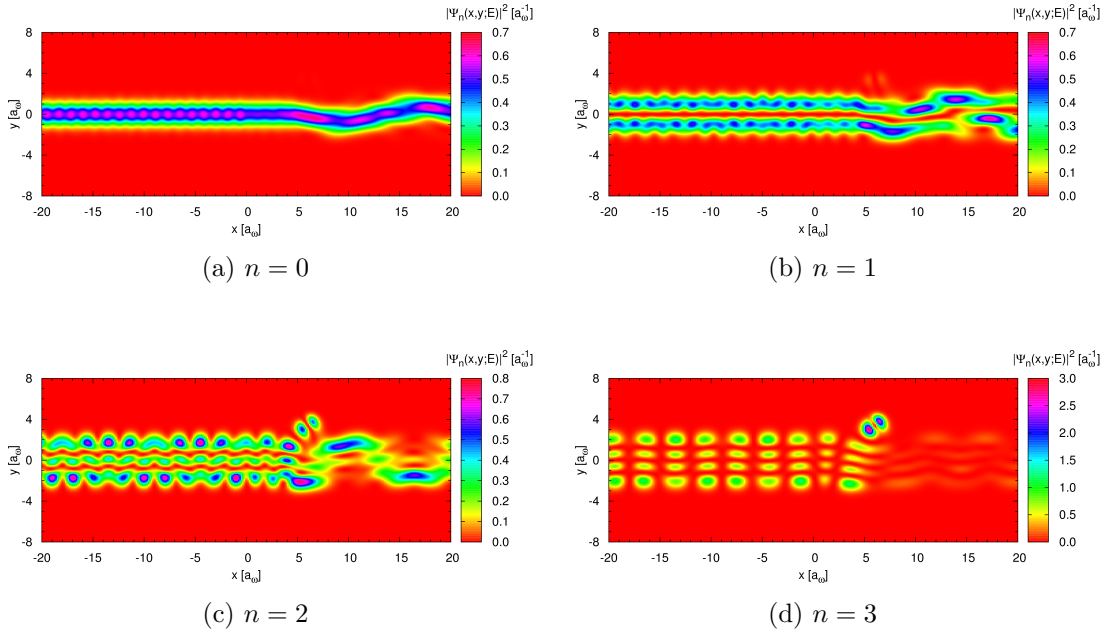

(a) $n = 0$ (b) $n = 1$

(c) $n = 2$ (d) $n = 3$

Figure 5.39: Quantum wire with a single side-coupled quantum dot and a step. The probability densities of the scattering states at $E = 9.076\,\varepsilon_0$ marked by $\boldsymbol{k}$ in figure 5.24.

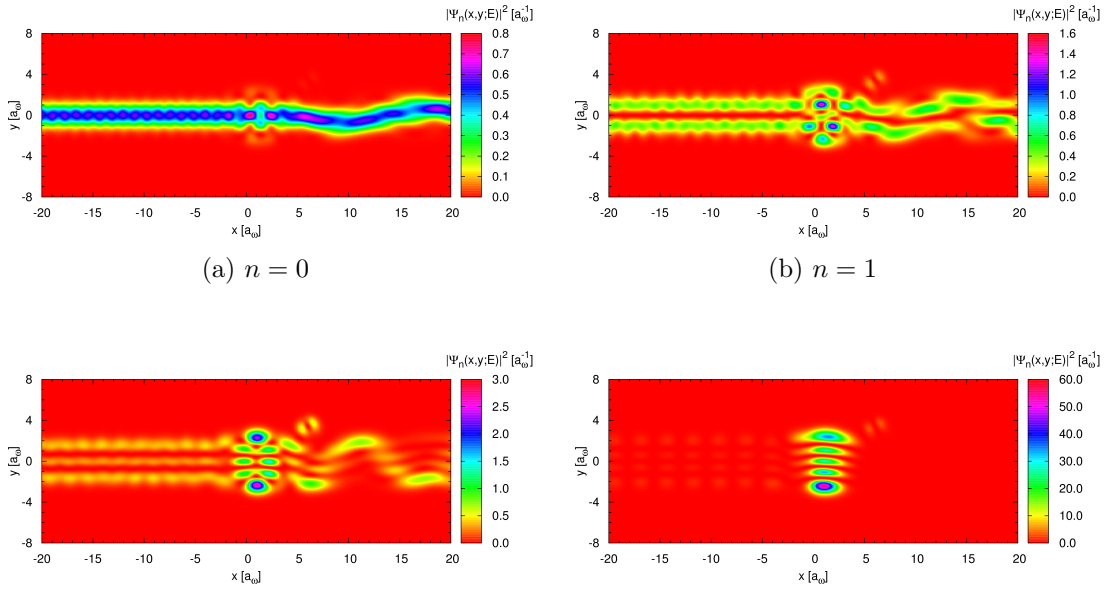

(a) $n = 0$ (b) $n = 1$

(c) $n = 2$ (d) $n = 3$

Figure 5.40: Quantum wire with a single side-coupled quantum dot and a step. The probability densities of the scattering states at $E = 9.5\,\varepsilon_0$ marked by $\boldsymbol{l}$ in figure 5.24.

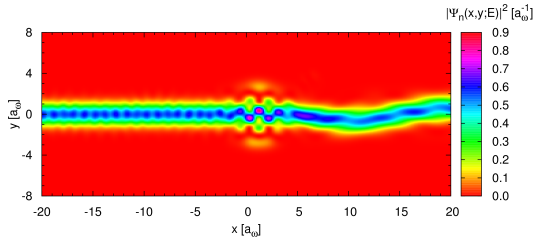

(a) $n = 0$

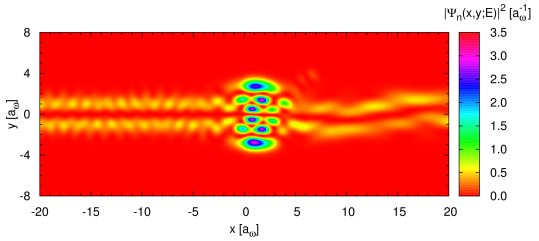

(b) $n = 1$

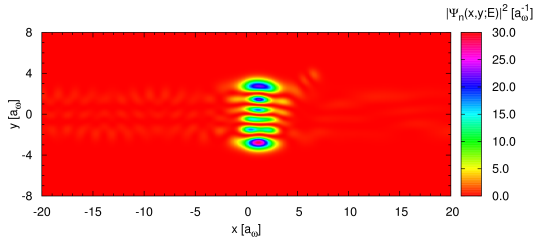

(c) $n = 2$

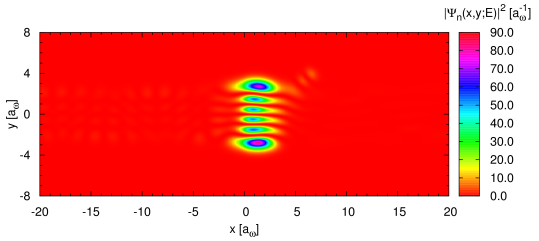

(d) $n = 3$

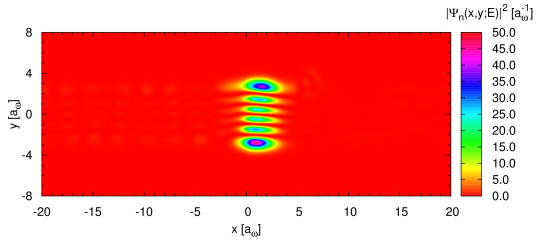

(e) $n = 4$

Figure 5.41: Quantum wire with a single side-coupled quantum dot and a step. The probability densities of the scattering states at $E = 11.502\,\varepsilon_0$ marked by $\boldsymbol{m}$ in figure 5.24.

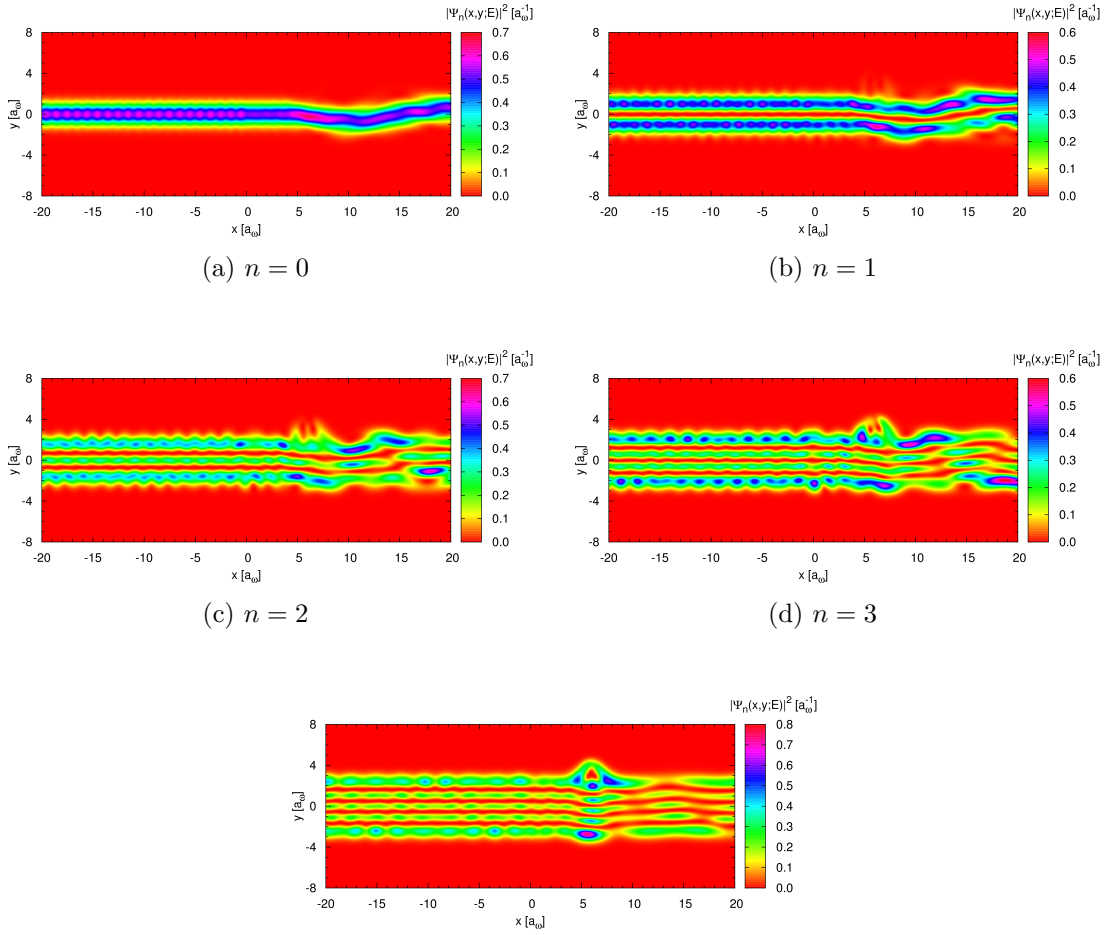

(a) $n = 0$ (b) $n = 1$

(c) $n = 2$ (d) $n = 3$

(e) $n = 4$

Figure 5.42: Quantum wire with a single side-coupled quantum dot and a step. The probability densities of the scattering states at $E = 11.818\,\varepsilon_0$ marked by $\boldsymbol{n}$ in figure 5.24.

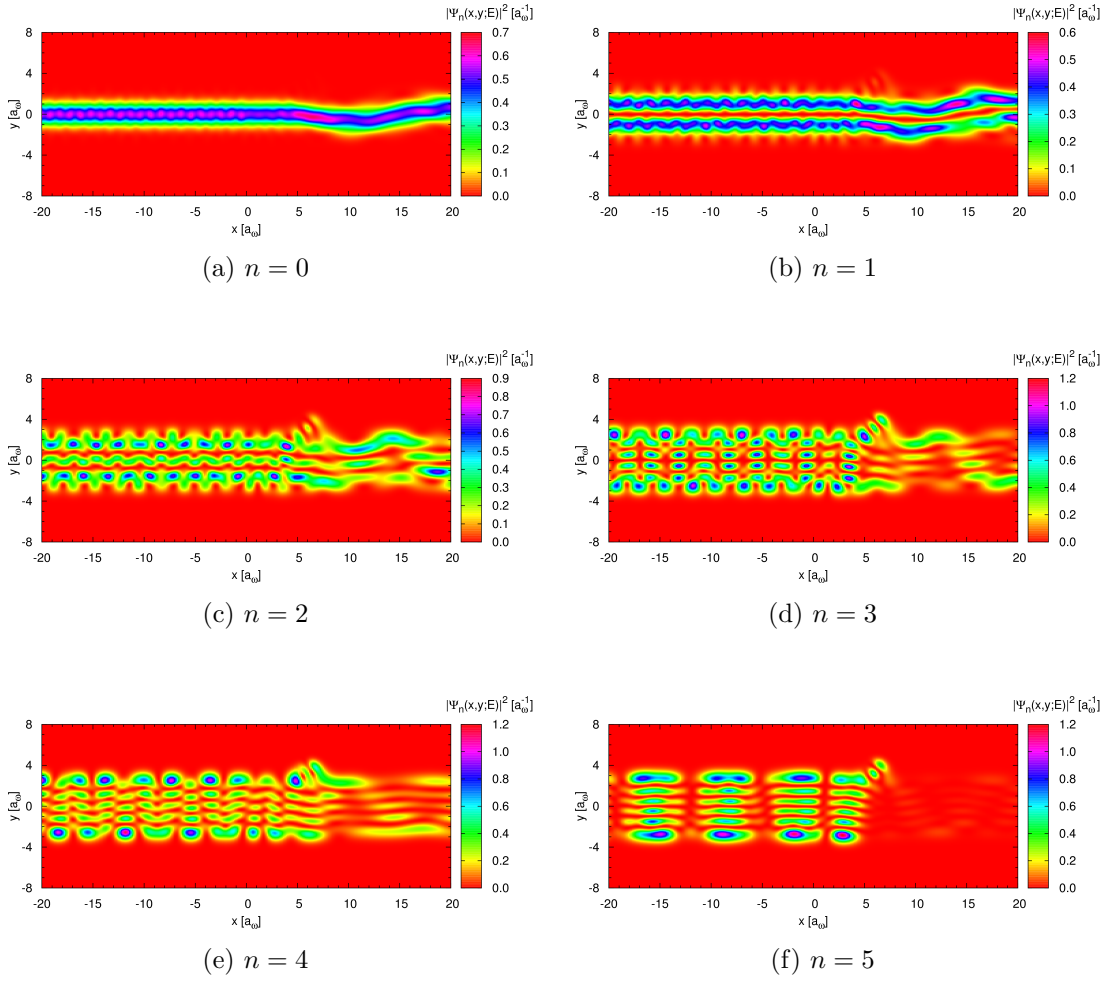

(a) $n = 0$ (b) $n = 1$

(c) $n = 2$ (d) $n = 3$

(e) $n = 4$ (f) $n = 5$

Figure 5.43: Quantum wire with a single side-coupled quantum dot and a step. The probability densities of the scattering states at $E = 12.194\,\varepsilon_0$ marked by ***o*** in figure 5.24.

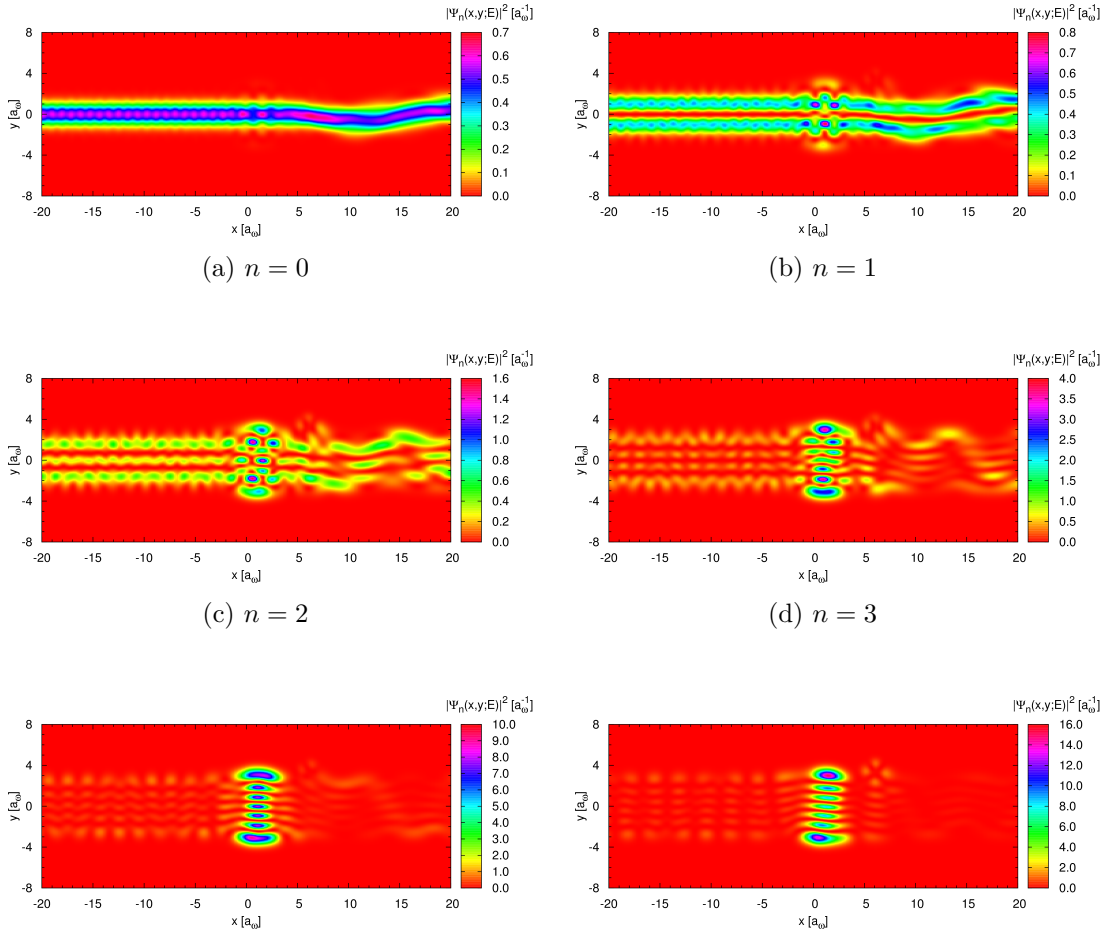

(a) $n = 0$ (b) $n = 1$

(c) $n = 2$ (d) $n = 3$

(e) $n = 4$ (f) $n = 5$

Figure 5.44: Quantum wire with a single side-coupled quantum dot and a step. The probability densities of the scattering states at $E = 13.521\,\varepsilon_0$ marked by $\boldsymbol{p}$ in figure 5.24.

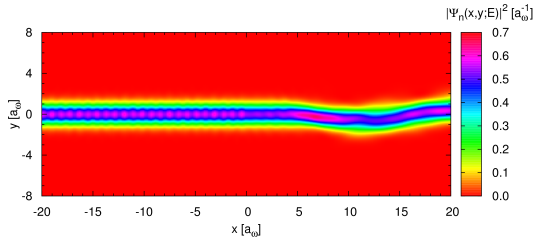

(a) $n = 0$

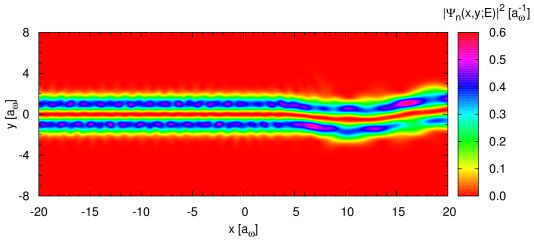

(b) $n = 1$

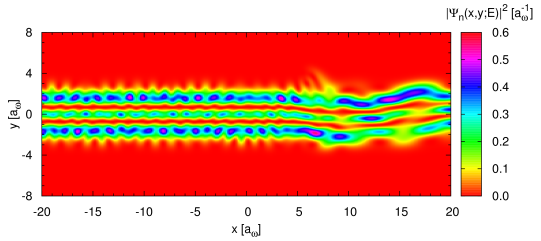

(c) $n = 2$

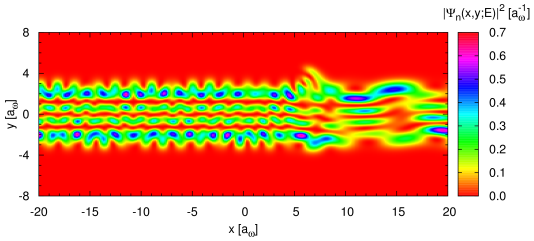

(d) $n = 3$

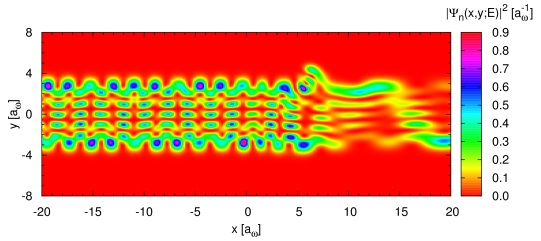

(e) $n = 4$

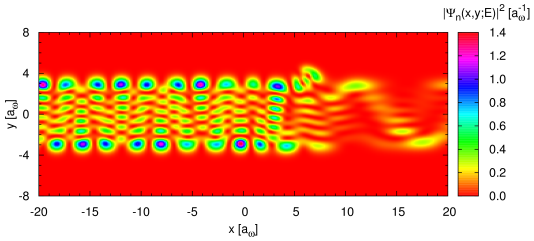

(f) $n = 5$

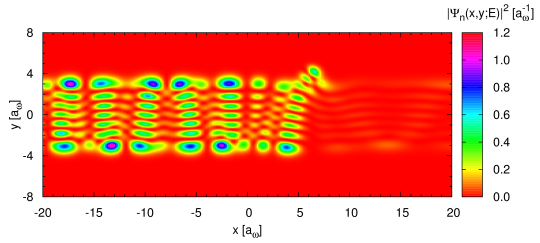

(g) $n = 6$

Figure 5.45: Quantum wire with a single side-coupled quantum dot and a step. The probability densities of the scattering states at $E = 14.638\,\varepsilon_0$ marked by $\boldsymbol{q}$ in figure 5.24.

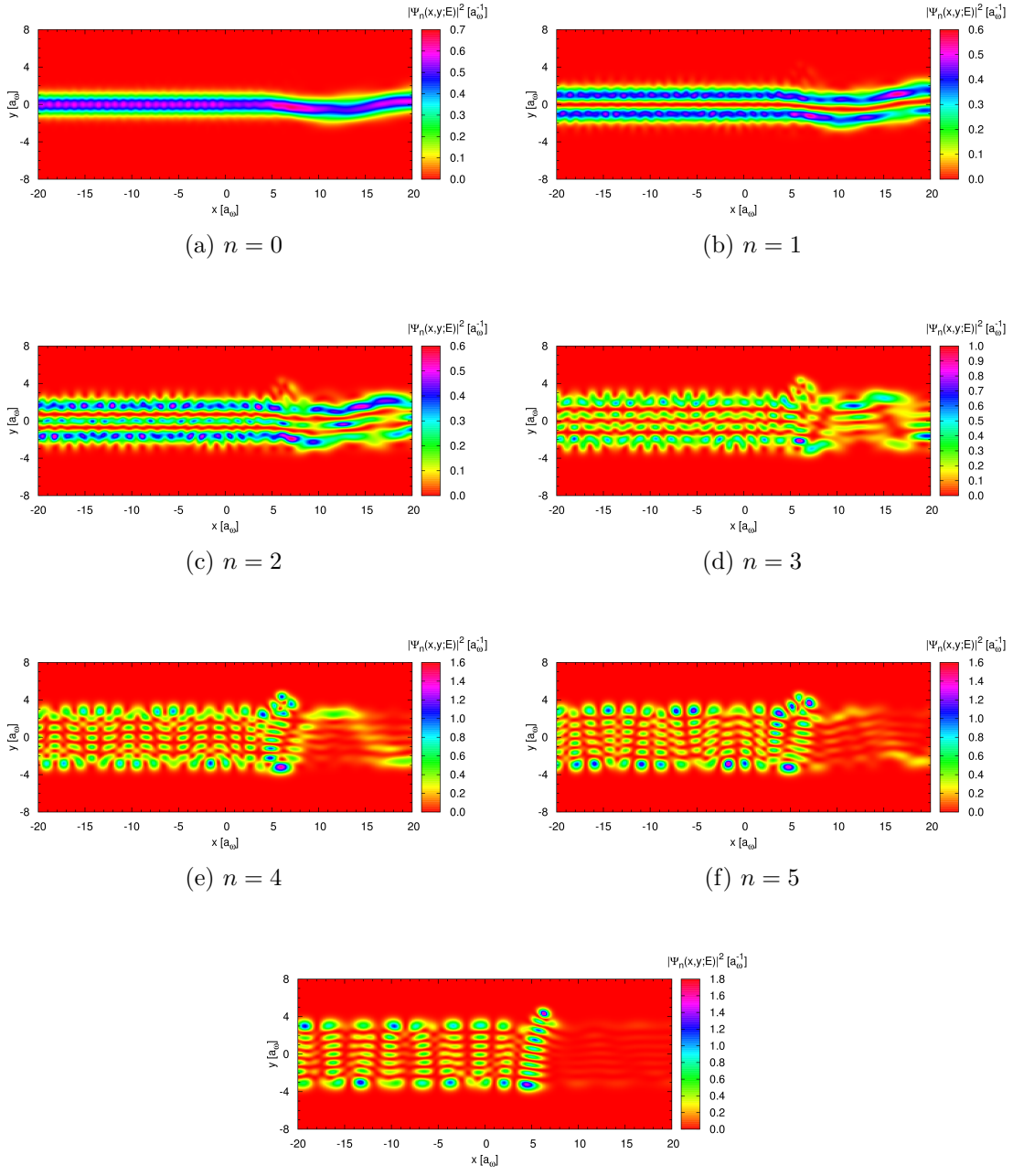

(a) $n = 0$ (b) $n = 1$

(c) $n = 2$ (d) $n = 3$

(e) $n = 4$ (f) $n = 5$

(g) $n = 6$

Figure 5.46: Quantum wire with a single side-coupled quantum dot and a step. The probability densities of the scattering states at $E = 14.981\,\varepsilon_0$ marked by $\boldsymbol{r}$ in figure 5.24.

5.3 Two Identical Quantum Dots

The transport through a quantum wire with a two side-coupled quantum dots is now investigated. These quantum dots are embedded on the opposite sides of the quantum wire and are parallel in the transverse y-direction. The scattering potential describing the two quantum dots is a sum of four Gaussian potentials

$$\begin{aligned} V_{\mathrm{sc}}(x,y) =& V_1 e^{-[\beta_{x,1}(x-x_1)^2+\beta_{y,1}(y-y_1)^2]} + V_2 e^{-[\beta_{x,2}(x-x_2)^2+\beta_{y,2}(y-y_2)^2]} \\ &+ V_3 e^{-[\beta_{x,3}(x-x_3)^2+\beta_{y,3}(y-y_3)^2]} + V_4 e^{-[\beta_{x,4}(x-x_4)^2+\beta_{y,4}(y-y_4)^2]}, \end{aligned} \tag{5.3}$$

where the parameters are

$$\begin{array}{llll} V_1 = -36.0\,\varepsilon_0, & x_1 = 6.0\,a_\omega, & y_1 = 4.0\,a_\omega, & \beta_{x,1} = \beta_{y,1} = 0.4\,a_\omega^{-2}, \\ V_2 = 20.0\,\varepsilon_0, & x_2 = 6.0\,a_\omega, & y_2 = 4.0\,a_\omega, & \beta_{x,2} = \beta_{y,2} = 0.2\,a_\omega^{-2}, \\ V_3 = -36.0\,\varepsilon_0 + \Delta V_3, & x_3 = 6.0\,a_\omega, & y_3 = -4.0\,a_\omega, & \beta_{x,3} = \beta_{y,3} = 0.4\,a_\omega^{-2}, \\ V_4 = 20.0\,\varepsilon_0, & x_4 = 6.0\,a_\omega, & y_4 = -4.0\,a_\omega, & \beta_{x,4} = \beta_{y,4} = 0.2\,a_\omega^{-2}. \end{array} \tag{5.4}$$

The first two Gaussian potentials describe the upper quantum dot as before and the second two the lower quantum dot. The quantum dots are identical apart from the small detuning parameter ΔV_3 which controls the depth of the lower quantum dot compared to the upper quantum dot. The detuning parameter will at first be kept at zero so the quantum dots are exactly identical. Detuning effect will be investigated in the following section.

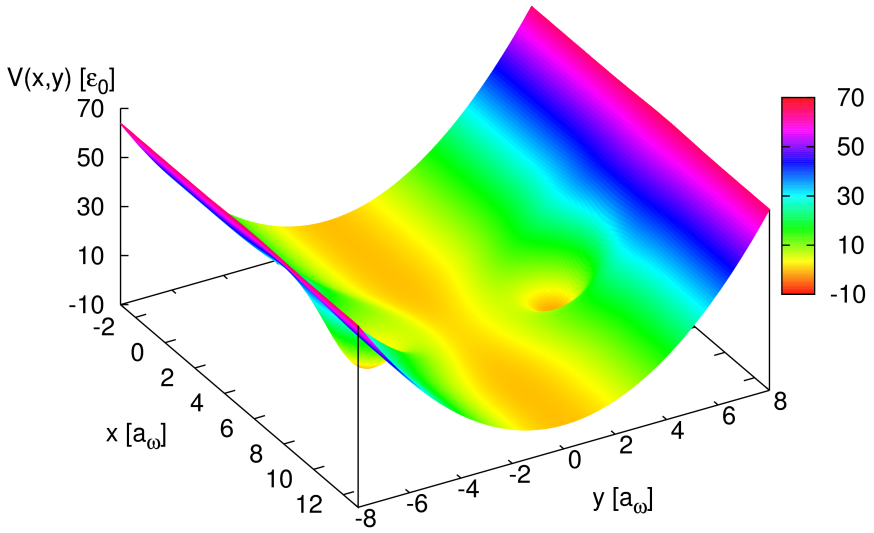

Figure 5.47: The potential distribution for a quantum wire with two side-coupled quantum dots.

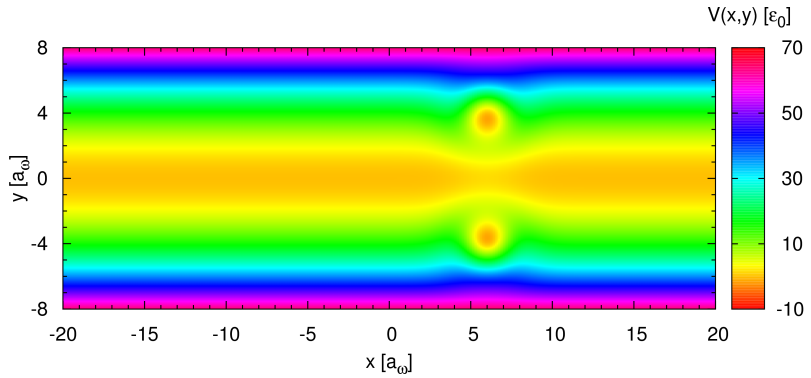

Figure 5.48: The potential distribution for a quantum wire with two side-coupled quantum dots. This is the same view as for the probability densities below.

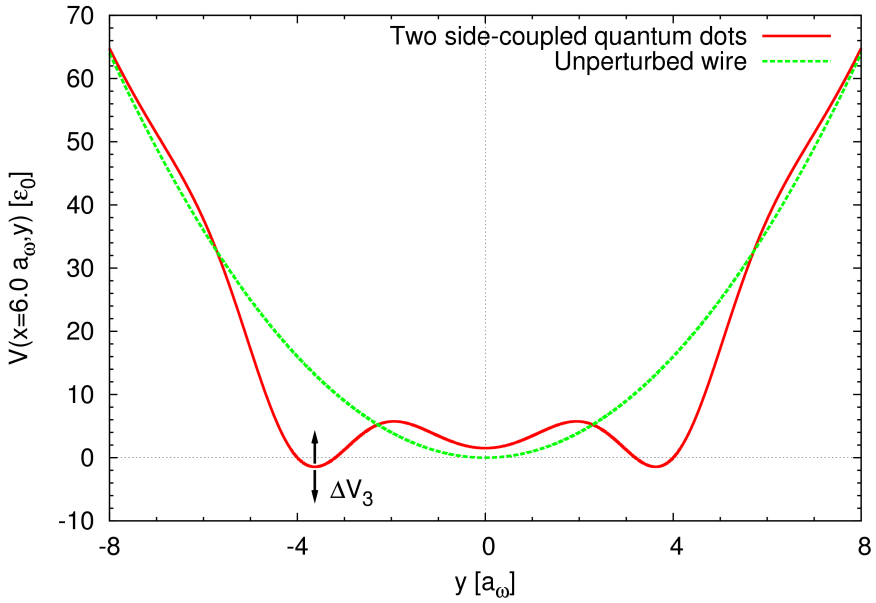

Figure 5.49: The potential distribution for a quantum wire with two side-coupled quantum dots. The cross section of the potential distribution along the transverse y-direction at the middle of the quantum dots at $x = 6\,a_\omega$.

Figures 5.47 and 5.48 show the potential distribution of the quantum wire system. Figure 5.49 shows the cross section of the potential distribution along the transverse y-direction at the middle of the quantum dots at $x = 6.0\,a_\omega$. The two quantum dots introduce a small constriction in the bottom of the wire around $x = 6.0\,a_\omega$. Also, there is a tunneling barrier between the bottom of the wire and the two quantum dot. The scattering potential is symmetric if the small detuning parameter is ignored. Thus, there are selection rules for the matrix elements, $V_{m,m'}(x)$ is only different from zero for m and m' both even or both odd.

Figure 5.50 shows the conductance of the quantum wire. Figure 5.51 shows a comparison of the conductance with the case of a single side-coupled quantum dot from before. The conductance is less than for a single quantum dot but that can be explained by the small constriction in the bottom of the wire introduced by the two quantum dots. Such a constriction was also present for a single quantum dot but was less pronounced there. The conductance is otherwise similar to the one for a single quantum dot. There is a sharp resonance peak-dip pair around $4\,\varepsilon_0$, shown in more detail in figure 5.52. It is much narrower than for a single quantum dot. It shows a symmetric Fano shape, as for a single quantum dot before. There is a small peak around $7\,\varepsilon_0$. A broader resonance structure is present around 8–$10\,\varepsilon_0$. There is a broad peak around $12\,\varepsilon_0$ and a small peak around $13\,\varepsilon_0$. Above $14\,\varepsilon_0$ there are oscillation with a periodic structure and an upward trend. The dips in the periodic structure are more pronounced than for a single quantum dot.

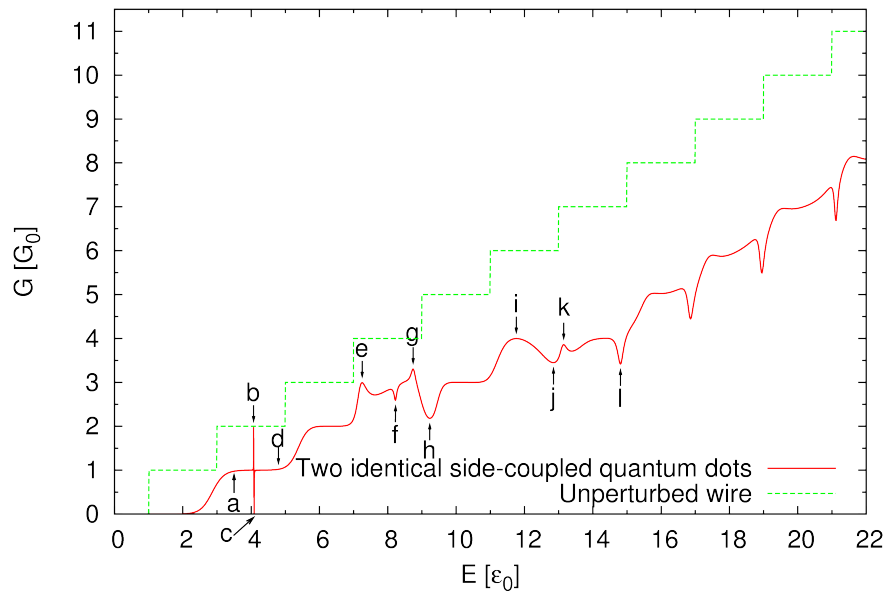

Figure 5.50: The conductance versus energy for a quantum wire with a two identical side-coupled quantum dots. For comparison the conductance of an unperturbed quantum wire is also shown.

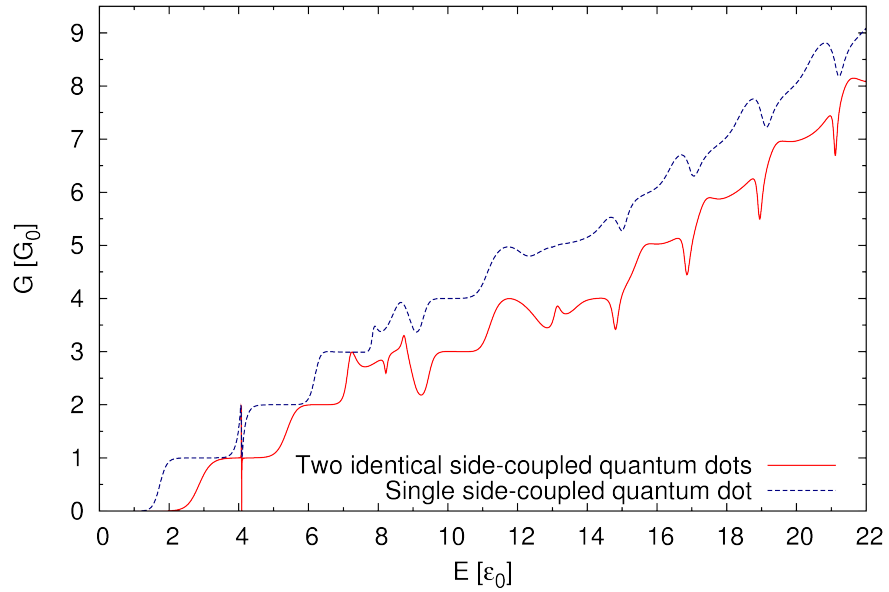

Figure 5.51: A comparison of the conductance versus energy for a quantum wire with two identical side-coupled quantum dots and a quantum wire with a single side-coupled quantum dot.

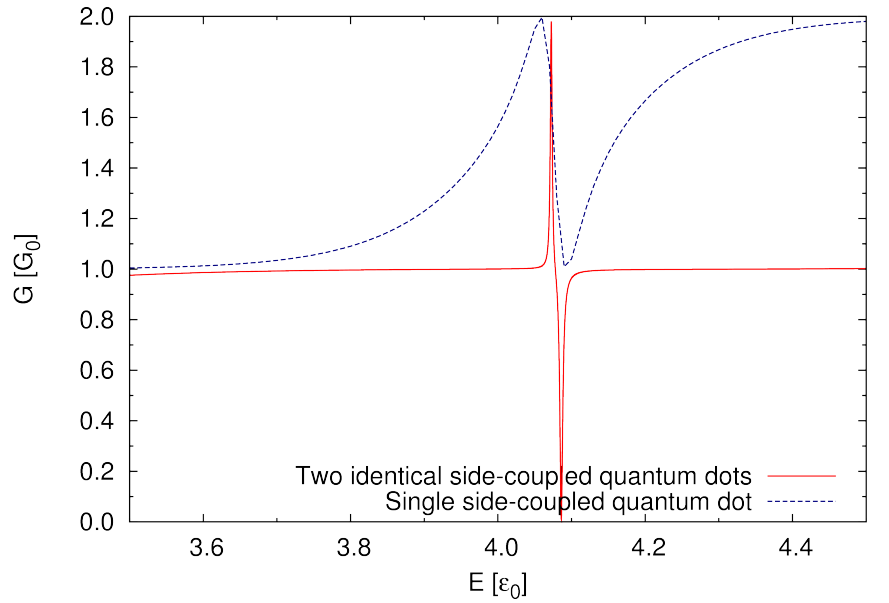

Figure 5.52: A comparison of the conductance versus energy for a quantum wire with two identical side-coupled quantum dots and a quantum wire with a single side-coupled quantum dot. The resonance peak-dip pair around $4\,\epsilon_0$ is shown in more detail.

The probability densities of the scattering states which are marked by the arrows in figure 5.50 will now be investigated.

The probability densities of the scattering states at $E = 3.5\,\varepsilon_0$ which are marked by ***a*** in figure 5.50 are shown in figure 5.53. The scattering states look very similar to the corresponding scattering states for a single quantum dot. Here, the scattering potential is fully symmetric so there is no wriggle motion or other asymmetrical effects as observed for a single quantum dot.

The probability densities for the resonance peak at $E = 4.0725\,\varepsilon_0$ which is marked by ***b*** in figure 5.50 are shown in figure 5.54. The scattering states show quasi-bound states in both quantum dots. The extended state is barely visible for the $n = 1$ scattering state and not visible at all for the $n = 0$ scattering state. It should be noted that these scattering states are delocalized since there is a propability for the presence of the electrons in two essentially unrelated quantum dots. Figure 5.55 shows the square root of the probability densities. The fully transmitting extended states in the wire are visible. Also, tunneling between the extended states and the quasi-bound states is visible.

Figure 5.56 shows the probability densities for the resonance dip at $E = 4.0861\,\varepsilon_0$ which is marked by ***c*** in figure 5.50. The $n = 0$ scattering state shows a stronger quasi-bound states than the $n = 1$ scattering state. This is different from the case of a single quantum dot where the $n = 1$ scattering state showed a stronger quasi-bound state than the $n = 0$ scattering state. Figure 5.57 shows the square root of the probability densities.

The quantum wire system is symmetrical in the transverse y-direction so the wavefunctions should be symmetric and antisymmetric in the y-direction. Figures 5.58 and 5.59 show the cross sections of the wavefunctions for the peak and the dip around $4\,\varepsilon_0$. The cross sections are along the transverse y-direction at the middle of the quantum dots, i.e. $x = 6\,a_\omega$. The $n = 0$ scattering states have symmetric wavefunctions and the $n = 1$ scattering states have antisymmetric wavefunctions. This can be explained by referring to the discussion of the confinement potential in section 2.3. The subbands have symmetric wavefunctions in the y-direction if n is a even number and antisymmetric if n is a odd number. A scattering state where the incoming subband has an even n can only couple with subbands where m is even, and the same for odd n. Thus, for a symmetric scattering potential all the scattering state with even n have symmetric wavefunctions and all the scattering states where n is odd have antisymmetric wavefunctions.

The probability densities for the scattering states at $E = 4.80\,\varepsilon_0$ which are marked by ***d*** in figure 5.50 are shown in figure 5.60. The scattering states look very similar to the scattering states at $E = 3.50\,\varepsilon_0$ shown in figure 5.53. The main difference is that the energy is higher so the wavelengths are shorter. Thus, the spacing between peaks in the beating pattering is shorter.

The probability densities for the small peak at $E = 7.25\,\varepsilon_0$ which is marked by ***e*** in figure 5.50 are shown in figure 5.61. The $n = 2$ scattering state seems to show a short lived quasi-bound state between the two quantum dots. Some tunneling

into the quantum dots is also visible. The structure in the quantum dots can not be characterized by the eigenstates of the closed quantum dot. This peak is at an energy where there was no conductance structure for a single quantum dot. Thus, this peak seems to be due to an effective well defined between the two quantum dots.

The probability densities for the scattering states at the resonance structure around 8–10 ε_0 which are marked by $\boldsymbol{f}$, $\boldsymbol{g}$, and $\boldsymbol{h}$ in figure 5.50 are shown in figures 5.62, 5.63, and 5.64, respectively. If the symmetry is ignored can some similarities to the corresponding scattering states for a single quantum dot be seen. Some of the scattering states look almost like the single quantum dot scattering states have been mirrored about the x-axis. This can for example be seen by comparing the $n = 3$ scattering states shown in figures 5.15 and 5.63. The structure around the quantum dot is clearer than for the case of a single quantum dot but this is probably due to the symmetry of the system. The quasi-bound states in quantum dots correspond to a mixture of the second and third eigenstates of the closed quantum dot, as for a single quantum dot before.

The probability densities for the scattering states higher in energy which are marked by $\boldsymbol{i}$, $\boldsymbol{j}$, $\boldsymbol{k}$, and $\boldsymbol{l}$ in figure 5.50 are shown in figures 5.65, 5.66, 5.67, and 5.68, respectively. Many of these scattering states are, if the symmetry is ignored, similar to the corresponding scattering states for a single quantum dot. The structure around the quantum dots is much clearer than for a single dot and shows indications of the fourth, fifth, and sixth eigenstates of the closed quantum dot.

The wriggle structure seen in the scattering states for a single dot is of course not visible since it is due to asymmetrical scattering. However, another interesting structure can be noted. This structure can for example be seen in the $n = 1$ scattering state in figure 5.65 and the $n = 0, 1$ scattering states in figure 5.66. Right of the quantum dots there is a structure that can not be characterized by the motion of a single classical particle. It could possibly be characterized by the motion of two classical particles or as pressure fluctuations in a classical fluid or gas flowing along the wire.

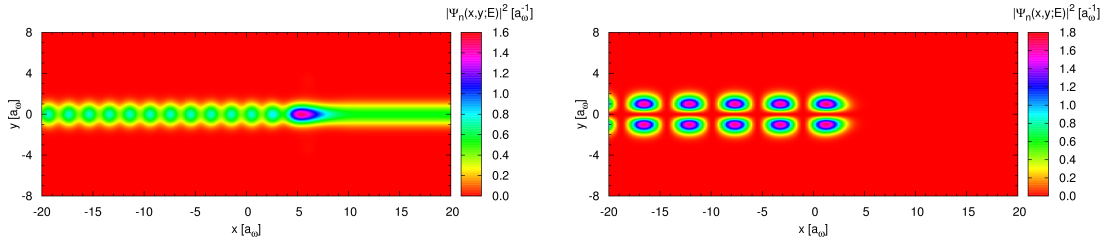

(a) $n = 0$ (b) $n = 1$

Figure 5.53: Quantum wire with two identical side-coupled quantum dots. The probability densities of the scattering states at $E = 3.5\,\varepsilon_0$ marked by ***a*** in figure 5.50.

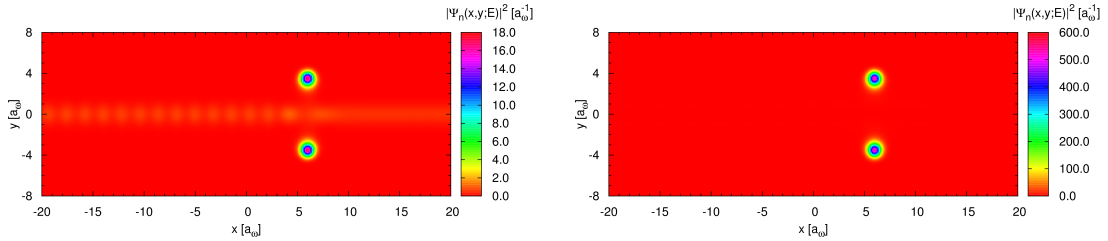

(a) $n = 0$ (b) $n = 1$

Figure 5.54: Quantum wire with two identical side-coupled quantum dots. The probability densities of the scattering states at $E = 4.0725\,\varepsilon_0$ marked by ***b*** in figure 5.50.

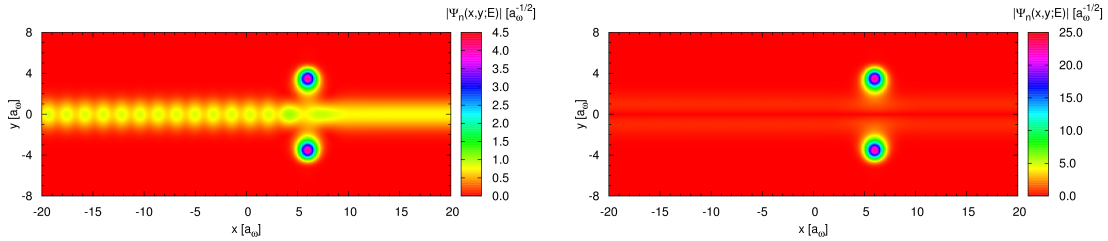

(a) $n = 0$ (b) $n = 1$

Figure 5.55: Quantum wire with two identical side-coupled quantum dots. The square root of the probability densities at $E = 4.0725\,\varepsilon_0$ marked by ***b*** in figure 5.50. The square root is taken to compress the color scale of the probability densities shown in figure 5.54.

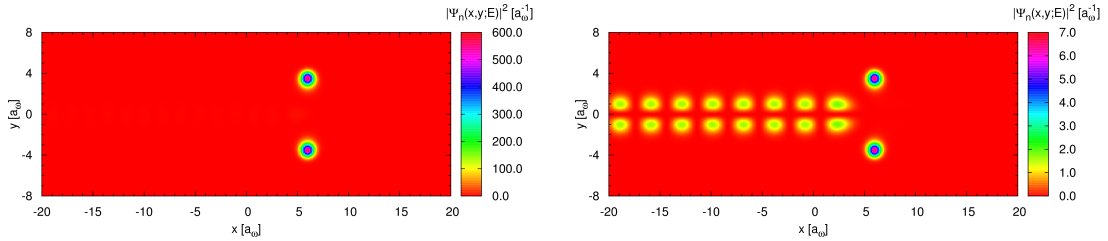

(a) $n = 0$ (b) $n = 1$

Figure 5.56: Quantum wire with two identical side-coupled quantum dots. The probability densities of the scattering states at $E = 4.0861\,\varepsilon_0$ marked by $\boldsymbol{c}$ in figure 5.50.

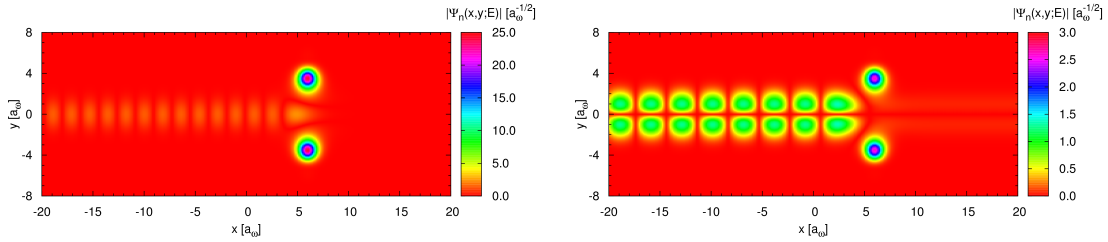

(a) $n = 0$ (b) $n = 1$

Figure 5.57: Quantum wire with two identical side-coupled quantum dots. The square root of the probability densities at $E = 4.0861\,\varepsilon_0$ marked by $\boldsymbol{c}$ in figure 5.50. The square root is taken to compress the color scale of the probability densities shown in figure 5.56.

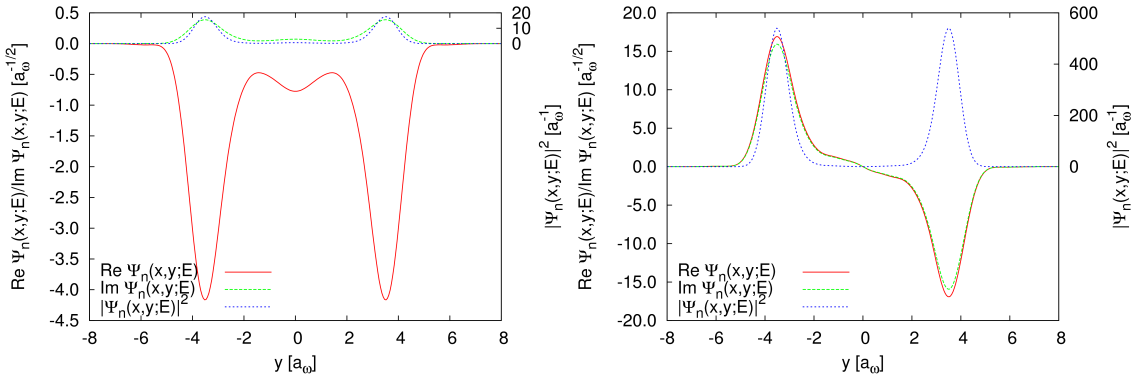

(a) $n = 0$ (b) $n = 1$

Figure 5.58: Quantum wire with two identical side-coupled quantum dots. The cross section of the wavefunctions along the transverse y-direction at the middle of the quantum dots at $x = 6.0\,a_\omega$ for $E = 4.0725\,\varepsilon_0$ marked by $\boldsymbol{b}$ in figure 5.50.

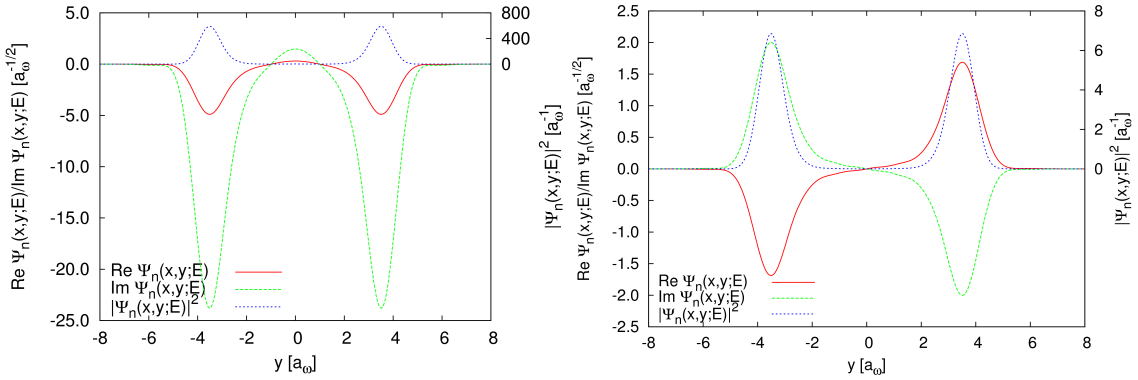

(a) $n = 0$ (b) $n = 1$

Figure 5.59: Quantum wire with two identical side-coupled quantum dots. The cross section of the wavefunctions along the transverse y-direction at the middle of the quantum dots at $x = 6.0\,a_\omega$ for $E = 4.0861\,\varepsilon_0$ marked by $\boldsymbol{c}$ in figure 5.50.

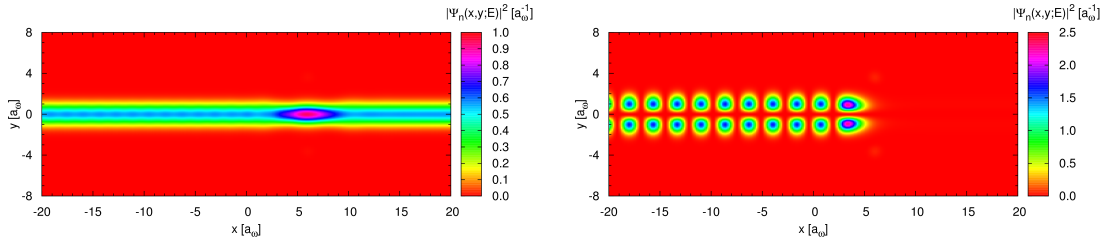

(a) $n = 0$ (b) $n = 1$

Figure 5.60: Quantum wire with two identical side-coupled quantum dots. The probability densities of the scattering states at $E = 4.8\,\varepsilon_0$ marked by ***d*** in figure 5.50.

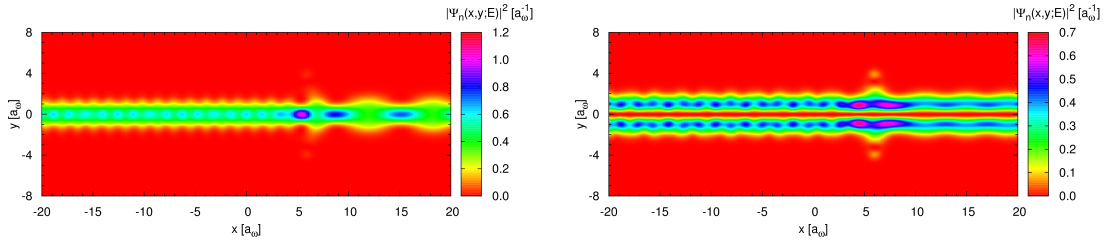

(a) $n = 0$ (b) $n = 1$

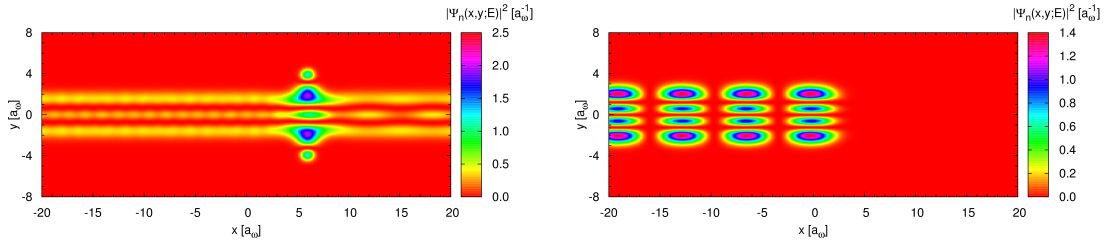

(c) $n = 2$ (d) $n = 3$

Figure 5.61: Quantum wire with two identical side-coupled quantum dots. The probability densities of the scattering states at $E = 7.25\,\varepsilon_0$ marked by ***e*** in figure 5.50.

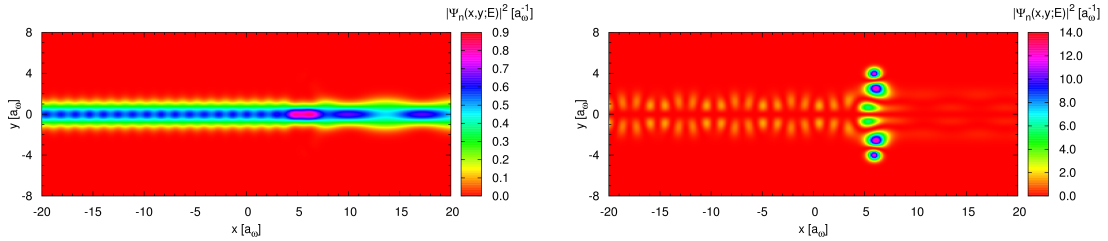

(a) $n = 0$ (b) $n = 1$

(c) $n = 2$ (d) $n = 3$

Figure 5.62: Quantum wire with two identical side-coupled quantum dots. The probability densities of the scattering states at $E = 8.22\,\varepsilon_0$ marked by $\boldsymbol{f}$ in figure 5.50.

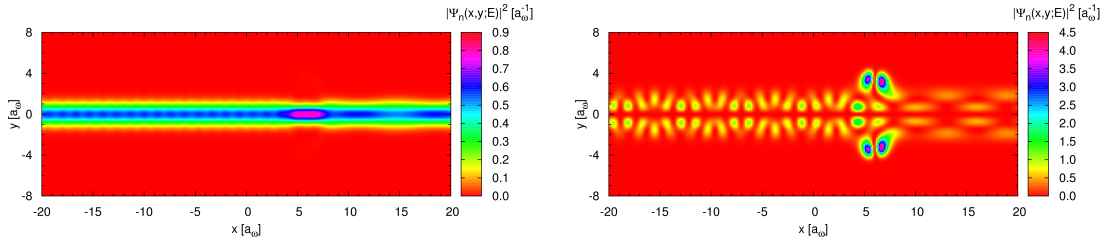

(a) $n = 0$ (b) $n = 1$

(c) $n = 2$ (d) $n = 3$

Figure 5.63: Quantum wire with two identical side-coupled quantum dots. The probability densities of the scattering states at $E = 8.74\,\varepsilon_0$ marked by $\boldsymbol{g}$ in figure 5.50.

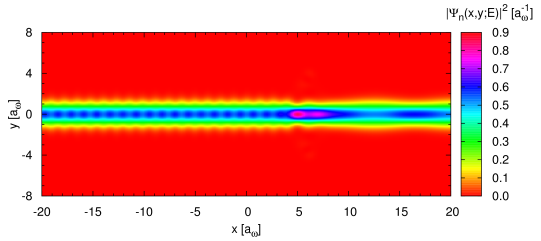

(a) $n = 0$

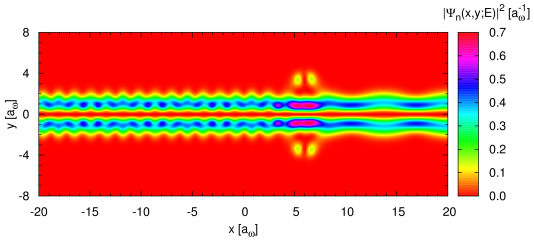

(b) $n = 1$

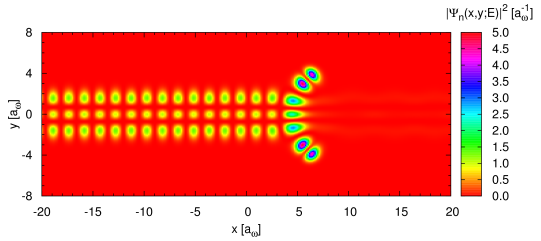

(c) $n = 2$

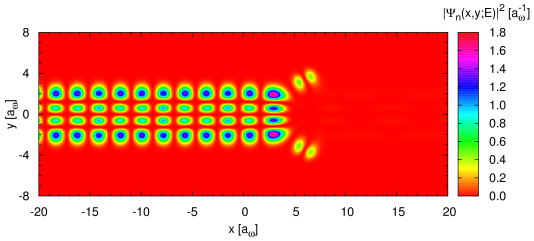

(d) $n = 3$

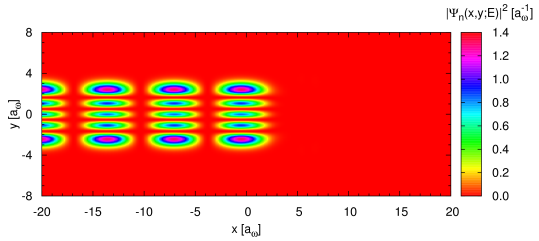

(e) $n = 4$

Figure 5.64: Quantum wire with two identical side-coupled quantum dots. The probability densities of the scattering states at $E = 9.23\,\varepsilon_0$ marked by ***h*** in figure 5.50.

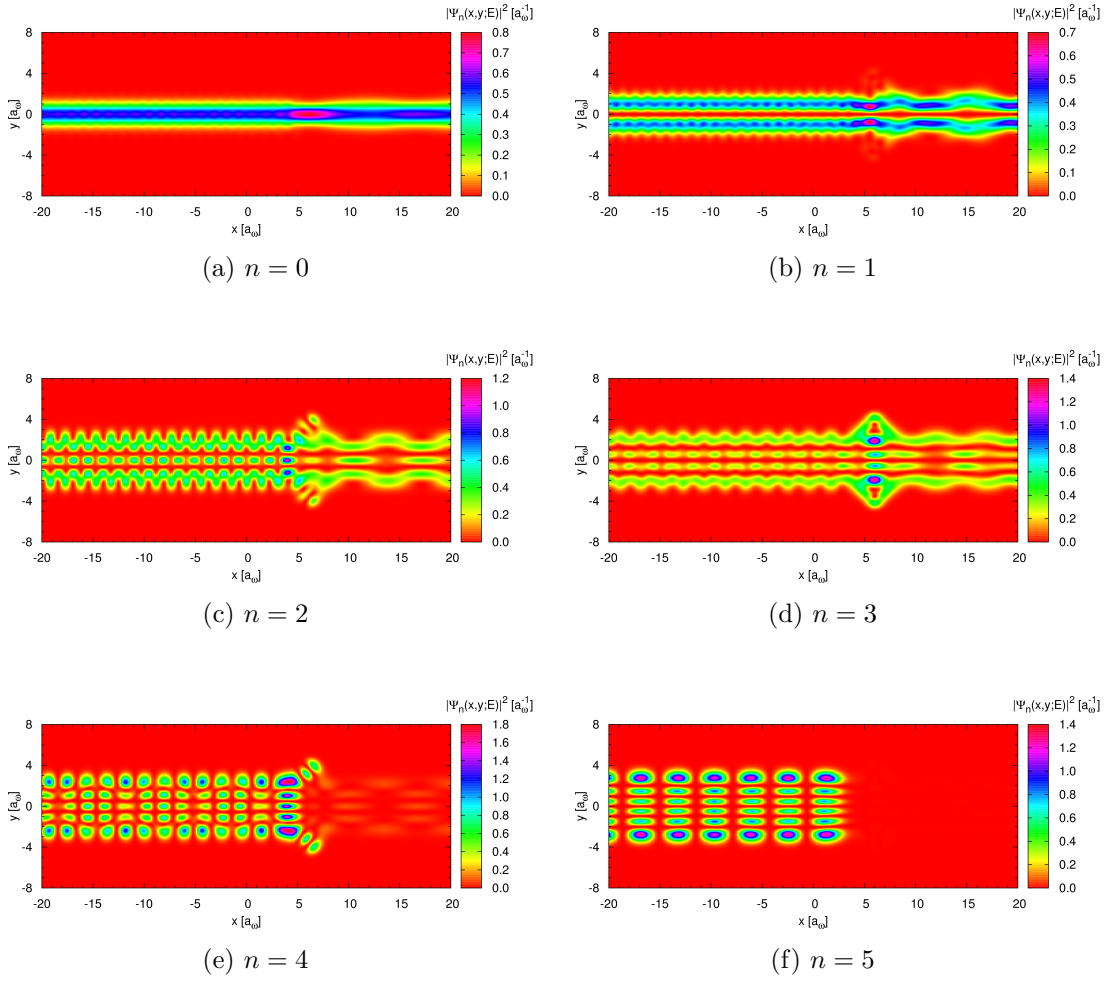

(a) $n = 0$ (b) $n = 1$

(c) $n = 2$ (d) $n = 3$

(e) $n = 4$ (f) $n = 5$

Figure 5.65: Quantum wire with two identical side-coupled quantum dots. The probability densities of the scattering states at $E = 11.76\,\varepsilon_0$ marked by ***i*** in figure 5.50.

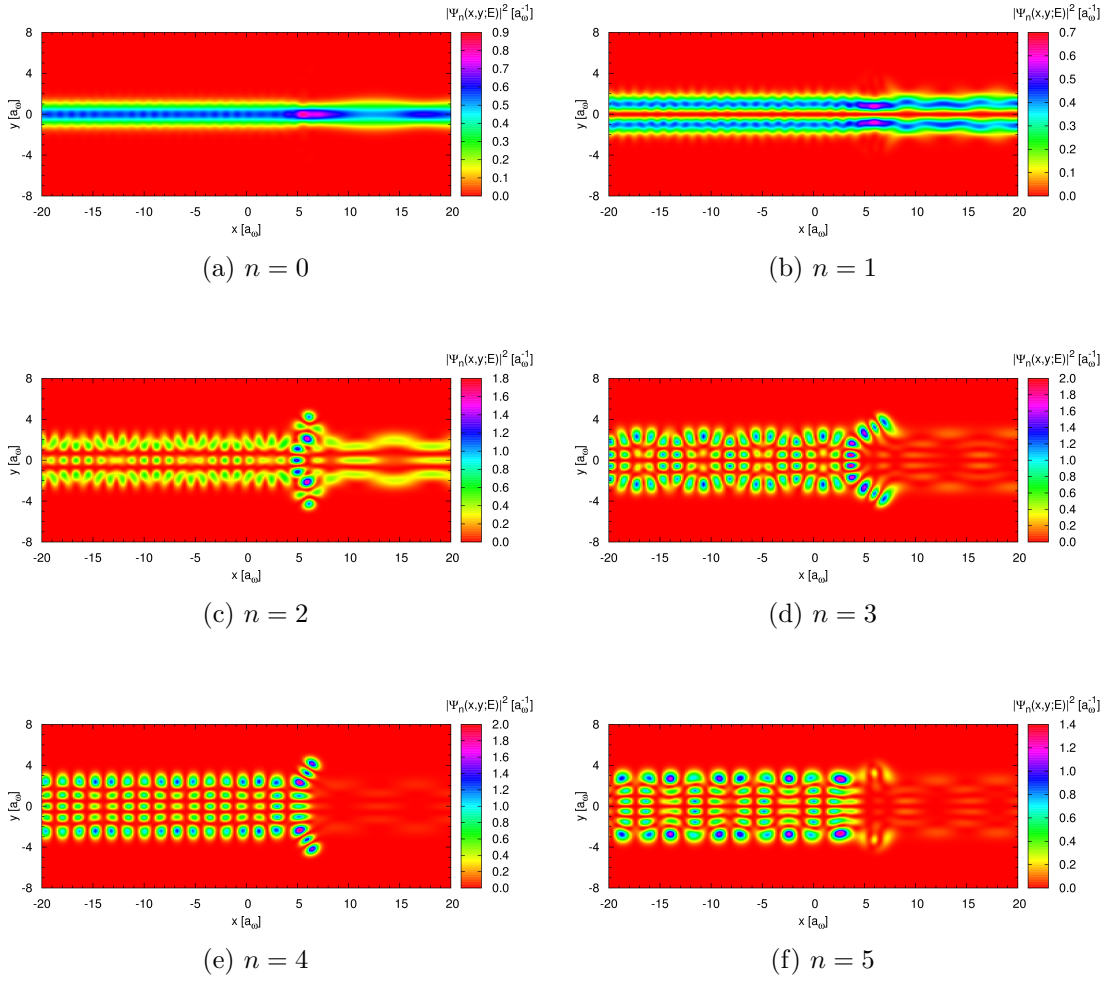

(a) $n = 0$ (b) $n = 1$

(c) $n = 2$ (d) $n = 3$

(e) $n = 4$ (f) $n = 5$

Figure 5.66: Quantum wire with two identical side-coupled quantum dots. The probability densities of the scattering states at $E = 12.85\,\varepsilon_0$ marked by $\boldsymbol{j}$ in figure 5.50.

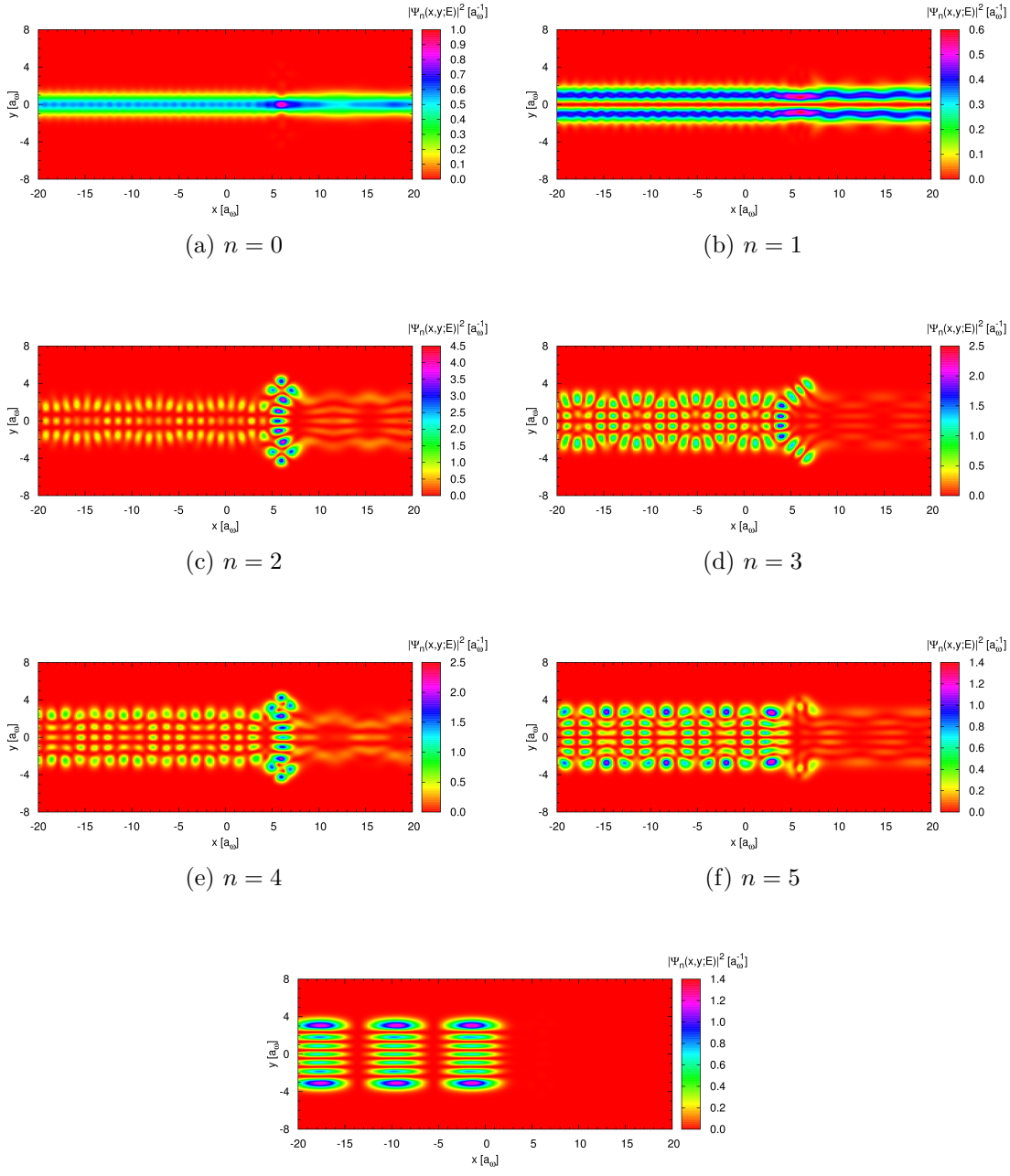

(a) $n = 0$ (b) $n = 1$

(c) $n = 2$ (d) $n = 3$

(e) $n = 4$ (f) $n = 5$

(g) $n = 6$

Figure 5.67: Quantum wire with two identical side-coupled quantum dots. The probability densities of the scattering states at $E = 13.15\,\varepsilon_0$ marked by $\boldsymbol{k}$ in figure 5.50.

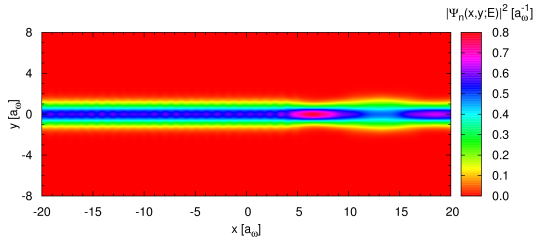

(a) $n = 0$

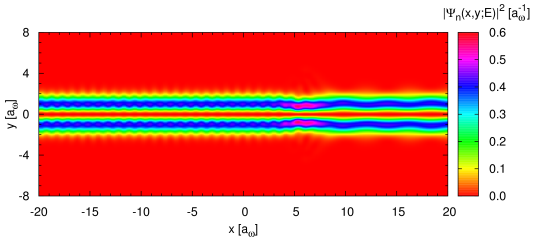

(b) $n = 1$

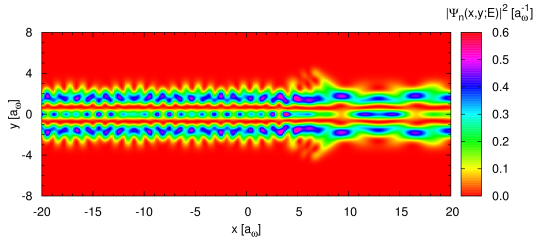

(c) $n = 2$

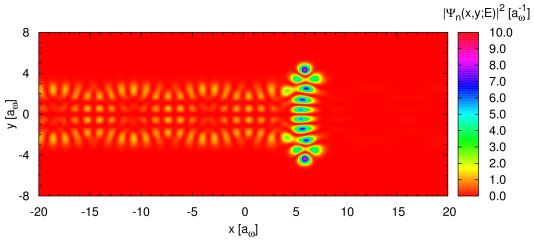

(d) $n = 3$

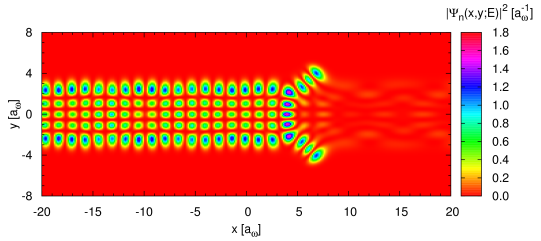

(e) $n = 4$

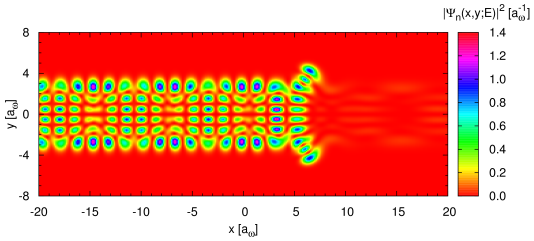

(f) $n = 5$

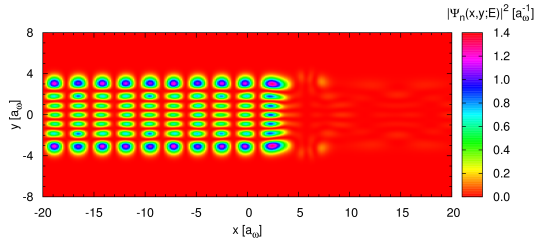

(g) $n = 6$

Figure 5.68: Quantum wire with two identical side-coupled quantum dots. The probability densities of the scattering states at $E = 14.81\,\varepsilon_0$ marked by ***1*** in figure 5.50.

5.4 Two Detuned Quantum Dots

The effects of detuning for the two side-coupled quantum dots is now investigated. The detuning parameter ΔV_3 controls the depth of the lower quantum dot compared to the upper quantum dot. Thus, it is expected that the energy positions of the quasi-bound states in the lower quantum dot will move. However, the quasi-bound states in the upper quantum dot should stay approximately stationary in the same positions. The values used for the detuning parameter are small compared to the overall scattering potential. There would be no indication of the detuning in the potential distribution on the scales used in figures 5.47, 5.48, and 5.49.

The detuning only has an effect on the conductance structure around $4\,\varepsilon_0$, i.e. the narrow resonance peak-dip pair. There is no effect on the conductance structure higher in energy. This is expected since the detuning parameter is very small on the scale of the conductance structure higher in energy. Thus, the focus will be on the conductance structure around $4\,\varepsilon_0$ and only the energy range around it shown. Figures 5.69 and 5.70 show the conductance versus energy and detuning parameter. Figures 5.71, 5.72, and 5.73 show the conductance versus energy for various values of the detuning parameter.

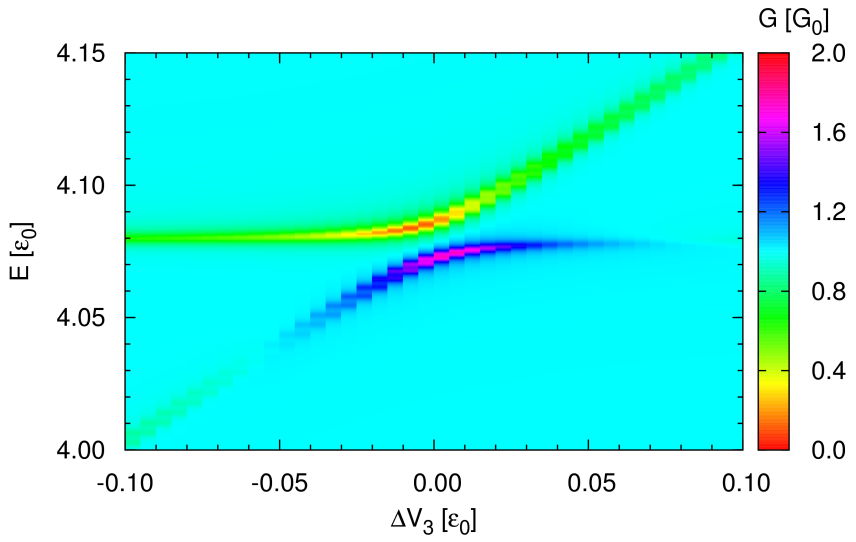

Figure 5.69: Quantum wire with two detuned side-coupled quantum dots. Focus on the conductance structure around $4\,\varepsilon_0$. The conductance versus energy and detuning parameter ΔV_3. Note that the raggedness of the figure is due to the resolution in the detuning parameter.

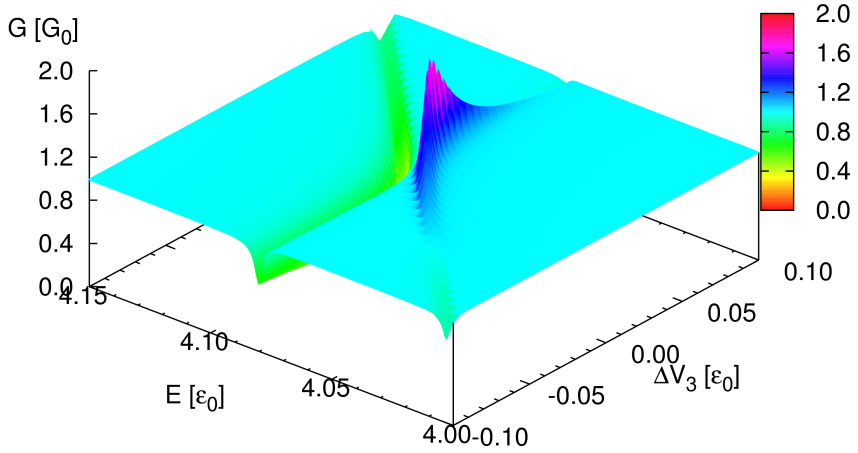

Figure 5.70: Quantum wire with two detuned side-coupled quantum dots. Focus on the conductance structure around $4\,\varepsilon_0$. The conductance versus energy and detuning parameter ΔV_3. Note that the raggedness of the figure is due to the resolution in the detuning parameter.

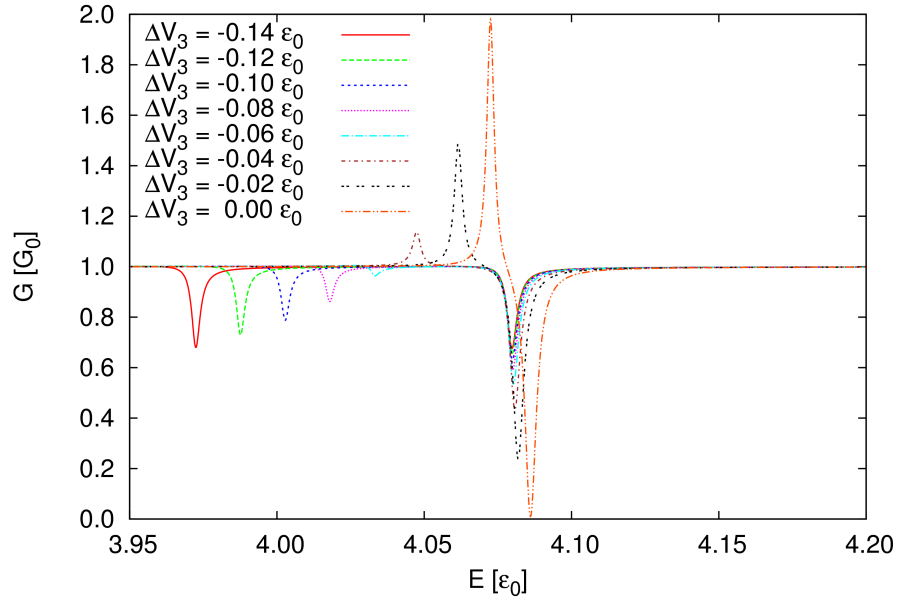

Figure 5.71: Quantum wire with two detuned side-coupled quantum dots. Focus on the conductance structure around $4\,\varepsilon_0$. The conductance versus energy for negative values of the detuning parameter ΔV_3.

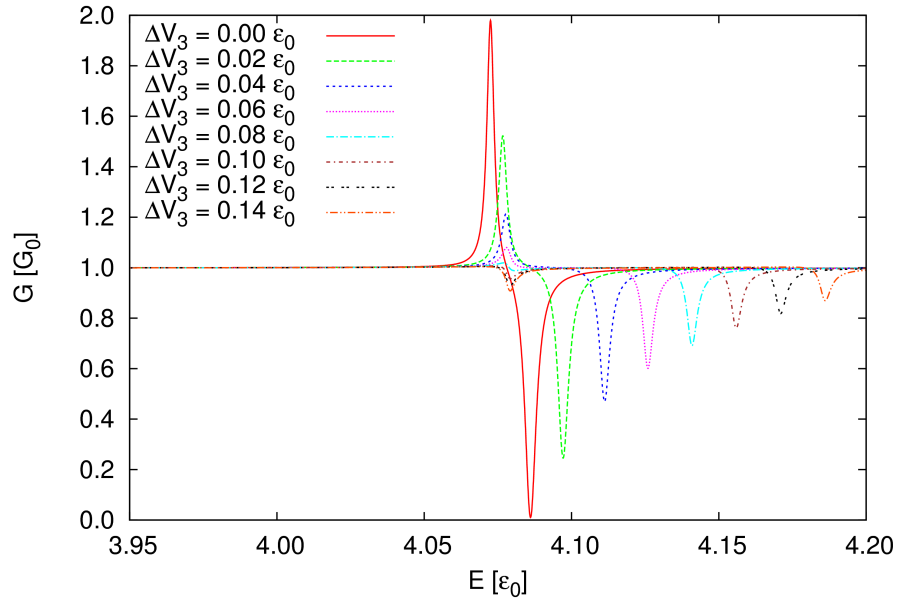

Figure 5.72: Quantum wire with two detuned side-coupled quantum dots. Focus on the conductance structure around $4\,\varepsilon_0$. The conductance versus energy for positive values of the detuning parameter ΔV_3.

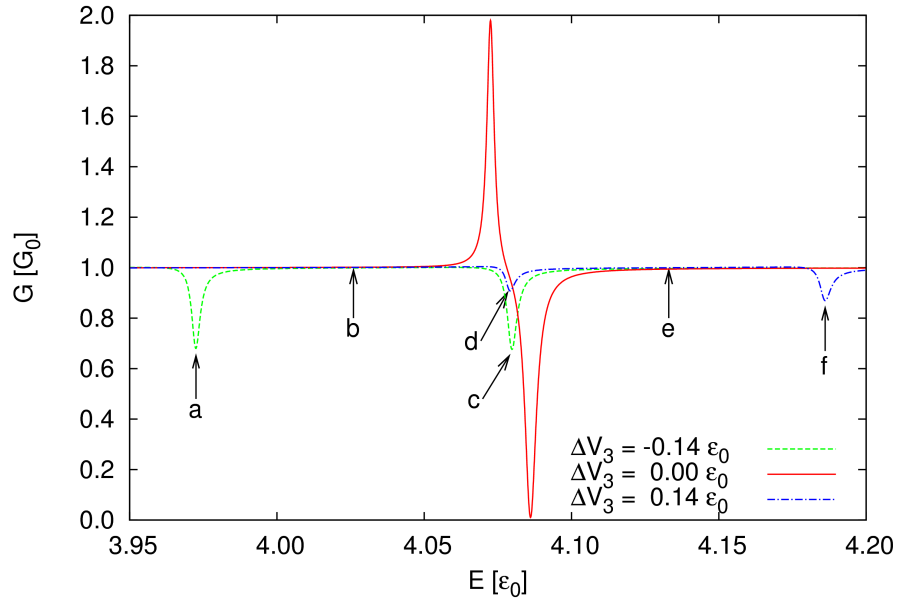

Figure 5.73: Quantum wire with two detuned side-coupled quantum dots. Focus on the conductance structure around $4\,\varepsilon_0$. The conductance versus energy for values of the detuning parameter ΔV_3.

Figure 5.71 shows the conductance as the detuning parameter is decreased from zero to negative values. The dip stays nearly in the same position and becomes shallower. The peak, however, moves lower in energy and becomes smaller until it crosses over to a deepening dip somewhere between $\Delta V_3 = -0.04\,\varepsilon_0$ and $\Delta V_3 = -0.06\,\varepsilon_0$. Figure 5.72 shows the conductance as the detuning parameter is increased from zero to positive values. The dip moves higher in energy and becomes shallower. The peak, however, stays in nearly the same place. It becomes smaller until it is barely visible around $\Delta V_3 = 0.08\,\varepsilon_0$, then it crosses over to a deepening dip. Thus, there is a similar effect for both negative and positive values of the detuning parameter as it is shifted from zero. There is a crossover of the conductance structure around $4\,\varepsilon_0$ from a peak-dip pair over to two dips. Figure 5.69 shows that sufficiently far from the zero point of the detuning parameter the energy position of the moving resonance structure, the peak or the dip, depends linearly on the detuning parameter. Also, a avoided crossing of the peak and the dip is visible.

The probability densites of the scattering states for $\Delta V_3 = \pm 0.14\,\varepsilon_0$ where the peak has crossed over to a dip will now investigated. They are marked by $\boldsymbol{a}$, $\boldsymbol{b}$, $\boldsymbol{c}$, $\boldsymbol{d}$, $\boldsymbol{e}$, and $\boldsymbol{f}$ in figure 5.73 and shown in figures 5.74, 5.75, 5.76, 5.77, 5.78, and 5.79, respectively. All the scattering states at the dips show quasi-bound states only in a single quantum dot and not in both quantum dots as for identical quantum dots. Furthermore, the scattering states between the dips do not show strong quasi-bound states in the quantum dots. The detuning has thus separated the quasi-bound states in the two quantum dots.

It is expected that the moving resonance structure should correspond to a quasi-bound state in the lower quantum dot. However, the stationary resonance structure should correspond to a quasi-bound state in the upper quantum dot. This is confirmed by the probability densites of the scattering states for $\Delta V_3 = \pm 0.14\,\varepsilon_0$. For a negative value of $\Delta V_3 = -0.14\,\varepsilon_0$ the dip lower in energy shown in figure 5.74, which was the moving resonance structure, corresponds to a quasi-bound state in the lower quantum dot. However, for a positive value of $\Delta V_3 = 0.14\,\varepsilon_0$ the dip higher in energy shown in figure 5.79, which was the moving resonance structure, corresponds to a quasi-bound state in the lower quantum dot. This is exactly what was expected. This change in character of the moving resonance structure when going from a negative values to a positive values of the detuning parameter is connected to the avoided crossing of the peak and dip seen in figure 5.69.

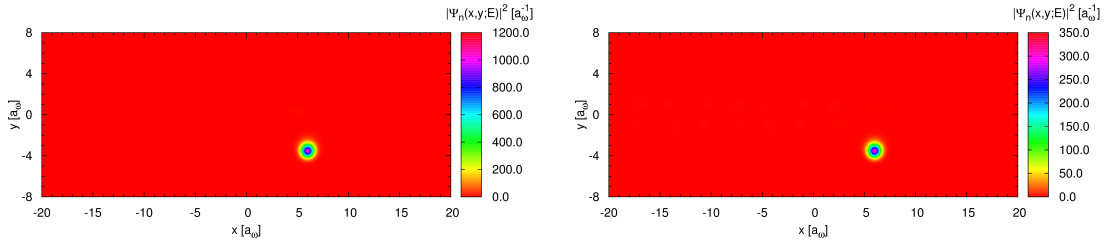

(a) $n = 0$ (b) $n = 1$

Figure 5.74: Quantum wire with two detuned side-coupled quantum dots. The detuning parameter is $\Delta V_3 = -0.14\,\varepsilon_0$. The probability densities of the scattering states at $E = 3.9725\,\varepsilon_0$ marked by ***a*** in figure 5.73.

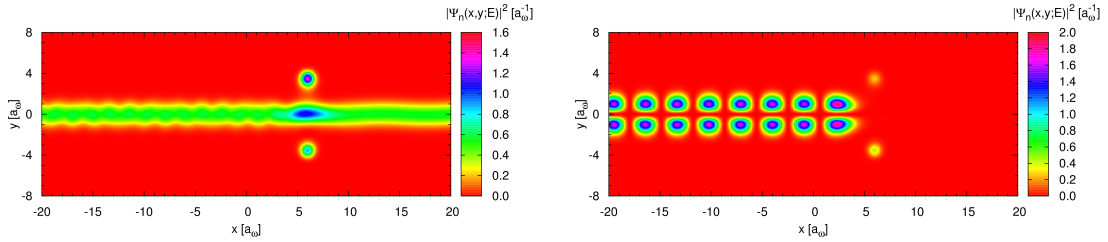

(a) $n = 0$ (b) $n = 1$

Figure 5.75: Quantum wire with two detuned side-coupled quantum dots. The detuning parameter is $\Delta V_3 = -0.14\,\varepsilon_0$. The probability densities of the scattering states at $E = 4.0260\,\varepsilon_0$ marked by ***b*** in figure 5.73.

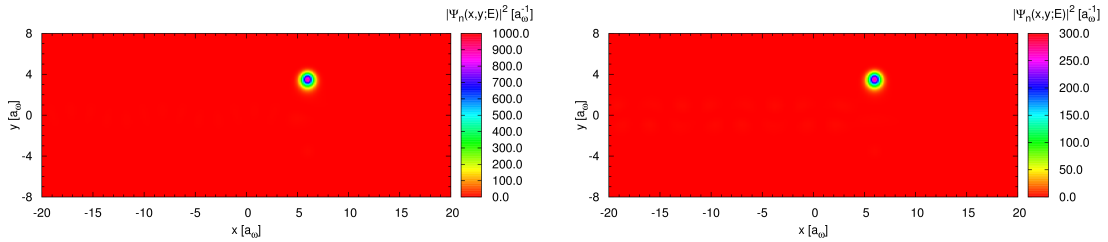

(a) $n = 0$ (b) $n = 1$

Figure 5.76: Quantum wire with two detuned side-coupled quantum dots. The detuning parameter is $\Delta V_3 = -0.14\,\varepsilon_0$. The probability densities of the scattering states at $E = 4.0798\,\varepsilon_0$ marked by ***c*** in figure 5.73.

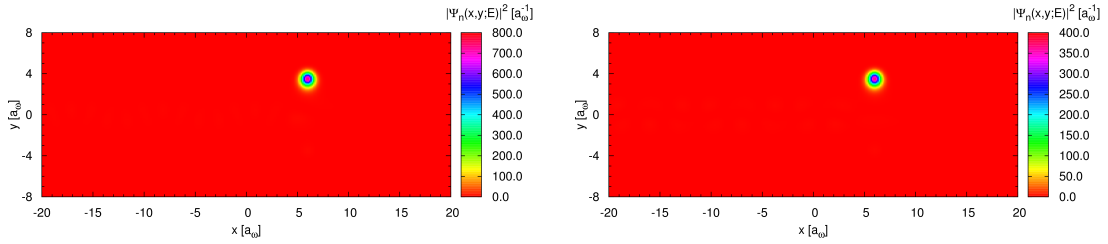

(a) $n = 0$ (b) $n = 1$

Figure 5.77: Quantum wire with two detuned side-coupled quantum dots. The detuning parameter is $\Delta V_3 = 0.14\,\varepsilon_0$. The probability densities of the scattering states at $E = 4.0792\,\varepsilon_0$ marked by ***d*** in figure 5.73.

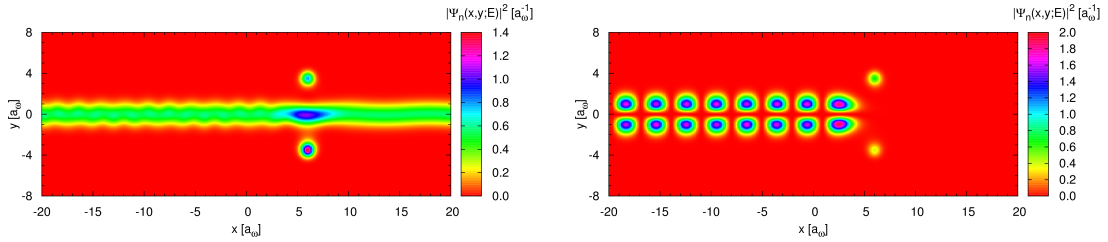

(a) $n = 0$ (b) $n = 1$

Figure 5.78: Quantum wire with two detuned side-coupled quantum dots. The detuning parameter is $\Delta V_3 = 0.14\,\varepsilon_0$. The probability densities of the scattering states at $E = 4.1330\,\varepsilon_0$ marked by ***e*** in figure 5.73.

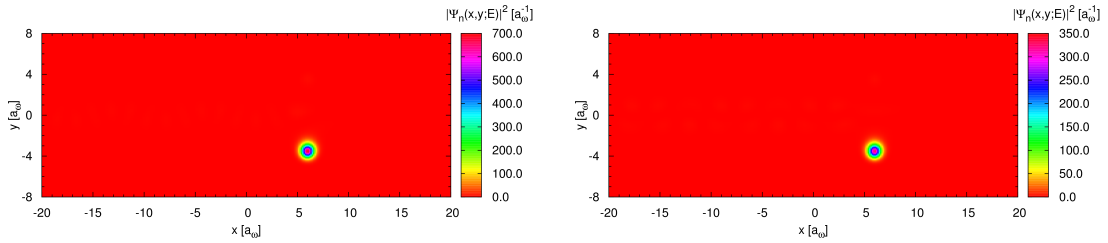

(a) $n = 0$ (b) $n = 1$

Figure 5.79: Quantum wire with two detuned side-coupled quantum dots. The detuning parameter is $\Delta V_3 = 0.14\,\varepsilon_0$. The probability densities of the scattering states at $E = 4.1861\,\varepsilon_0$ marked by ***f*** in figure 5.73.

5.4.1 Bound state in the continuum

The crossover from a peak to a dip warrants a further investigation. It was somewhere between $\Delta V_3 = -0.04\,\varepsilon_0$ and $\Delta V_3 = -0.06\,\varepsilon_0$ for negative values of the detuning parameter. Figures 5.80 and 5.81 show how the peak evolves to a dip as the detuning parameter is varied. The peak continuously gets smaller until there is only a small blip for $\Delta V_3 = -0.055\,\varepsilon_0$ and then crosses over to a dip. Figure 5.81 shows that compared to the dip higher in energy the blip is almost a straight line. Thus, for $\Delta V_3 = -0.055\,\varepsilon_0$ is only a single dip effectively visible.

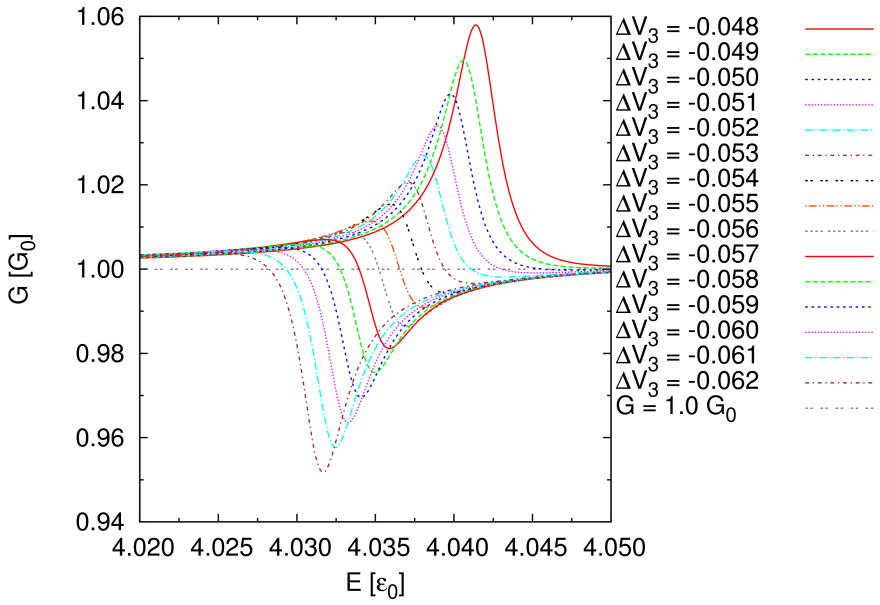

Figure 5.80: Quantum wire with two detuned side-coupled quantum dots. Focus on the crossover from a peak to a dip in the conductance structure around $4\,\varepsilon_0$. The conductance versus energy for positive values of the detuning parameter ΔV_3.

Figures 5.82, 5.85, and 5.86 show the probability densities of the scattering states for $\Delta V_3 = -0.055\,\varepsilon_0$ which are marked by ***g***, ***h***, and ***i*** in figure 5.81. Most interesting are the scattering states at the small blip which are shown in figure 5.85. They show a strong quasi-bound state in the lower quantum dot. However, there is no indication in the conductance of a strong quasi-bound state other than the small blip. Normally such a blip would not be associated with a strong quasi-bound state. This quasi-bound state is almost as strong as the quasi-bound state in the upper quantum dot which is visible in the scattering states at the dip shown in figure 5.86. However, there is no strong quasi-bound state in the scattering states situated between the blip and the dip which are shown in figure 5.85. Figure 5.83 shows the scattering states at the blip with a considerably shortened color scale. There, the extended states show an interesting asymmetrical scattering and band-mixing.

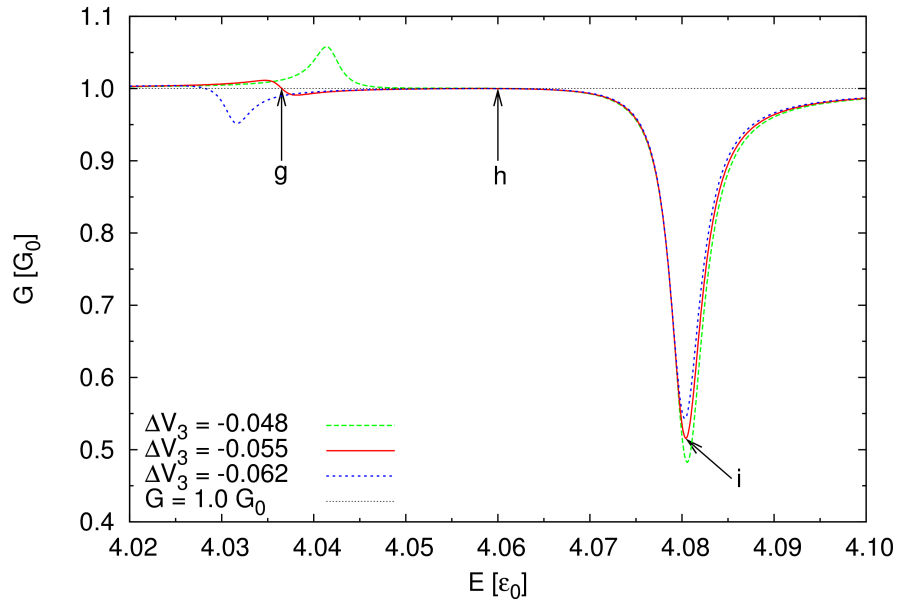

Figure 5.81: Quantum wire with two detuned side-coupled quantum dots. Focus on the crossover from a peak to a dip in the conductance structure around $4\,\varepsilon_0$. The conductance versus energy for positive values of the detuning parameter ΔV_3.

Also, the extended states right of the quantum dots are almost identical for both scattering states. The transmission probabilities for the scattering states at the blip are shown in figure 5.84. Interesting about them is that they are all equal to 0.25.

A concept that is generally not widely known should be introduced before an explanation for the strong quasi-bound states at the blip is given. This is the concept of a bound state in the continuum. In quantum mechanics there are generally two types of solutions of the time-independent Schrödinger equation. Discrete normalizable bound states in the discrete spectrum below the continuum threshold in energy. Furthermore, continuously distributed unnormalizable states in the continuous spectra above the continuum threshold in energy. The scattering states in the quasi-1D Lippmann-Schwinger scattering formalism are an example of continuously distributed states. Above the continuum threshold quasi-bound states can exist, they have finite lifetimes and finite resonance widths. Such quasi-bound states have repeatedly been seen in this thesis. Also, so called bound states in the continuum (BIC) can exist in special cases [38–41]. These states are discrete normalizable bound states above the continuum threshold in energy. They have infinite lifetimes and thus vanishing resonance widths. The one-dimensional potential in figure 5.2 gives a simple picture of all these concepts.

The existence of these bound states in the continuum was first showed by von Neumann and Wigner in 1929 for special but unphysical one-dimensional spatially oscillating attractive potentials [38, 39]. There, the existence of these states is due

to diffractive interference. They were later shown to exist in physically plausible atomic systems [40]. Furthermore, these peculiar states have indeed been observed in superlattice heterostructures grown by molecular-beam epitaxy [42]. Closer to the case at hand bound states in the continuum have been shown to exist in quantum waveguides or similar mesoscopic systems [41,43–45]. In addition, they have very recently been shown to exist, outside of quantum mechanics, in photonic systems [46]. It seems that bound states in the continuum are a general wave phenomena that is not confined to quantum mechanics.

Friedrich and Wintgen used Feshbach's approach to formulate a general model which explains the mechanism behind bound states in the continuum in multichannel scattering [47]. Their main result is that a bound state in the continuum can occur when there are two resonance states corresponding to two different closed channels which interfere with each other. The separation of these two resonance states is varied as a function of a continuous parameter. An avoided crossing of the two resonance states is caused by the interference between these two resonance states. Furthermore, for a certain value of the continuous parameters the interference may result in a vanishing resonance width of one of the resonance states. Thus, a bound state in the continuum is formed. The condition for a bound state in the continuum may not be satisfied exactly. Then the resonance width of one of the resonance states becomes anomalously narrow for a finite range of the continuous separation parameter. They also showed that the bound state in the continuum lies near to the avoided crossing if the widths of the non-interfering resonance states are of the same order. However, it may lie far from the avoided crossing if the widths are very dissimilar. Finally, they state that occurrence of bound states in the continuum and anomalously narrow resonance widths due to this mechanism is a very general effect that may be important in many areas of physics where interference or interaction between resonances may occur.

From the above discussion and the fact that channels in multichannel scattering correspond to the subbands in quasi-one-dimensional scattering the following conclusion can be drawn. That the strong quasi-bound state at the blip is showing an indication of an existence of a bound state in the continuum in a quantum wire with two detuned side-coupled quantum dots. The two resonance states are the quasi-bound states in the two side-coupled quantum dots and the continuous separation parameter is the detuning parameter. The two quasi-bound states are moved closer together by varying the detuning parameter towards zero. The interference between the quasi-bound states results in the avoided crossing seen in figure 5.69. Near the crossover from a peak to a dip a bound state in the continuum is formed for a certain value of the detuning parameters. This happens both for a negative and a positive value of the detuning parameter as seen above. It should be emphasized that the strong quasi-bound state at the blip is not the bound state in the continuum itself, only an indication of its existence.

It is an open question if a bound state in the continuum can be found with the quasi-1D Lippmann-Schwinger scattering formalism. The scattering formalism is

based on the unnormalizable scattering states in the wire. They have the boundary condition of electrons incident from the left which get scattered inside the scattering area. However, the normalizable bound state in the continuum has the boundary condition of begin localized inside the scattering area with a decay into the leads. If the quasi-1D Lippmann-Schwinger scattering formalism allows bound state in the continuum there are nevertheless some problems. Trying to find a resonance state with a vanishing width is a numerically hard problem. However, the resonance state would probably, due to finite accuracy, acquire a finite width in numerical calculations. Also, the search for a bound state in the continuum is in a two-dimensional domain, it has a position in energy and detuning parameter space. Finally the following has been noted in the literature regarding this question. That the scattering wavefunction should diverge in the interior of the spatial structures inducing the resonance states, which here are the side-coupled quantum dots, when approaching the position of the bound state in the continuum [41].

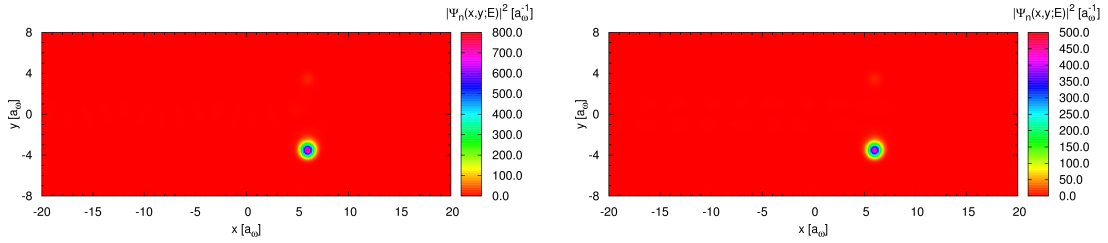

(a) $n = 0$ (b) $n = 1$

Figure 5.82: Quantum wire with two detuned side-coupled quantum dots. The detuning parameter is $\Delta V_3 = -0.055\,\varepsilon_0$. The probability densities of the scattering states at $E = 4.0365\,\varepsilon_0$ marked by $\boldsymbol{g}$ in figure 5.81.

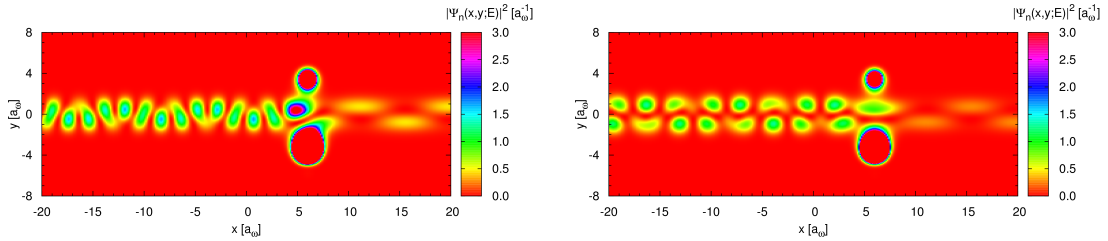

(a) $n = 0$ (b) $n = 1$

Figure 5.83: Quantum wire with two detuned side-coupled quantum dots. The detuning parameter is $\Delta V_3 = -0.055\,\varepsilon_0$. The probability densities of the scattering states at $E = 4.0365\,\varepsilon_0$ marked by $\boldsymbol{g}$ in figure 5.81. The color scale has been shortened considerably to make the extended state in the wire visible.

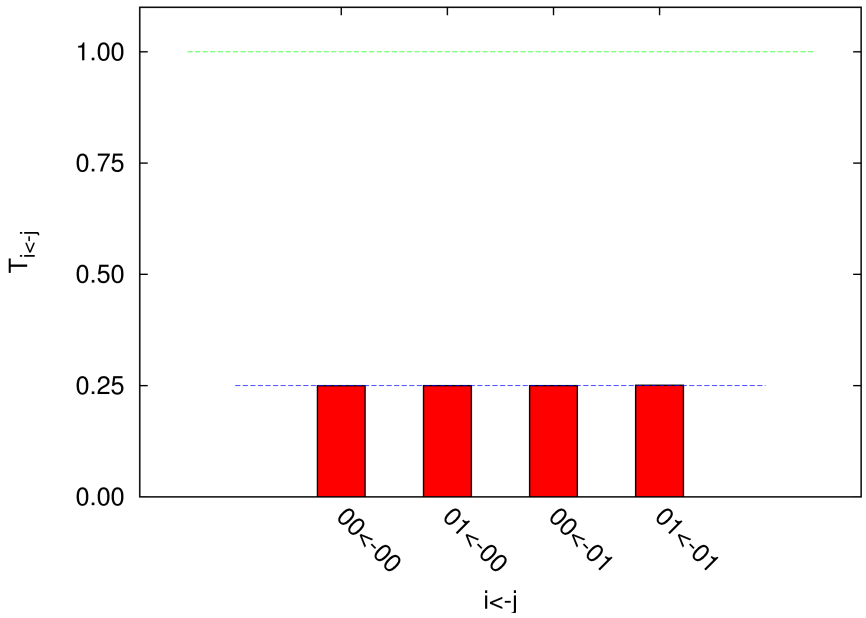

Figure 5.84: Quantum wire with two detuned side-coupled quantum dots. The detuning parameter is $\Delta V_3 = -0.055\,\varepsilon_0$. The transmission probabilities for the scattering states at $E = 4.0365\,\varepsilon_0$ marked by $\boldsymbol{g}$ in figure 5.84.

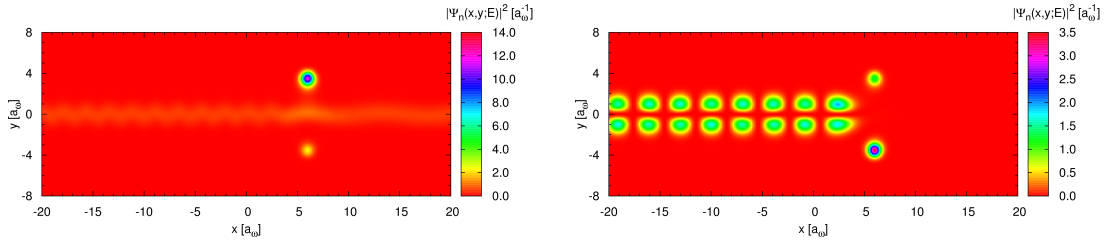

(a) $n = 0$ (b) $n = 1$

Figure 5.85: Quantum wire with two detuned side-coupled quantum dots. The detuning parameter is $\Delta V_3 = -0.055\,\varepsilon_0$. The probability densities of the scattering states at $E = 4.0600\,\varepsilon_0$ marked by ***h*** in figure 5.81.

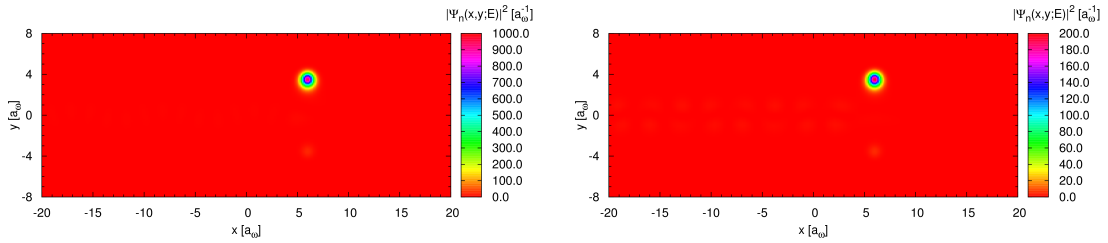

(a) $n = 0$ (b) $n = 1$

Figure 5.86: Quantum wire with two detuned side-coupled quantum dots. The detuning parameter is $\Delta V_3 = -0.055\,\varepsilon_0$. The probability densities of the scattering states at $E = 4.0804\,\varepsilon_0$ marked by ***i*** in figure 5.81.

Chapter 6

Summary

Here, coherent electronic transport through quantum wires with embedded nanostructures has been investigated. The investigation was in a static single-particle picture where a theoretical framework consisting of the Landauer-Büttiker formalism and a quasi-1D Lippmann-Schwinger scattering formalism was used. A clean ballistic quantum wire exhibits step like quantization of the conductance. However, the embedded nanostructures modifies the conductance of the quantum wire system from this quantization.

The systems investigated are mainly of two types. On one hand a quantum wire with a single side-coupled quantum, with and without a step in the wire. The step can be thought of as a part of a model of a partial gate on top of the wire. On the other hand a quantum wire with two side-coupled quantum dots where the dots are both identical and detuned.

A simple model of a closed quantum dot with a similar geometry as the side-coupled quantum dots is also introduced. This model is used to characterize the quasi-bound states in the open side-coupled quantum dots.

The conductance versus energy shows a rich structure for all systems. This conductance structure is mainly caused by quasi-bound states in the quantum dots. The lowest conductance structure in all the system is a sharp and narrow resonance peak-dip pair which shows a symmetric Fano lineshape. The probability densites of the scattering states at this peak-dip pair show a clear sign of the Fano effect, that this resonance peak-dip pair is due to the lowest quasi-bound states in the quantum dots. Tunneling between the bottom of the wire and the quantum dots is also visible there. The Fano effect has indeed been observed in a similar experimental system with a single side-coupled quantum dot [30].

The conductance structure at higher energies is less pronounced and the probability densities of the scattering states are harder to characterize. However, the scattering states show indications of structures around the quantum dots which look like the eigenstates of the closed quantum dot.

The asymmetrical system of a single quantum dot shows asymmetrical scattering and strong band-mixing, as expected. The scattering shows an interesting wriggle

structure which probably could be expected for the case of a classical particle traveling along the x-direction.

The inclusion of a step in a quantum wire with a single quantum dot introduces fine structure in the conductance, it is regularly spaced and mainly in the form of narrow dips. This fine structure is due to quasi-bound states in an effective well defined by the step and the quantum dot. The well acts as an resonator resulting in resonance dips or peaks when the corresponding half-wavelengths satisfy the effective x-length of the well. Otherwise, the conductance is very similar to the case without a step. It can thus be concluded as a first approximation that the conductance of a quantum wire with a single side-coupled quantum dot is for most parts unaltered if a partial gate is introduced in the wire.

The conductance for a quantum wire with two identical side-coupled quantum dots is generally less than for a single quantum dot. Otherwise, the conductance structure is similar to the one for a single quantum dot. For identical quantum dots the lowest resonance peak-dip pair shows quasi-bound states in both quantum dots. Many of the scattering states for two quantum dots are, if the symmetry is ignored, similar to the corresponding scattering states for a single quantum dot. The geometry of two quantum dots introduces a new quasi-bound state which is due to an effective well between the two quantum dots in the y-direction. The scattering for two quantum dot shows an interesting structure that can not be characterized by a motion of a single classical particle but looks rather like pressure fluctuations in a classical fluid or gas flowing along the wire.

The two quantum dots are detuned by varying a detuning parameter which controls the depth of one of the quantum dots compared to the other one. The value of the detuning parameter is in a narrow range so the detuning only has an effect on the lowest resonance peak-dip pair.

The peak or the dip moves when the detuning parameter is varied from zero and both the peak and the dip become less pronounced. The peak crosses over to a dip which becomes deeper, resulting in two dips. An avoided crossing of the peak and dip is seen when the detuning parameter is varied towards zero.

The scattering states when the peak has crossed over to a dip show that the detuning separates the quasi-bound states in the quantum dots. The two different dips correspond to quasi-bound states in two different quantum dots. However, a scattering state betwen the dips shows no quasi-bound state. There are thus three active states in a short energy range, neither dot active or either one of the dots active. This could have an interesting application in a device based on a quantum wire with two detuned quantum dots. The active state could be selected by varying the Fermi energy of electrons in the short energy range around the two dips. This also gives an indication that the quantum dots have to be close to identical to get quasi-bound states in both quantum dots at the same time, leaving little room for variations in manufacturing.

At the crossover from a peak to a dip there is only one dip visible and only a small blip where the peak was before. A strong quasi-bound state at the blip gives

an indication of an interesting and peculiar state in the quantum wire system. So called bound state in the continuum. These states are discrete normalizable bound states lying above the continuum threshold in energy. They have infinite lifetimes and thus vanishing resonance widths. These state are due to interference between two resonance states where the separation between them can be varied as function of a continuous parameter. It should be noted that due to finite accuracy in real structure a bound state in the continuum would most likely be a quasi-bound state with an extremely long lifetime and an extremely narrow width.

Appendix A

The Green's Function

The Green's function $G_m^{\mathrm{s}}(x,x';E)$ that takes the step into consideration is here derived by solving directly the Green's function differential equation. A similar Green's function with a step on the other side, i.e. for $x>0$ not for $x<0$ as here, has been derived in the literature where the spectral representation was used [21,22].

The Green's function fulfills

$$\left[\frac{d^2}{dx^2}+k_{R;m}^2-U_{\mathrm{s}}(x)\right]G_m^{\mathrm{s}}(x,x';E)=\delta(x-x'), \tag{A.1}$$

with the boundary condition of an outgoing wave from x'. The step is given by the potential

$$U_{\mathrm{s}}(x)=U_{\mathrm{s}}\big[1-\Theta(x)\big]=\begin{cases}U_{\mathrm{s}}, & x<0,\\ 0, & x>0,\end{cases} \tag{A.2}$$

where

$$U_{\mathrm{s}}=\frac{2mV_{\mathrm{s}}}{\hbar^2}. \tag{A.3}$$

The wavenumbers for the left and right leads are defined as

$$k_{L,m}^2=k_{R,m}^2-U_{\mathrm{s}}=\frac{2m(E-\varepsilon_m-V_{\mathrm{s}})}{\hbar^2}, \tag{A.4}$$

and

$$k_{R,m}^2=\frac{2m(E-\varepsilon_m)}{\hbar^2}. \tag{A.5}$$

The differential equation is solved by using a similar method as often used when solving one-dimensional scattering problems [10]. A general solution of the Green's function is put forward on each region and the boundary conditions at the perimeters of the regions are used to get the appropriate solution.

The Green's function fulfills

$$\left[\frac{d^2}{dx^2}+k_{L;m}^2\right]G_m^{\mathrm{s}}(x,x';E)=\delta(x-x'), \tag{A.6}$$

for the left lead, i.e. $x < 0$, and

$$\left[\frac{d^2}{dx^2} + k_{R;m}^2\right] G_m^{\mathrm{s}}(x, x'; E) = \delta(x - x'), \tag{A.7}$$

for the right lead, i.e. $x > 0$.

The second derivative of the Green's function is infinite at $x = x'$. Thus, a similar trick as used when the scattering problem of the delta function is solved is used to obtain the boundary condition [10]. The above differential equations are integrated from $x - \epsilon$ to $x + \epsilon$. Here, $\epsilon > 0$ is small constant which is taken to the limit $\epsilon \to 0$ after integrating. This results in

$$\int_{x-\epsilon}^{x+\epsilon} dx\, \frac{d^2}{dx^2} G_m^{\mathrm{s}}(x, x'; E) + \int_{x-\epsilon}^{x+\epsilon} dx\, k_{\{L,R\};m}^2 G_m^{\mathrm{s}}(x, x'; E) = \int_{x-\epsilon}^{x+\epsilon} dx\, \delta(x - x'). \tag{A.8}$$

The second term on the left side is zero in the limit $\epsilon \to 0$ and the first term on the left side is the derivative of the Green's function taken at the integration limits. Thus, taking the limit $\epsilon \to 0$ the left side is

$$\begin{aligned} \Delta\Big(\frac{d}{dx} G_m^{\mathrm{s}}(x, x'; E)\Big) &= \frac{d}{dx} G_m^{\mathrm{s}}(x^+, x'; E) - \frac{d}{dx} G_m^{\mathrm{s}}(x^-, x'; E) \\ &= \lim_{\epsilon \to 0} \Big(\frac{d}{dx} G_m^{\mathrm{s}}(x + \epsilon, x'; E) - \frac{d}{dx} G_m^{\mathrm{s}}(x - \epsilon, x'; E)\Big). \end{aligned} \tag{A.9}$$

The term on the right side, i.e the integral over the delta function, depends on if x' is in the range $[x - \epsilon, x + \epsilon]$ or not

$$\int_{x-\epsilon}^{x+\epsilon} dx\, \delta(x - x') = \begin{cases} 1, & x' \in [x - \epsilon, x + \epsilon], \\ 0, & x' \notin [x - \epsilon, x + \epsilon]. \end{cases} \tag{A.10}$$

The boundary condition at $x = x'$ is obtained by taking the limit $\epsilon \to 0$

$$\Delta\Big(\frac{d}{dx} G_m^{\mathrm{s}}(x, x'; E)\Big) = \begin{cases} 1, & x' = x, \\ 0, & x' \neq x. \end{cases} \tag{A.11}$$

Thus, there is a discontinuity in the derivative of the Green's function at $x = x'$. It can be seen that the Green's function itself is continuous by integrating again

$$\Delta\Big(G_m^{\mathrm{s}}(x, x'; E)\Big) = 0. \tag{A.12}$$

The case $x' > 0$ is first considered. The general solution for the Green's function is

$$G_m^{\mathrm{s}}(x, x'; E) = \begin{cases} Ae^{ik_{L;m}x} + Be^{-ik_{L;m}x}, & x < 0, \\ Ce^{ik_{R;m}x} + De^{-ik_{R;m}x}, & x > 0 \ \& \ x < x', \\ Ee^{ik_{R;m}x} + Fe^{-ik_{R;m}x}, & x > 0 \ \& \ x > x'. \end{cases} \tag{A.13}$$

The boundary condition of an outgoing wave from x' gives $A = F = 0$. Furthermore, the other boundary conditions at $x = 0$ and $x = x'$ give the following linear equations for the remaining coefficients

$$B = C + D, \tag{A.14}$$

$$-ik_{L;m}B = ik_{R;m}C - ik_{R;m}D, \tag{A.15}$$

$$Ce^{ik_{R;m}x'} + De^{-ik_{R;m}x'} = Ee^{ik_{R;m}x'}, \tag{A.16}$$

$$ik_{R;m}Ee^{ik_{R;m}x'} - ik_{R;m}Ce^{ik_{R;m}x'} + ik_{R;m}De^{-ik_{R;m}x'} = 1. \tag{A.17}$$

These linear equations have the solution

$$B = -\frac{i}{k_{R;m} + k_{L;m}} e^{ik_{R;m}x'}, \tag{A.18}$$

$$C = -\frac{i}{2k_{R;m}} \Big(\frac{k_{R;m} - k_{L;m}}{k_{R;m} + k_{L;m}} \Big) e^{ik_{R;m}x'}, \tag{A.19}$$

$$D = -\frac{i}{2k_{R;m}} e^{ik_{R;m}x'}, \tag{A.20}$$

$$E = -\frac{i}{2k_{R;m}} e^{-ik_{R;m}x'} - \frac{i}{2k_{R;m}} \Big(\frac{k_{R;m} - k_{L;m}}{k_{R;m} + k_{L;m}} \Big) e^{ik_{R;m}x'}. \tag{A.21}$$

Thus, the Green's function for $x' > 0$ is

$$G_m^{\mathrm{s}}(x, x'; E) = \begin{cases} -\frac{i}{k_{R;m}+k_{L;m}} e^{-ik_{L;m}x + ik_{R;m}x'}, & x < 0, \\ -\frac{i}{2k_{R;m}} e^{-ik_{R;m}(x-x')} & \\ -\frac{i}{2k_{R;m}} \Big(\frac{k_{R;m}-k_{L;m}}{k_{R;m}+k_{L;m}} \Big) e^{ik_{R;m}(x+x')}, & x > 0 \ \& \ x < x', \\ -\frac{i}{2k_{R;m}} e^{ik_{R;m}(x-x')} & \\ -\frac{i}{2k_{R;m}} \Big(\frac{k_{R;m}-k_{L;m}}{k_{R;m}+k_{L;m}} \Big) e^{ik_{R;m}(x+x')}, & x > 0 \ \& \ x > x'. \end{cases} \tag{A.22}$$

The case $x' < 0$ is then considered. The general solution is

$$G_m^{\mathrm{s}}(x, x'; E) = \begin{cases} Ge^{ik_{L;m}x} + He^{-ik_{L;m}x}, & x < 0 \ \& \ x < x', \\ Ie^{ik_{L;m}x} + Je^{-ik_{L;m}x}, & x < 0 \ \& \ x > x', \\ Ke^{ik_{R;m}x} + Le^{-ik_{R;m}x}, & x > 0. \end{cases} \tag{A.23}$$

The boundary condition of a outgoing wave from x' gives $G = L = 0$. Furthermore, the other boundary conditions at $x = 0$ and $x = x'$ give the following linear equations for the remaining coefficients

$$He^{-ik_{L;m}x'} = Ie^{ik_{L;m}x'} + Je^{-ik_{L;m}x'}, \tag{A.24}$$
$$ik_{L;m}Ie^{ik_{L;m}x'} - ik_{L;m}Je^{-ik_{L;m}x'} + ik_{L;m}He^{-ik_{L;m}x'} = 1, \tag{A.25}$$
$$I + J = K, \tag{A.26}$$
$$ik_{L;m}I - ik_{L;m}J = ik_{R;m}K. \tag{A.27}$$

These linear equations have the solution

$$H = -\frac{i}{2k_{L;m}}e^{ik_{L;m}x'} + \frac{i}{2k_{L;m}}\Big(\frac{k_{R;m} - k_{L;m}}{k_{R;m} + k_{L;m}}\Big)e^{-ik_{L;m}x'}, \tag{A.28}$$
$$I = -\frac{i}{2k_{L;m}}e^{-ik_{L;m}x'}, \tag{A.29}$$
$$J = +\frac{i}{2k_{L;m}}\Big(\frac{k_{R;m} - k_{L;m}}{k_{R;m} + k_{L;m}}\Big)e^{-ik_{L;m}x'}, \tag{A.30}$$
$$K = -\frac{i}{k_{R;m} + k_{L;m}}e^{-ik_{L;m}x'}. \tag{A.31}$$

Thus, the Green's function for $x' < 0$ is

$$G^{\mathrm{s}}_m(x, x'; E) = \begin{cases} -\frac{i}{2k_{L;m}}e^{-ik_{L;m}(x-x')} \\ +\frac{i}{2k_{L;m}}\left(\frac{k_{R;m}-k_{L;m}}{k_{R;m}+k_{L;m}}\right)e^{-ik_{L;m}(x+x')}, & x < 0 \ \& \ x < x', \\ \\ -\frac{i}{2k_{L;m}}e^{ik_{L;m}(x-x')} \\ +\frac{i}{2k_{L;m}}\left(\frac{k_{R;m}-k_{L;m}}{k_{R;m}+k_{L;m}}\right)e^{-ik_{L;m}(x+x')}, & x < 0 \ \& \ x > x', \\ \\ -\frac{i}{k_{R;m}+k_{L;m}}e^{ik_{R;m}x - ik_{L;m}x'}, & x > 0. \end{cases} \tag{A.32}$$

The absolute value is defined as

$$|x - x'| = \begin{cases} (x - x'), & x - x' > 0, \\ -(x - x'), & x - x' < 0. \end{cases} \tag{A.33}$$

Thus, the Green's function can be written as

$$G_m^{\mathrm{s}}(x,x';E)=\begin{cases}-\frac{i}{2k_{L;m}}e^{ik_{L;m}|x-x'|}\\ +\frac{i}{2k_{L;m}}\left(\frac{k_{R;m}-k_{L;m}}{k_{R;m}+k_{L;m}}\right)e^{-ik_{L;m}(x+x')}, & x<0\ \&\ x'<0,\\ -\frac{i}{k_{R;m}+k_{L;m}}e^{-ik_{L;m}x+ik_{R;m}x'}, & x<0\ \&\ x'>0,\\ -\frac{i}{k_{R;m}+k_{L;m}}e^{ik_{R;m}x-ik_{L;m}x'}, & x>0\ \&\ x'<0,\\ -\frac{i}{2k_{R;m}}e^{ik_{R;m}|x-x'|}\\ -\frac{i}{2k_{R;m}}\left(\frac{k_{R;m}-k_{L;m}}{k_{R;m}+k_{L;m}}\right)e^{ik_{R;m}(x+x')}, & x>0\ \&\ x'>0.\end{cases}\tag{A.34}$$

The limiting case of no step, $V_0\to 0$, can be considered. Then

$$k_{R;m}=k_{L;m}=k_m,\tag{A.35}$$

so the Green's function is

$$\lim_{V_0\to 0}G_m^{\mathrm{s}}(x,x';E)=-\frac{i}{2k_m}e^{ik_m|x-x'|},\tag{A.36}$$

which is the Green's function for a free particle, as expected.

The transmission and reflection amplitudes can be defined

$$t_m=\frac{2k_{R;m}}{k_{R;m}+k_{L;m}},\qquad r_m=\frac{k_{R;m}-k_{L;m}}{k_{R;m}+k_{L;m}}.\tag{A.37}$$

The Green's function can then be written as

$$G_m^{\mathrm{s}}(x,x';E)=\begin{cases}-\frac{i}{2k_{L;m}}e^{ik_{L;m}|x-x'|}\\ +\frac{i}{2k_{L;m}}r_m e^{-ik_{L;m}(x+x')}, & x<0\ \&\ x'<0,\\ -\frac{i}{2k_{R;m}}t_m e^{-ik_{L;m}x+ik_{R;m}x'}, & x<0\ \&\ x'>0,\\ -\frac{i}{2k_{R;m}}t_m e^{ik_{R;m}x-ik_{L;m}x'}, & x>0\ \&\ x'<0,\\ -\frac{i}{2k_{R;m}}e^{ik_{R;m}|x-x'|}\\ -\frac{i}{2k_{R;m}}r_m e^{ik_{R;m}(x+x')}, & x>0\ \&\ x'>0.\end{cases}\tag{A.38}$$

This form shows a very simple interpretation of the Green's function as a propagator from x' to x. For $x<0$ and $x'<0$ the first term can be interpreted as the direct path from x' to x and the second term as the path which propagates from x' to the step at 0 where it gets reflected and then propagates to x. For $x>0$ and $x'<0$ the single term can be interpreted as the path which propagates from x' to the step at 0 where it gets transmitted and then propagates to x'. There are similar interpretations for the other two cases.

Appendix B

Matrix Elements for a Gaussian Potential

Here, the matrix elements for a Gaussian potential are derived. The Gaussian potential is given by

$$V_i(x,y) = V_i e^{-[\beta_{x,i}(x-x_i)^2+\beta_{y,i}(y-y_i)^2]}, \tag{B.1}$$

where V_i is the strength of the potential, $(x_i,\ y_i)$ is the center of the potential and $\beta_{\{x,y\},i}$ determine the range of the potential. The matrix elements are

$$V_{i;m,m'}(x) = \int_{-\infty}^{\infty} dy \chi_m^*(y) V_i(x,y) \chi_{m'}(y). \tag{B.2}$$

The wavefunctions of the subbands for a parabolic confinement were introduced in section 2.3

$$\chi_m(y) = \frac{1}{(2^m m! \pi^{1/2} a_\omega)^{1/2}} H_m\left(\frac{y}{a_\omega}\right) e^{-y^2/2a_\omega^2}, \qquad m = 0, 1, 2, \ldots . \tag{B.3}$$

The wavefunctions are real so the matrix elements are invariant under exchange of m and m'

$$V_{i;m,m'}(x) = V_{i;m',m}(x). \tag{B.4}$$

Putting all together results in

$$V_{i;m,m'}(x) = \int_{-\infty}^{\infty} dy \left[\left[\frac{1}{(2^m m! \pi^{1/2} a_\omega)^{1/2}} e^{-y^2/2a_\omega^2} H_m(y/a_\omega) \right] \right.$$
$$\left. \left[V_i e^{-\beta_{x,i}(x-x_i)^2 - \beta_{y,i}(y-y_i)^2} \right] \left[\frac{1}{(2^{m'} m'! \pi^{1/2} a_\omega)^{1/2}} e^{-y^2/2a_\omega^2} H_{m'}(y/a_\omega) \right] \right]. \tag{B.5}$$

The substitution $\tilde{y} = y/a_\omega$ gives

$$V_{i;m,m'}(x) = \frac{V_i e^{-\beta_{x,i}(x-x_i)^2}}{(2^{m+m'}m!m'!\pi)^{1/2}} \int_{-\infty}^{\infty} d\tilde{y}\, e^{-\beta_{y,i}a_\omega^2(\tilde{y}-\tilde{y}_i)^2-\tilde{y}^2} H_m(\tilde{y})H_{m'}(\tilde{y}). \tag{B.6}$$

For convenience the notation $\tilde{\beta}_{y,i} = \beta_{y,i}a_\omega^2$ is defined. The expression in the exponential inside the integral is

$$\begin{aligned}
&-\tilde{\beta}_{y,i}(\tilde{y}-\tilde{y}_i)^2 - \tilde{y}^2 = -\left[(1+\tilde{\beta}_{y,i})\tilde{y}^2 - 2\tilde{\beta}_{y,i}\tilde{y}_i\tilde{y} + \tilde{\beta}_{y,i}\tilde{y}_i^2 - \frac{\tilde{\beta}_{y,i}\tilde{y}_i^2}{1+\tilde{\beta}_{y,i}} + \frac{\tilde{\beta}_{y,i}\tilde{y}_i^2}{1+\tilde{\beta}_{y,i}}\right] \\
&= -\frac{1}{1+\tilde{\beta}_{y,i}}\left[(1+\tilde{\beta}_{y,i})^2\tilde{y}^2 - 2(1+\tilde{\beta}_{y,i})\tilde{\beta}_{y,i}\tilde{y}_i\tilde{y} + (1+\tilde{\beta}_{y,i})\tilde{\beta}_{y,i}\tilde{y}_i^2 - \tilde{\beta}_{y,i}\tilde{y}_i^2 + \tilde{\beta}_{y,i}\tilde{y}_i^2\right] \\
&= -\frac{1}{1+\tilde{\beta}_{y,i}}\left[(1+\tilde{\beta}_{y,i})^2\tilde{y}^2 - 2(1+\tilde{\beta}_{y,i})\tilde{\beta}_{y,i}\tilde{y}_i\tilde{y} + \tilde{\beta}_{y,i}^2\tilde{y}_i^2 + \tilde{\beta}_{y,i}\tilde{y}_i^2\right] \\
&= -\frac{1}{1+\tilde{\beta}_{y,i}}\left[(1+\tilde{\beta}_{y,i})\tilde{y} - \tilde{\beta}_{y,i}\tilde{y}_i\right]^2 - \frac{\tilde{\beta}_{y,i}\tilde{y}_i^2}{1+\tilde{\beta}_{y,i}} \\
&= -\left[(1+\tilde{\beta}_{y,i})^{1/2}\tilde{y} - \frac{\tilde{\beta}_{y,i}\tilde{y}_i}{(1+\tilde{\beta}_{y,i})^{1/2}}\right]^2 - \frac{\tilde{\beta}_{y,i}\tilde{y}_i^2}{1+\tilde{\beta}_{y,i}}.
\end{aligned} \tag{B.7}$$

Using this and the substitution $t = (1+\tilde{\beta}_{y,i})^{1/2}\tilde{y}$ results in

$$\begin{aligned}
V_{i;m,m'}(x) = &\frac{V_i e^{-\beta_{x,i}(x-x_i)^2}}{(2^{m+m'}m!m'!\pi)^{1/2}} \frac{e^{-\frac{\tilde{\beta}_{y,i}\tilde{y}_i^2}{1+\tilde{\beta}_{y,i}}}}{(1+\tilde{\beta}_{y,i})^{1/2}} \\
&\times \int_{-\infty}^{\infty} dt\, e^{-\left(t-\frac{\tilde{\beta}_{y,i}\tilde{y}_i}{(1+\tilde{\beta}_{y,i})^{1/2}}\right)^2} H_m\left[\frac{t}{(1+\tilde{\beta}_{y,i})^{1/2}}\right] H_{m'}\left[\frac{t}{(1+\tilde{\beta}_{y,i})^{1/2}}\right].
\end{aligned} \tag{B.8}$$

Equation 7.374.9 on page 797 in [48] gives

$$\begin{aligned}
&\int_{-\infty}^{\infty} dx\, e^{-(x-y)^2} H_m(\alpha x)H_n(\alpha x) \\
&\quad = \pi^{1/2} \sum_{k=0}^{\min(m,n)} 2^k k! \binom{m}{k}\binom{n}{k} (1-\alpha^2)^{\frac{m+n}{2}-k} H_{m+n-2k}\left[\frac{\alpha y}{(1-\alpha^2)^{1/2}}\right].
\end{aligned} \tag{B.9}$$

Thus

$$\begin{aligned}
V_{i;m,m'}(x) = &\frac{V_i e^{-\beta_{x,i}(x-x_i)^2}}{(2^{m+m'}m!m'!)^{1/2}} \frac{e^{-\frac{\tilde{\beta}_{y,i}\tilde{y}_i^2}{1+\tilde{\beta}_{y,i}}}}{(1+\tilde{\beta}_{y,i})^{1/2}} \\
&\times \sum_{k=0}^{\min(m,m')} 2^k k! \binom{m}{k}\binom{m'}{k} \left(\frac{\tilde{\beta}_{y,i}}{1+\tilde{\beta}_{y,i}}\right)^{\frac{m+m'}{2}-k} H_{m+m'-2k}\left[\frac{\tilde{\beta}_{y,i}^{1/2}\tilde{y}_i}{(1+\tilde{\beta}_{y,i})^{1/2}}\right].
\end{aligned} \tag{B.10}$$

The final answer is

$$V_{i;m,m'}(x) = \frac{V_i e^{-\beta_{x,i}(x-x_i)^2}}{(2^{m+m'}m!m'!)^{1/2}} \frac{e^{-\frac{\beta_{y,i}y_i^2}{1+\beta_{y,i}a_\omega^2}}}{(1+\beta_{y,i}a_\omega^2)^{1/2}}$$
$$\times \sum_{k=0}^{\min(m,m')} 2^k k! \binom{m}{k}\binom{m'}{k}\left(\frac{\beta_{y,i}a_\omega^2}{1+\beta_{y,i}a_\omega^2}\right)^{\frac{m+m'}{2}-k} H_{m+m'-2k}\left[\frac{\beta_{y,i}^{1/2}y_i}{(1+\beta_{y,i}a_\omega^2)^{1/2}}\right], \tag{B.11}$$

where the original parameters have been restored. Also, if the scaled variables defined in section 3.4 are used

$$\hat{V}_{i;m,m'}(\hat{x}) = \frac{\hat{V}_i e^{-\hat{\beta}_{x,i}(\hat{x}-\hat{x}_i)^2}}{(2^{m+m'}m!m'!)^{1/2}} \frac{e^{-\frac{\hat{\beta}_{\hat{y},i}\hat{y}_i^2}{1+\hat{\beta}_{y,i}}}}{(1+\hat{\beta}_{y,i})^{1/2}}$$
$$\times \sum_{k=0}^{\min(m,m')} 2^k k! \binom{m}{k}\binom{m'}{k}\left(\frac{\hat{\beta}_{y,i}}{1+\hat{\beta}_{y,i}}\right)^{\frac{m+m'}{2}-k} H_{m+m'-2k}\left[\frac{\hat{\beta}_{y,i}^{1/2}\hat{y}_i}{(1+\hat{\beta}_{y,i})^{1/2}}\right]. \tag{B.12}$$

Appendix C

Numerical Methods

Here, the numerical methods used to solve the equations of the quasi-1D Lippmann-Schwinger scattering formalism are introduced. It should be noted that every equation and variable is scaled and dimensionless as defined in section 3.4 although it is not explicitly labeled.

The coupled Lippmann-Schwinger equations are

$$\varphi_{n;m}(x;E) = \varphi^0_{n;m}(x) + \sum_{m'} \int_{-\infty}^{\infty} dx' \underbrace{G^s_m(x,x';E)V_{m,m'}(x')}_{=K_{m,m'}(x,x';E)} \varphi_{n;m'}(x'). \tag{C.1}$$

The total number of subband used in the calculations is N_m. Thus, for a parabolic confinement the highest subband is subband $N_m - 1$.

The Green's function has a cusp at $x = x'$ caused by the $e^{ik_m|x-x'|}$ term. This must be taken care of in the integral in the Lippmann-Schwinger equations. Thus, the integral is split into two intervals, for $x' < x$ and $x' > x$. The cusp is then at the ends of the intervals integrated over.

The scattering potential is localized so

$$\lim_{x\to\pm\infty} V_{m,m'}(x) = 0. \tag{C.2}$$

The infinite limits in the integral are thus approximated with a finite cutoff $\pm x_{\max}$ where $V_{m,m'}(\pm x_{\max}) \approx 0$. The integral is then

$$\int_{-\infty}^{\infty} dx' \approx \int_{-x_{\max}}^{x} dx' + \int_{x}^{x_{\max}} dx'. \tag{C.3}$$

The numerical integration scheme used to solve the integrals in the Lippmann-Schwinger equations is the five point Bode's rule [29]

$$\int_{x_1}^{x_5} dx f(x) = \frac{2h}{45}\left(7f_1 + 32f_2 + 12f_3 + 32f_4 + 7f_5\right) - \frac{8f^{(6)}(\xi)h^7}{945}, \tag{C.4}$$

where $h = x_{i+1} - x_i$ is the spacing between points and $f_i = f(x_i)$. An extended version of this rule for $N = 4n + 1 = 5, 9, 13, 17, 21, \ldots$ points is

$$\begin{aligned}\int_{x_1}^{x_N} dx f(x) \approx & \frac{2h}{45}\big(7f_1 + 32f_2 + 12f_3 + 32f_4 + 14f_5 + 32f_6 + 12f_7 \\ & + \ldots + 32f_{N-5} + 14f_{N-4} + 32f_{N-3} + 12f_{N-2} + 32f_{N-1} + 7f_N\big) \\ = & \frac{2h}{45}\left(7f_1 + 32\sum_{k=1}^{(N-1)/2} f_{2k} + 12\sum_{i=k}^{(N-1)/4} f_{4k-1} + 14\sum_{k=1}^{(N-5)/4} f_{4k+1} + 7f_N\right), \qquad \text{(C.5)}\end{aligned}$$

where $h = (x_N - x_1)/(N-1)$ and $x_i = x_1 + (i-1)h$.

First, x is put on an equally spaced grid, $x_1, x_2, \ldots, x_{N_x}$, from $-x_{\max}$ to $x_{\max}$ with a total of $N_x = 4n_x + 1$ grid points. Then

$$h = \frac{2x_{\max}}{N_x - 1}, \qquad \text{(C.6)}$$

and

$$x_i = -x_{\max} + (i-1)h. \qquad \text{(C.7)}$$

The Lippmann-Schwinger equations are now

$$\begin{aligned}\varphi_{n;m}(x_i) = \varphi^0_{n;m}(x_i) + \sum_{m'=0}^{N_m-1}\Bigg[& \int_{x_1}^{x_i} dx'\, K_{m,m'}(x_i, x')\varphi_{n;m'}(x') \\ & + \int_{x_i}^{x_{N_x}} dx' K_{m,m'}(x_i, x')\varphi_{n;m'}(x')\Bigg]. \qquad \text{(C.8)}\end{aligned}$$

The extended Bode's rule is only for $N = 4n + 1 = 5, 9, 13, \ldots$ points. Thus, it will depend on the value of i which limits are used for the integrals. This is to make sure there are appropriate numbers of grid points for the two intervals. The case for $i = 3, 7, 11, 15, \ldots, (N_x - 2)$ will be looked at as a specific example. The limits are then

$$\begin{aligned}\varphi_{n;m}(x_i) = \varphi^0_{n;m}(x_i) + \sum_{m'=0}^{N_m-1}\Bigg[& \int_{x_3}^{x_i} dx' K_{m,m'}(x_i, x')\varphi_{n;m'}(x') \\ & + \int_{x_i}^{x_{N_x-2}} dx' K_{m,m'}(x_i, x')\varphi_{n;m'}(x')\Bigg]. \qquad \text{(C.9)}\end{aligned}$$

Then, Bode's rule gives

$$\begin{aligned}
\varphi_{n;m}(x_i) &= \varphi^0_{n;m}(x_i) \\
&+ \sum_{m'=0}^{N_m-1} \Bigg[\frac{2h}{45} \Bigg(7K_{m,m'}(x_i, x_3)\varphi_{n;m'}(x_3) + 32 \sum_{k=1}^{(i-3)/2} K_{m,m'}(x_i, x_{2k+2})\varphi_{n;m'}(x_{2k+2}) \\
&+ 12 \sum_{k=1}^{(i-3)/4} K_{m,m'}(x_i, x_{4k+1})\varphi_{n;m'}(x_{4k+1}) + 14 \sum_{k=1}^{(i-7)/4} K_{m,m'}(x_i, x_{4k+3})\varphi_{n;m'}(x_{4k+3}) \\
&+ 7K_{m,m'}(x_i, x_i)\varphi_{n;m'}(x_i) \Bigg) \\
&+ \frac{2h}{45} \Bigg(7K_{m,m'}(x_i, x_i)\varphi_{n;m'}(x_3) + 32 \sum_{k=(i-1)/2}^{(N_x-7)/2} K_{m,m'}(x_i, x_{2k+2})\varphi_{n;m'}(x_{2k+2}) \\
&+ 12 \sum_{k=(i+1)/4}^{(N_x-5)/4} K_{m,m'}(x_i, x_{4k+1})\varphi_{n;m'}(x_{4k+1}) + 14 \sum_{k=(i+1)/4}^{(N_x-9)/4} K_{m,m'}(x_i, x_{4k+3})\varphi_{n;m'}(x_{4k+3}) \\
&+ 7K_{m,m'}(x_i, x_{N_x-2})\varphi_{n;m'}(x_{N_x-2}) \Bigg) \Bigg] \\
&= \varphi^0_{n;m}(x_i) + \sum_{m'=0}^{N_m-1} \sum_{k=1}^{N_x} \frac{2h}{45} w_{i,j} K_{m,m'}(x_i, x_j)\varphi_{n;m'}(x_j).
\end{aligned} \tag{C.10}$$

Where, for convince, the weights $w_{i,j}$ have been defined. The weights for all four cases are the following.

- If $i = 4l - 3 = 1, 5, 9, 13, \ldots, N_x, \quad l = 1, 2, \ldots, (N_x + 3)/4$

$$w_{i,j} = \begin{cases} 7 & \text{if} \quad j = 1, N_x, \\ 32 & \text{if} \quad j = 2k, \quad k = 1, \ldots, (N_x - 1)/2, \\ 12 & \text{if} \quad j = 4k - 1, \quad k = 1, \ldots, (N_x - 1)/4, \\ 14 & \text{if} \quad j = 4k + 1, \quad k = 1, \ldots, (N_x - 5)/4. \end{cases} \tag{C.11}$$

- If $i = 4l - 2 = 2, 6, 10, 14, \ldots, N_x - 1, \quad l = 1, 2, \ldots, (N_x + 1)/4$

$$w_{i,j} = \begin{cases} 0 & \text{if} \quad j = 1, N_x - 2, N_x - 1, N_x, \\ 7 & \text{if} \quad j = 2, N_x - 3, \\ 32 & \text{if} \quad j = 2k + 1, \quad k = 1, \ldots, (N_x - 5)/2, \\ 12 & \text{if} \quad j = 4k, \quad k = 1, \ldots, (N_x - 5)/4, \\ 14 & \text{if} \quad j = 4k + 2, \quad k = 1, \ldots, (N_x - 9)/4. \end{cases} \tag{C.12}$$

- If $i = 4l - 1 = 3, 7, 11, 15, \ldots, N_x - 2, \quad l = 1, 2, \ldots, (N_x - 1)/4$

$$w_{i,j} = \begin{cases} 0 & \text{if} \quad j = 1, 2, N_x - 1, N_x, \\ 7 & \text{if} \quad j = 3, N_x - 2, \\ 32 & \text{if} \quad j = 2k + 2, \quad k = 1, \ldots, (N_x - 5)/2, \\ 12 & \text{if} \quad j = 4k + 1, \quad k = 1, \ldots, (N_x - 5)/4, \\ 14 & \text{if} \quad j = 4k + 3, \quad k = 1, \ldots, (N_x - 9)/4. \end{cases} \tag{C.13}$$

- If $i = 4l = 4, 8, 12, 16, \ldots, N_x - 3, \quad l = 1, 2, \ldots, (N_x - 3)/4$

$$w_{i,j} = \begin{cases} 0 & \text{if} \quad j = 1, 2, 3, N_x, \\ 7 & \text{if} \quad j = 4, N_x - 1, \\ 32 & \text{if} \quad j = 2k + 3, \quad k = 1, \ldots, (N_x - 5)/2, \\ 12 & \text{if} \quad j = 4k + 2, \quad k = 1, \ldots, (N_x - 5)/4, \\ 14 & \text{if} \quad j = 4k + 4, \quad k = 1, \ldots, (N_x - 9)/4. \end{cases} \tag{C.14}$$

The following notation is defined

$$\tilde{K}_{m,i;m,j} = \frac{2h}{45} w_{i,j} K_{m,m'}(x_i, x_j), \tag{C.15}$$

and

$$\varphi_{n;m',j} = \varphi_{n;m'}(x_j). \tag{C.16}$$

The Lippmann-Schwinger equations are then

$$\varphi_{n;m,i} = \varphi^0_{n;m,i} + \sum_{m'=0}^{N_m - 1} \sum_{k=1}^{N_x} \tilde{K}_{m,i;m',j} \varphi_{n;m',j}, \tag{C.17}$$

which are inconvenient tensor equations. The mappings $\mu \leftrightarrow (m, i)$ and $\nu \leftrightarrow (m', j)$ are thus defined by

$$\mu = i + mN_x, \quad i = 1, \ldots, N_x, \quad m = 1, \ldots, N_m, \tag{C.18}$$

and

$$\nu = j + m'N_x, \quad j = 1, \ldots, N_x, \quad m' = 1, \ldots, N_m. \tag{C.19}$$

These mappings are also showed in table C.1. The Lippmann-Schwinger equations are then

$$\varphi_{n;\mu} = \varphi^0_{n;\mu} + \sum_{\nu=1}^{N_m \cdot N_x} \tilde{K}_{\mu,\nu} \varphi_{n;\nu}. \tag{C.20}$$

The vectors $\boldsymbol{\varphi}_n$ and $\boldsymbol{\varphi}^0_n$ and the matrix $\tilde{K}$ are defined so the above equations can be written as

$$\boldsymbol{\varphi}_n = \boldsymbol{\varphi}^0_n + \tilde{K} \boldsymbol{\varphi}_n. \tag{C.21}$$

Table C.1: Definition of the mappings $\mu \leftrightarrow (m, i)$ and $\nu \leftrightarrow (m', j)$.

μ/ν	m/m'	i/j
1	0	1
2	0	2
3	0	3
$\vdots$	$\vdots$	$\vdots$
$N_x - 1$	0	$N_x - 1$
N_x	0	N_x
$N_x + 1$	1	1
$N_x + 2$	1	2
$\vdots$	$\vdots$	$\vdots$
$2N_x$	1	N_x
$2N_x + 1$	2	1
$\vdots$	$\vdots$	$\vdots$
$(N_m - 1)N_x$	$N_m - 2$	N_x
$(N_m - 1)N_x + 1$	$N_m - 1$	1
$\vdots$	$\vdots$	$\vdots$
$N_m \cdot N_x$	$N_m - 1$	N_x

This results in

$$(\mathbb{1} - \tilde{K})\boldsymbol{\varphi}_n = \boldsymbol{\varphi}_n^0. \tag{C.22}$$

The matrix $H = \mathbb{1} - \tilde{K}$ is defined

$$H\boldsymbol{\varphi}_n = \boldsymbol{\varphi}_n^0. \tag{C.23}$$

This is a matrix equation where the matrix elements are given by

$$H_{\nu,\mu} = \delta_{\nu,\mu} - \frac{2h}{45} w_{i,j} G_{m;i,j} V_{m,m';j} = \delta_{\nu,\mu} - \frac{2h}{45} w_{i,j} G_m(x_i, x_j) V_{m,m'}(x_j). \tag{C.24}$$

The coupled Lippmann-Schwinger integral equations have thus been transformed into a matrix equation which is simple to solve.

The transmission amplitudes $t_{m,n}$ are given by the equation

$$t_{m,n} = \delta_{m,n} \frac{2k_{L;n}}{k_{L;n} + k_{R;n}} + \sum_{m'} \int_{-\infty}^{\infty} dx' \underbrace{g_m(x') V_{m,m'}(x')}_{s_{m,m'}(x')} \varphi_{n;m'}(x'). \tag{C.25}$$

Using Bode's rule results in

$$\begin{aligned} t_{m,n} &= \delta_{m,n}\frac{2k_{L;n}}{k_{L;n}+k_{R;n}} + \sum_{m'=0}^{N_m}\sum_{j=1}^{N_x}\frac{2h}{45}l_j s_{m,m'}(x_j)\varphi_{n;m'}(x_j) \\ &= \delta_{m,n}\frac{2k_{L;n}}{k_{L;n}+k_{R;n}} + \sum_{m'=0}^{N_m}\sum_{j=1}^{N_x}\frac{2h}{45}l_j s_{m;m',j}\varphi_{n;m',j}, \end{aligned} \tag{C.26}$$

where the integral weights are defined by

$$l_j = \begin{cases} 7 & \text{if} \quad j = 1, N_x, \\ 32 & \text{if} \quad j = 2k, \quad k = 1, \ldots, (N_x-1)/2, \\ 12 & \text{if} \quad j = 4k-1, \quad k = 1, \ldots, (N_x-1)/4, \\ 14 & \text{if} \quad j = 4k+1, \quad k = 1, \ldots, (N_x-5)/4. \end{cases} \tag{C.27}$$

Putting $h_{m;m',j} = \frac{2h}{45}l_j s_{m;m',j}$ and using the mapping $\nu \leftrightarrow (m', j)$ from before results in

$$t_{m,n} = \delta_{m,n}\frac{2k_{L;n}}{k_{L;n}+k_{R;n}} + \sum_{\nu=1}^{N_m\cdot N_x} h_{m;\nu}\varphi_{n;\nu} = \delta_{m,n}\frac{2k_{L;n}}{k_{L;n}+k_{R;n}} + \boldsymbol{h}_m \cdot \boldsymbol{\varphi}_n, \tag{C.28}$$

which is a simple dot product between two vectors.

Bibliography

[1] J. H. Davies, *The Physics of Low-dimensional Semiconductors - An Introduction* (Cambridge University Press, 1997).

[2] M. A. Kastner, *Artificial Atoms*, Phys. Today **46**, 24 (January 1993).

[3] B. J. van Wees, H. van Houten, C. W. J. Beenakker, J. G. Williamson, L. P. Kouwenhoven, D. van der Marel, and C. T. Foxon, *Quantized conductance of point contacts in a two-dimensional electron gas*, Phys. Rev. Lett. **60**, 848 (1988).

[4] H. van Houten and C. Beenakker, *Quantum Point Contacts*, Phys. Today **49**, 22 (July 1996).

[5] Y. Imry and R. Landauer, *Conductance viewed as transmission*, Rev. Mod. Phys. **71**, S306 (1999).

[6] H. Bruus and K. Flensberg, *Many-Body Quantum Theory in Condensed Matter Physics* (Oxford University Press, 2004).

[7] S. Datta, *Electronic Transport in Mesoscopic Systems* (Cambridge University Press, 1995).

[8] D. K. Cheng, *Field and Wave Electromagnetics*, 2nd ed. (Addison-Wesley Publishing Company, 1989).

[9] P. F. Bagwell, *Evanescent modes and scattering in quasi-one-dimensional wires*, Phys. Rev. B **41**, 10354 (1990).

[10] D. J. Griffiths, *Introduction to Quantum Mechanics*, 2nd ed. (Pearson Prentice Hall, 2005).

[11] M. R. Spiegel and J. Liu, *Mathematical Handbook of Formulas and Tables*, 2nd ed. (McGraw-Hill, 1999).

[12] N. Lebedev, *Special Functions & Their Applications* (Dover Publications, Inc., 1972).

[13] E. N. Economou, *Green's Functions in Quantum Physics*, 3th ed. (Springer Verlag, 2006).

[14] R. M. Landau, *Quantum Mechanics II - A Second Course in Quantum Theory*, 2nd ed. (John Wiley & Sons, 1996).

[15] J. D. Jackson, *Classical Electrodynamics*, 3rd ed. (John Wiley & Sons, 1999).

[16] M. J. Ablowitz and A. S. Fokas, *Complex Variables - Introduction and Applications*, 2nd ed. (Cambridge University Press, 2003).

[17] E. Merzbacher, *Quantum Mechanics*, 3rd ed. (John Wiley & Sons, 1998).

[18] M. Di Ventra and N. D. Lang, *Transport in nanoscale conductors from first principles*, Phys. Rev. B **65**, 045402 (2001).

[19] G. Cattapan and E. Maglione, *Coupled-channel integral equations for quasi-one-dimensional systems*, Am. J. Phys. **71**, 903 (2003).

[20] J. H. Bardarson, I. Magnusdottir, G. Gudmundsdottir, C. S. Tang, A. Manolescu, and V. Gudmundsson, *Coherent electronic transport in a multi-mode quantum channel with Gaussian-type scatterers*, Phys. Rev. B **70**, 245308 (2004).

[21] M. A. M. de Aguiar, *Exact Green's function for the step and square-barrier potentials*, Phys. Rev. A **48**, 2567 (1993).

[22] M. A. M. de Aguiar, *Erratum: Exact Green's function for the step and square-barrier potentials*, Phys. Rev. A **51**, 2654 (1995).

[23] M. Macucci, K. Hess, and G. J. Iafrate, *Numerical simulation of shell-filling effects in circular quantum dots*, Phys. Rev. B **55**, R4879 (1997).

[24] M. F. Crommie, C. P. Lutz, and D. M. Eigler, *Confinement of Electrons to Quantum Corrals on a Metal Surface*, Science **262**, 218 (1993).

[25] M. Persson, J. Pettersson, B. von Sydow, P. E. Lindelof, A. Kristensen, and K. F. Berggren, *Conductance oscillations related to the eigenenergy spectrum of a quantum dot in weak magnetic fields*, Phys. Rev. B **52**, 8921 (1995).

[26] J. M. Thijssen, *Computational Physics* (Cambridge University Press, 1998).

[27] A. Szabo and N. S. Ostlund, *Modern Quantum Chemistry - Introduction to Advanced Electronic Structure Theory* (Dover Publications, Inc., 1996).

[28] L. Råde and B. Westergren, *Mathematics Handbook for Science and Engineering*, 5th ed. (Studentlitteratur, 2004).

[29] M. Abramowitz and I. A. Stegun, *Handbook of Mathematical Functions - with Formulas, Graphs, and Mathematical Tables* (Dover Publications, Inc., 1965).

[30] K. Kobayashi, H. Aikawa, A. Sano, S. Katsumoto, and Y. Iye, *Fano resonance in a quantum wire with a side-coupled quantum dot*, Phys. Rev. B **70**, 035319 (2004).

[31] M. Sato, H. Aikawa, K. Kobayashi, S. Katsumoto, and Y. Iye, *Observation of the Fano-Kondo Antiresonance in a Quantum Wire with a Side-Coupled Quantum Dot*, Phys. Rev. Lett. **95**, 066801 (2005).

[32] K. Kang, S. Y. Cho, J. J. Kim, and S. C. Shin, *Anti-Kondo resonance in transport through a quantum wire with a side-coupled quantum dot*, Phys. Rev. B **63**, 113304 (2001).

[33] R. Franco, M. S. Figueira, and E. V. Anda, *Fano resonance in electronic transport through a quantum wire with a side-coupled quantum dot: X-boson treatment*, Phys. Rev. B **67**, 155301 (2003).

[34] T. Lobo, M. S. Figueira, and M. E. Foglio, *Electronic transport through a quantum wire with a side-coupled quantum dot*, Braz. J. Phys. **36**, 397 (2006).

[35] W. Lee, J. U. Kim, and H. Sim, *Fano resonance in a two-level quantum dot side-coupled to leads*, Phys. Rev. B **77**, 033305 (2008).

[36] V. Gudmundsson, G. Gudmundsdottir, J. H. Bardarson, I. Magnusdottir, C. S. Tang, and A. Manolescu, *Multi-mode transport through a quantum nanowire with two embedded dots*, Eur. Phys. J. B **45**, 339 (2005).

[37] U. Fano, *Effects of Configuration Interaction on Intensities and Phase Shifts*, Phys. Rev. **124**, 1866 (1961).

[38] J. von Neumann and E. Wigner, *Über merkwürdige diskrete Eigenwerte*, Phys. Z. **30**, 465 (1929).

[39] F. H. Stillinger and D. R. Herrick, *Bound states in the continuum*, Phys. Rev. A **11**, 446 (1975).

[40] H. Friedrich and D. Wintgen, *Physical realization of bound states in the continuum*, Phys. Rev. A **31**, 3964 (1985).

[41] A. F. Sadreev, E. N. Bulgakov, and I. Rotter, *Bound states in the continuum in open quantum billiards with a variable shape*, Phys. Rev. B **73**, 235342 (2006).

[42] F. Capasso, C. Sirtori, J. Faist, D. L. Sivco, S. N. G. Chu, and A. Y. Cho, *Observation of an electronic bound state above a potential well*, Nature **358**, 565 (1992).

[43] M. L. Ladrón de Guevara, F. Claro, and P. A. Orellana, *Ghost Fano resonance in a double quantum dot molecule attached to leads*, Phys. Rev. B **67**, 195335 (2003).

[44] G. Cattapan and P. Lotti, *Fano Resonances in Stubbed Quantum Waveguides with Impurities*, Eur. Phys. J. B **60**, 51 (2007).

[45] G. Ordonez, K. Na, and S. Kim, *Bound states in the continuum in quantum-dot pairs*, Phys. Rev. A **73**, 022113 (2006).

[46] D. C. Marinica, A. G. Borisov, and S. V. Shabanov, *Bound States in the Continuum in Photonics*, Phys. Rev. Lett. **100**, 183902 (2008).

[47] H. Friedrich and D. Wintgen, *Interfering resonances and bound states in the continuum*, Phys. Rev. A **32**, 3231 (1985).

[48] I. S. Gradshteyn and I. M. Ryzhik, in *Table of Integrals, Series, and Products*, 6th ed., edited by A. Jeffrey (Academic Press, 2000).